Theses and Dissertations

August 2019

Light Scattering in Diffraction Limit Infrared Imaging

Ghazal Azarfar

University of Wisconsin-Milwaukee

LIGHT SCATTERING IN DIFFRACTION

LIMIT INFRARED IMAGING

by

Ghazal Azarfar

A Dissertation Submitted in

Partial Fulfillment of the

Requirements for the Degree of

Doctor of Philosophy

in Engineering

at

The University of Wisconsin Milwaukee

August 2019

ABSTRACT

LIGHT SCATTERING IN DIFFRACTION LIMIT INFRARED IMAGING

by

Ghazal Azarfar

The University of Wisconsin Milwaukee, 2019
Under the Supervision of Professor Carol J. Hirschmugl

Fourier Transform Infrared (FTIR) microspectroscopy is a noninvasive technique for chemical imaging of micrometer size samples. Employing an infrared microscope, an infrared source and FTIR spectrometer coupled to a microscope with an array of detectors (128 x 128 detectors), enables collecting combined spectral and spatial information simultaneously. Wavelength dependent images are collected, that reveal biochemical signatures of disease pathology and cell cycle. Single cell biochemistry can be evaluated with this technique, since the wavelength of light is comparable to the size of the objects of interest, which leads to additional spectral and spatial effects disturb biological signatures and can confound the understanding and analysis. In the present research, the measured signatures are corrected by cleaning the spectra to improve the fundamental analysis of single cell samples.

In diffraction limit FTIR imaging, where the size of the sample is in the same range as the incident light, scattering phenomenon appear in spectra as a result of the interaction of light and matter. The observed scattering contribution depends on the physical and chemical structure of the sample as well as the focusing optics and the light source.

It is crucial to consider the light source to interpret any image, for example visible images taken by a flashlight or a laser provide distinct information about the sample. Synchrotron and

thermal light sources are currently employed in FTIR imaging, and infrared laser sources are quickly being adopted for future application. Lasers are fully coherent light sources, while synchrotron and thermal sources (like flashlights) are partially coherent and non-coherent light sources, respectively. Coherency of the light can have a profound effect in the diffraction limited imaging and needs to be taken into account when analyzing hyperspectral images.

The objective of the thesis is to understand and remove scattering contributions in infrared hyperspectral images. The first Chapter of the thesis introduces the wide field FTIR imaging technique and describes the distinct observations for scattering objects using a large single detector vs a focal plane array, that is a two-dimensional array of small detectors. The former has been well established with many theories that accurately predict the detected signals, while the latter topic regarding what is detected in a single pixel detector is a central question that is addressed in this thesis.

In Chapter 2, an in-depth analysis of stressed, hydrated algal cells (*Thalassiosira weissflogii*) measured with FTIR spectromicroscopic imaging is presented. The spatially varying, pixelated, biochemical response to environmental stresses has been revealed. This prototypical experiment shows the potential of such imaging to monitor in-situ biochemical changes, for single cells that are maintained in a water environment with minimal scattering, but highlights the need to remove inherent spectral and spatial fringes from data that are inherent when maintaining cells in such an environment.

Many Hydrated single cells with distinct biochemistry have important chemical distributions (e.g. yeast cells) and are therefore interesting to measure without a hydrated environment. However, the infrared measurements of these cells are frequently dominated by scattering, since

they are similar in size to the wavelength of the probing light. Due to the presence of scattering, the individual pixels in wide field FTIR imaging have spectral responses that represent both the chemistry and physical response of the sample. Pure absorbance spectra are desired to detect the subtle differences in biochemistry that are important. However, the pixelated data contain abrupt spectrally dependent inhomogeneities, since samples with geometrical shape, and refractive indices that are different from their environment strongly deviate direction of the incident light.

As a first step to understand the effects of light scattering in pixelated FTIR imaging, homogenous microspheres with size similar to the wavelength of light are studied, experimentally and theoretically. In Chapter 3 experimental results for polymer (PMMA) microspheres imaged with a synchrotron and a thermal source are provided. Interestingly, the pixelated spectra measured with synchrotron source are distinct from the ones measured with a thermal source. The distinction between the spectra measured with synchrotron and thermal sources is being related to the spatial coherency of the light source.

In Chapter 4, hyperspectral images of the microsphere are simulated using the resonant Mie scattering theory. The simulated images give an insight about the experimental results and help answer the question of what is detected in a single pixel. A full understanding of the impact of scattering effects on spatial and spectral responses will enable us to develop strategies for deconvolving the scattering contributions and recovering pure absorbance images.

With the insight gained from the experiments and simulations, we identified that removing scattering from pixelated spectra is feasible by an iterative inverse method. The outcome is presented in Chapter 5 as a new algorithm. It is shown that, the complex refractive index of the

sample can be recovered by measuring amplitude and phase of the electric field. The algorithm is not sensitive to noise, and it can recover refractive indices of samples with high absorption.

By incorporating a finite element software and extending the algorithm, recovery of the complex refractive index of the sample with super resolution is expected.

v

To my family

TABLE OF CONTENTS

xi

LIST OF FIGURES

LIST OF TABLES

xiv

ACKNOWLEDGEMENTS

Firstly, I would like to express my gratitude towards my advisor Prof. Carol Hirschmugl for her kind support, encouragement, patience and creativity that made this thesis a reality. Her exceptional personality, communication and leadership skills made her a role model for my personal and professional life.

I would like to thank Prof. Achim Kohler for his help and insight in the fringe correction of the hyperspectral infrared images. I would also like to thank Prof. Reinhold Blumel for his constant feedback and suggestions on the inverse scattering algorithm. I really appreciate the comments from Prof. Yongjin Sung for evaluating the inverse scattering algorithm, and his kindness for providing holographic images of melanoma cells. I would also like to thank Professor George Hanson for his extensive support during my studies at UWM. I would also like to thank my committee advisor Professor Law for his interest in my work, valuable feedback and advice.

Special thanks to the members of my research group, Nick Walter, Alex Schofield, Sugato Ray and Ebrahim Aboualizadeh. It was great to work and learn with them.

Finally, I would like to acknowledge my family who their lifetime emotional support made me who I am. Special thanks to my parents for their loving support, my brothers Mehran and Alireza, my beloved aunt Kathy and my uncle Jamshid.

Chapter 1

1 Introduction

1.1 IR Vibrational Spectroscopy

Infrared spectra result from interaction of infrared light with matter. Molecules can absorb photons with energy level that match with their molecular band gap. As a result of the absorption of the light, molecules transit between quantized vibrational energy states. Molecular vibrations can range from the simple coupled motion of the two atoms of a diatomic molecule to the much more complex motion of each atom in a large polyfunctional molecule (Griffiths & de Haseth, 2007) .
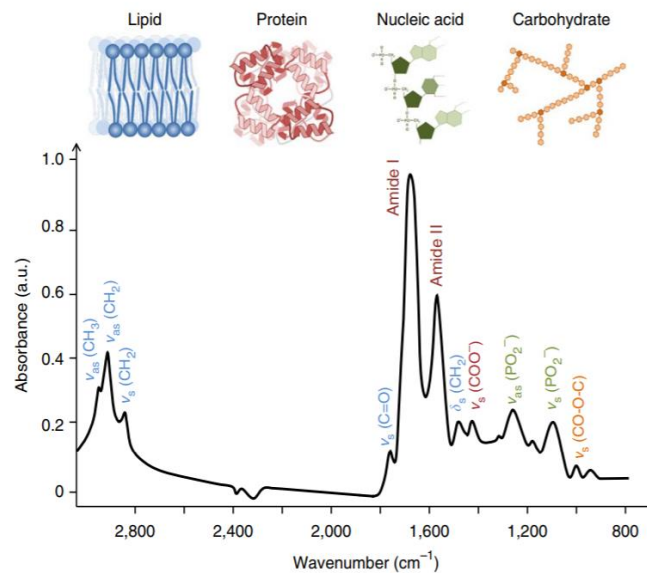
Figure 1 | Typical biological spectrum showing biomolecular peak assignments from 3,000–800 cm−1, where v = stretching vibrations, δ = bending vibrations, s = symmetric vibrations and as = asymmetric vibrations. The spectrum is a transmission-type micro-spectrum from a human breast carcinoma (ductal carcinoma in situ). The sample was cryosectioned (8 μm thick) and mounted on BaF2 slides (1 mm thick) before IR microspectroscopy. Equipment: Bruker IR scope II, circular diameter of aperture ~60 μm; a.u., arbitrary units. (Baker, et al., Using

1
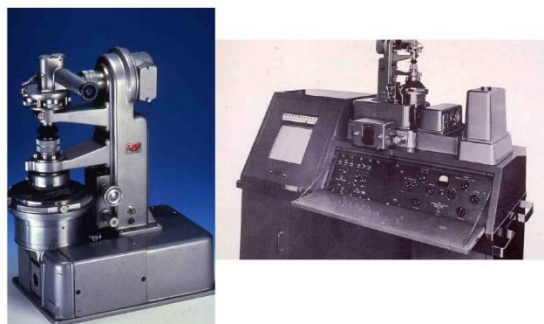
Figure 2 (a) One of the First Infrared spectrometers, Prototype Model 12 (1943) (Tisinger, 2018) *(b) The first commercial IR micro spectrometer PE model 85 (1953)* (Tisinger, 2018)

Mid-IR ($4000 - 400$ cm^{-1} ≡ 2.5 μm − 25μm) spectroscopy is a powerful stain-free technique for biological analysis. Figure 1 shows a typical biological spectrum showing biomolecular peak assignments from 3000-800 cm^{-1}.

1.2 History

The history of the FTIR spectroscopy goes back to World War II, when Beckman at National Technical Laboratories characterized gasses by IR to manufacture rubber for defense purposes, concurrently Baird at Dual Beam laboratory used infrared characterization for penicillin manufacture. (Tisinger, 2018)

Figure 2 shows the Prototype Model 12 (1943). These early instruments were splitting up the infrared interferogram into wavelength dependent components with a prism. The first commercial IR spectrometer was made in 1944, and it was called PE IR12.

C.R. Burch et al. provided reflective objectives as a solution to optimize the image reproduction for reflecting microscopy (Burch, 1947). R. Barer coupled a Burch design reflecting

www.manaraa.com
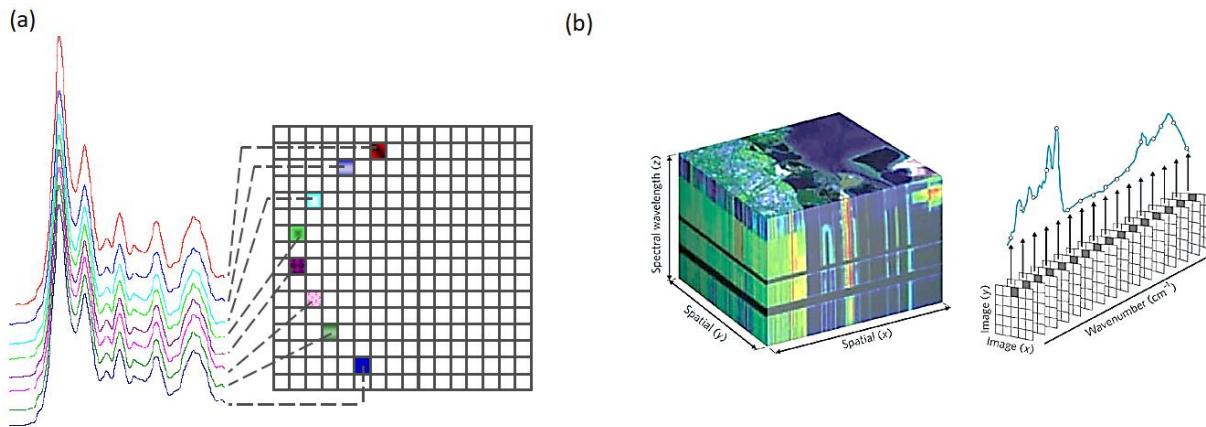
Figure 3 (a) Chemical Image; Sample is imaged onto a FPA detector (nxn pixel array), each pixel has an entire spectrum (~1.1 μm) (b) Representation of the FTIR Images in the form of Hyperspectral Cube. (Hyperspectral remote sensing, 2019)

microscope to a PE recording IR and invented the first IR micro spectrometer (Barber, Cole, & Thompson, 1949).

At 1950 E. R Blout et al. discussed performance characteristics of IR Microscopes, (Blout & Bird, 1950). The first commercial IR Microscope (Perkin-Elmer Model 85) was made by V. J Coates in 1953 (Coates, Offner, & Siegler, 1953).

Commercialization of digital computers, and invention of sensitive detectors lead to fabrication of the first FTIR Microscope (Digilab UMA 100) at 1980. In a FTIR micro spectrometer the prism of the spectrometer is replaced by a digital Fourier transformer, which decomposes the interferogram into the wavelength components.

The first FTIR Imaging was done at 1995 by E. N. Lewis et al. with resolution of 17.5 µm by the first Focal Plane Array (FPA) (Lewis, et al., 1995). Today's FTIR Imaging systems have nominal resolutions of as high as 1.1 µm.

FPA- FTIR detectors provide the ability to acquire a grid of spectra in the same amount of time that it takes single point detectors to acquire one spectrum. The data measured with an FPA is called a Chemical Image or a Hyperspectral Cube. This data format is shown in Figure 3. The
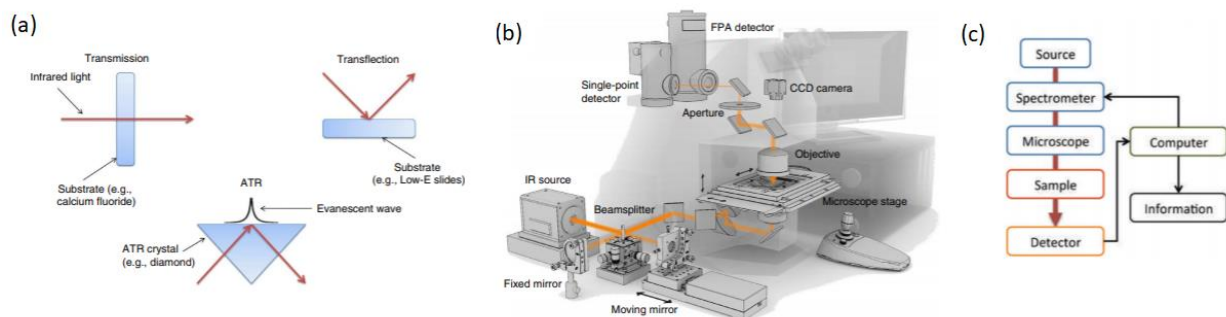
Figure 4 The instrumentation underlying the main forms of IR spectroscopic sampling. (a) Schematic of modern FTIR-imaging spectrometer (only transmission path is shown). (Baker, et al., Using Fourier Transform IR spectroscopy to analyze biological materials, 2014) (b) Schematic representation of the three main sampling modes for FTIR spectroscopy. (c) Conceptually, the optical path proceeds from a source to a spectrometer, microscope, sample, and to the detector. The computer serves to operate the spectrometer and process signals from the detector into information. (Bhargava, 2012)

hyperspectral image shown is consisted of a series of absorbance images of the same sample at different wavelengths. Figure 3 (a) shows infrared spectra extracted from single pixels of the cube. Figure 3 (b) shows the hyperspectral cube, and it indicates that the absorbance spectrum of the pixel is consisted of the intensity values of the pixel from wavelength dependent absorbance images that are placed in series.

1.3   FTIR Micro-spectroscopy

Fourier transform spectrometers allow measuring infrared absorption by a sample in three different geometries as shown in Figure 4 (a): transmission, transflection and attenuated total reflection (ATR). A schematic view of a Fourier transform infrared (FT-IR) micro spectrometer is shown in Figure 4. FTIR micro spectrometers allow usually transmission and reflection sampling configurations in the same system. A single point detector and a FPA detector are provided for both point mapping and imaging technology. An external interferometer and a computer are used to record and process data. Figure 4 (c) shows the conceptual optical path from a source to the detector. The light after passing through a Michelson interferometer is coupled to the microscope, that focuses the light on the sample, and depending on the numerical aperture of the collecting

4

optics, the scattered light is partially collected. The detected light is an interferogram distorted by the sample.

1.3.1 Mid-infrared light sources

The light source is a key component in MIR infrared imaging systems and has an impact on the design of the rest of the system. Globar (Thermal) and synchrotron light sources are known as the two well-established light sources in infrared imaging. Additional light sources such as quantum cascade lasers (QCL), MIR super continuum light sources and free electron lasers (FEL) have become available in Mid-IR region.

A globar (thermal) is the simplest and cheapest IR source. It is a filament made of silicon carbide that is heated up to 1000-1650 °C by an electric current, and it radiates according to Planck's law. The output radiation is spatially and temporally incoherent and has a large spectral emission range (2-25 µm), but low intensity (Hermes, et al., 2018).

Synchrotron and FEL light sources radiate based on the Bremsstrahlung effect (Abo-Bakr, et al., 2003). They can cover the whole MIR spectral range with significantly higher brightness. Synchrotron and FEL light sources are big facilities and expensive to maintain. Bremsstrahlung radiation that is also called "braking radiation" and "deceleration radiation" is an electromagnetic radiation generated by charge particles that are accelerated to a relativistic speed, while their transverse motion is modulated by a magnetic field. Although the synchrotron radiation is generally known as incoherent source, some design can achieve coherence in certain spectral ranges (Hermes, et al., 2018).

Quantum cascade lasers are high power (over 200 W) infrared sources. Their emission spectral range span from 2.36 µm to 24.4 µm. The QCL chip is pumped by applying a voltage across it.

5

The chip is a carefully designed heterostructure enable electrons to move into an upper laser level in the conduction band, where these electrons undergo a radiative transition to a lower state in the conduction band. Finally, the electrons exit the lower laser state through a non-radiative transition to upper laser state of the next cascade. Typically, there are 30-40 cascades within one laser structure. Increasing the number of cascades can technically increase the efficiency of the laser. To make a balance between thermal conductance and power efficiency usually 10-15 cascades are used for high power applications. These semiconductor lasers are small, they are tuned electronically and have mass production potential. The spectral range of the most of the commercially available QCL chips does not cover the whole MIR range, so multiple chips are combined into a system with a common output port (Hermes, et al., 2018).

Supercontinuum infrared light sources have high brightness, and a broad spectrum. In a supercontinuum laser, narrowband optical pulses pass through a variety of nonlinear optical effects that broadens the spectral range. Optical fibers have been proven to be suitable for this purpose, as light passes through a long interaction length. Current commercially available MIR supercontinuum sources do not extend beyond 2200 cm^{-1}. Supercontinuum laser have a high quality beam with spatial coherence, enabling diffraction limit performance.

1.3.2 MIR Detectors

MIR detectors compare to the visible detectors are more sensitive to noise. Specially the noise resulting from black body-radiation of their own components. As a result, low noise performance can only achieve by cryogenic cooling. Cold shielding is also used to minimize radiation from the surrounding objects. MIR detectors are generally either of thermal detectors or photonic detectors. Thermal detectors are made of materials that absorb light and the increase in their temperature can

6

be detected. Absorption of light in photonic detectors result in creation of electron-hole pairs giving rise to a current (Hermes, et al., 2018).

Bolometers and thermopiles are two kind of thermal detectors. The bolometer sensor has a temperature dependent electrical resistance, that can be detected by measuring the voltage across the sensor when a constant current is passing through it. The sensitivity of the bolometers depends on the temperature coefficient of resistance of the sensor material. IR imaging in the wavelength regime of 8-14 µm, is achieved using microbolometer arrays. The arrays are typically 320x240 pixels, and the individual pixel dimension is of the order of 20µm×20µm. As the size of the individual pixels decreases, their sensitivity to IR radiation decreases, that result in a larger noise equivalent temperature difference. Thermopiles are another type of thermal detectors, that measure temperature change through a series of thermocouple devices. Thermopiles are less sensitive compare to bolometers, nevertheless they are cost effective and have several applications in medical, farming and automotive industry (Hermes, et al., 2018).

Photodetectors are based on the photon absorption in a semiconductor material resulting in an electronic transition generating a free charge carrier. The working wavelength range of the detector depends on the band gap of the sensor. Silicon (Si) is the material that is preferred for light detection in spectral range of 350 to 1100 nm and is basically a PIN diode (a diode made of three layers of material: a wide undoped layer of intrinsic semiconductor sandwiched between a p-type semiconductor and a n-type semiconductor). Longer wavelengths in range of 0.85 to 1.7µm are being detected by InGaAs which is made as an avalanche photodiode. Indium antimonide (InSb) can be used in the range of 3-5µm, whereas mercury cadmium telluride (MCT) is commonly used in the wavelength range of 2-12µm. InSb and MCT both need to be cooled with liquid nitrogen. However, InSb has a better noise performance than an MCT. The relatively large wavelength range

7

of MCT detectors makes them a good candidate for FTIR spectrometry. Focal plane arrays (FPA) of MCT are used for FTIR imaging (Hermes, et al., 2018).

Upconversion based detection is another approach for IR sensing. In upconversion IR sensing instead of detecting the low energy IR radiation, the IR radiation is mixed with a high brightness laser in a transparent nonlinear medium, shifting both spectral and spatial information from the low energy infrared range to the NIR or visible range, for which fast and sensitive detectors exists. A transparent medium here means that no black-body radiation from the medium is added to the IR signal (Hermes, et al., 2018).

1.3.3 Optics and Sample Preparation

The spatial resolution of a MIR microscope depends on the wavelength of the light, the collecting optics, and the pixel size of the detector. Schwarzschild optics that consist of a matched pair of Cassegrain objectives are used for broadband imaging using incoherent light sources. The Cassegrain objective has a central convex mirror that reflects the incoming light toward the secondary concave mirror above it. The secondary mirror focuses the light to the sample. Schwarzschild optics correct spherical aberration, coma and astigmatism over a wide range of wavelengths. The central mirror of the Schwarzschild objective and its mount cause obscuration of the image that can become a problem in coherent imaging. However coherent light sources are usually brighter than the incoherent light sources, and therefore losses due to lower optical throughput of the refractive optics can be tolerated (Hermes, et al., 2018).

As shown in Figure 4. FTIR microscopy is done in three different geometries of ATR, transmission, and reflection. In transmission configuration light is focused onto the sample by a condenser, and the light transmitted in the forward direction is being collected with a second

8

objective. In reflection configuration, sample is mounted on a reflective substrate, and the backward light is collected with the illuminating objective. The third way for FTIR imaging is ATR using a high refractive index crystal. In this case, the sample is place on an ATR crystal. The irradiated IR beam internally reflects at the boundary of the crystal and the sample, resulting in an evanescent wave propagating orthogonally to the surface into the sample. The energy of the radiated field is partially absorbed by the sample, and as a result the light detected by the sensor is attenuated. When the illumination angle is larger than the critical angle between the crystal and sample, a purely ATR spectrum is observed (Hermes, et al., 2018).

For ATR measurements, a thin layer of the sample, usually 1-3µm (practically can be any thickness), is pressed onto a crystal. For transmission and reflection measurements, the sample needs to be mounted on a transmissive or a reflective substrate. Calcium fluoride (CaF_2) and barium fluoride (BaF_2) are the optimal substrates for IR measurements. For reflection mode measurements the substrate is usually a glass slide, coated by gold or a thin aluminum layer covered by a thin oxide layer (Hermes, et al., 2018).

When the size of the sample is in the order of the wavelength spectral features known as Mie scattering are observed at the spectra. Bassan et al (Bassan, Light scattering during infrared spectroscopic measurements of biomedical samples, 2011) developed an algorithm for scattering correction of the spectra for the case where the detector size is larger than the sample size. This method is recently optimized by Konveskikh et all (Konevskikh T. , Lukacs, Bl̇umel, Ponossov, & Kohler, 2015) (Solheim, et al., 2019) (Konevskikh , Lukacs, & Kohler, 2017). Mie scattering features are explained with more detail in Section 1.5.2.

The FTIR measured data is essentially a hyperspectral image with chemical information about the sample. There are a range of multivariant analysis techniques to extract the desired chemical information from the infrared hyperspectral image. A hyperspectral image is a data cube with two spatial dimension (x,y), and one spectral dimension (λ).

1.4   Analysis of Hyperspectral data cubes

Several general pre-processing techniques are needed in order to obtain meaningful spectral information. For disease pathology applications tissue is sectioned by a microtome. Due to variations in thickness of the tissue and due to differences in the effective optical path length, a normalization step is needed in the preprocessing. Vector normalization (Brereton, 2009), min-max normalization, multiplicative scatter correction (MSC) (Geladi, MacDougall, & Martens, 1985) (Wold, Martens, & Wold, 1983), standard normal variate (SNV) are some of the established normalization techniques.

For general problems where there is an unwanted signal in the background of the spectra, a polynomial is fitted to the baseline and is being subtracted from the spectrum. In histopathology application, samples are mostly a mixture of complex biochemical compounds, resulting in complex IR spectra with overlapping peaks. In this situation a common approach is to use derivative spectra. Derivative spectra have two advantages, firstly the baseline is removed automatically and secondly it emphasizes the shoulders of the broad peaks (Hermes, et al., 2018).

Atmospheric water vapor removal, resonant Mie scatter corrected by EMSC, and paraffin removal are some of the specific preprocessing techniques for preprocessing of the IR spectra and are application dependent (Hermes, et al., 2018).

10

After preprocessing of the spectral data, in order to improve the understanding of chemical information, and correlating the physical parameters to analytical data, multivariant chemometrics are used. Chemometrics is the science of extracting information from chemical systems by data-driven means. Principal components analysis (PCA), and classification methods such as linear discriminant analysis (LDA), super vector machines (SVM) and K-means clustering are some of the algorithms that are used in chemometrics for extracting information from spectral data (Hermes, et al., 2018).

1.5   Applications

FTIR chemical imaging is widely used for visualization of chemical distribution at the micro scale. For example, it is being used for polymer characterization, art conservation and pharmaceuticals.

The ability to detect biologically important chemical bands such as protein (Amide I and Amide II), Lipids (CH2 and CH3), and carbohydrate without labeling makes FTIR imaging a desirable technique for disease pathology and cell cycle study and tissue imaging. Chapter 2 of the thesis is an example of the single live cell imaging by FTIR.

In Section 1.4 it was mentioned that, there are some undesired features observed in spectra of biological sample. Preprocessing techniques are used to remove these features from the spectra. These undesired spectral features are called spectral distortion. The physical origin of the spectral distortion is not always obvious to the spectroscopist. Depending on the application and the sample, a specific signal correction method is needed. Section 1.6 is the summary of some of the well-known spectral distortions.

11
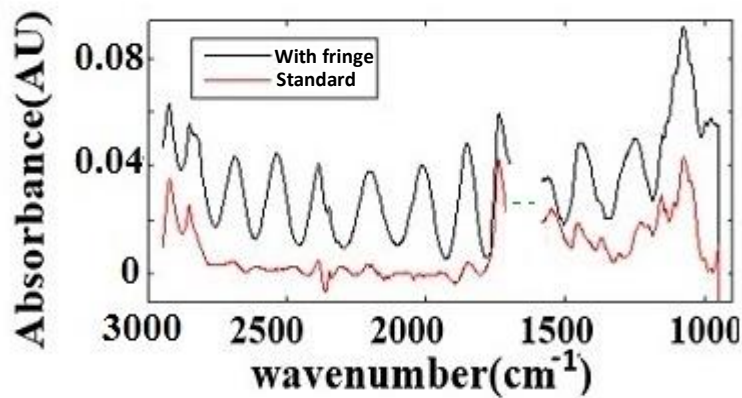
Figure 5 Spectra of algal cell, with finges and baseline, and the standard algal cell spectrum

1.6 Spectral Distortion

Spectral features observed in the measured infrared spectra are not always because of chemical absorption bands of the molecules. Physical shape and size of an object can distort the measured spectra. Spectral distortions happen because of physical phenomena such as scattering, multiple internal reflections etc. In the following subsections two forms of spectral distortions are introduced.

1.6.1 Fringes

Fringes are a form of spectral distortions, which hinder quantitative analysis of the spectra. Fringes appear in the spectra of thin films, due to multiple internal reflection of the light in the material. Figure 5 shows a spectrum of an algal cell distorted with fringes and a standard algae spectrum. Fringes change the relative peak heights of chemical bands and hinder further analysis of the spectrum.

In chapter 2, an Extended Multiplicative Signal Correction method is proposed for removing the fringes from hyperspectral cubes.

12

1.6.2 Scattering

Fourier Transform Infrared (FTIR) micro spectroscopy is a powerful technique in chemical analysis of micron size biological samples. When the size of an object is in the same order of infrared wavelength (3 to 10µm), scattering can distort infrared spectra. In single cell imaging, where the diameter of the object is ~10 to 50 µm, the geometrical shape of the object plays a role in scattering effects in pixelated infrared spectra.

Scattering behavior of single particles in the forward direction is explained by means of a quantity called Q extinction, which is dependent on the refractive index, and the size of the particle. Absorption of a low-absorbing dielectric sphere with radius r, refractive index of n, and magnetic permittivity of µ=1, is defined using its scattering, and absorption cross sections.

In a regime, where the geometric cross section of a sphere $g = \pi r^2$, is smaller than the area of the detector G (G > g), the absorption is calculated as follows (Hulst, 1981).

Consider I_0 as the incident intensity, I_{sca} the scattered intensity, I_{abs} as the absorbed intensity, and I as the un-scattered intensity moving in the forward direction.

Defining the scattering cross sections as σ_{sca} and the absorbing cross section as σ_{abs}, the extinction cress section is defined as $\sigma_{ext} = \sigma_{sca} + \sigma_{abs}$.

With the help of G and the cross sections, the associated radiative powers are calculated.

$P_0 = I_0 G, P_{sca} = I_0 \sigma_{sca}, P_{abs} = I_0 \sigma_{abs}$, and $\quad P = IG$.

Due to energy conservation, we can write:

$$P_0 = P + P_{sca} + P_{abs} \qquad (1.1)$$

13
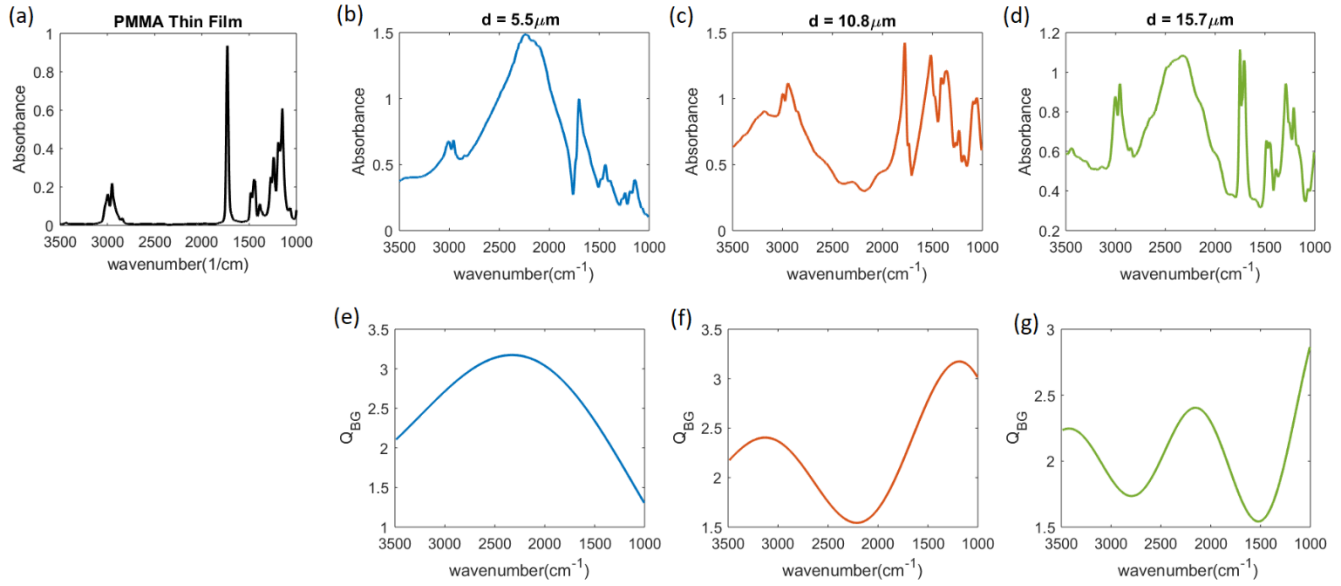
Figure 6 (a) shows absorbance spectra of a PMMA thin film, while Figure 5 (b) to (d) show spectra of PMMA beads with diameters of 5.5µm, 10.8 µm, and 15.7 µm for a single detector.

Therefore,

$$I_0 G = IG + I_0 \sigma_{sca} + I_0 \sigma_{abs} = IG + I_0 \sigma_{ext} \qquad (1.2)$$

The apparent absorbance, which is measured in the experiment is defined as:

$$A = -\log_{10}(\frac{I}{I_0}) \quad (1.3)$$

This is called the apparent absorbance because it includes not only the intensity lost due to (chemical) absorption but also the intensity lost via scattering. Because of the finite illuminated area G of the detector, and because of its finite distance to the scatterer, apart from collecting the unscattered intensity I, the detector collects some scattered light (Blumel, Bagcioglu, Lukaccs, & Kohler, 2016).

The scattering contribution of a single bead with a constant real refractive index, where G > g is estimated by Van de Hulst approximation as follows

$$Q_{ext} = 2 - \frac{4}{\rho} \sin\rho + \frac{4}{\rho^2}(1 - \cos\rho) \qquad (1.4)$$

14

$$\rho = 4\pi r(n_0 - 1)\upsilon \qquad (1.5)$$

Where r is the radius of the sphere, n_0 is the nominal refractive index and υ is the wavenumber (Hulst, 1981).

Figure 6 shows the infrared spectra of a PMMA thin film compared to spectra of three homogenous PMMA beads with different diameter sizes. The variations observed in the spectra shown in Figure 6 (a) to (d), are the result of size dependent scattering contributions (Bassan, Light scattering during infrared spectroscopic measurements of biomedical samples, 2011). Figure 6 (e) to (g) show the Q_{ext} or the scattering backgrounds of the corresponding PMMA beads in Figure 6 (b) to (d).

While the scattering contributions in infrared spectra obtained with a single detector (where G > g) are well understood and can be expressed by Eq. (1.5) and (1.4), the scattering contributions in high resolution infrared images, where the detector consists of an array of detectors(pixel), with sizes smaller than the sample (where g < G), is not well explained in literature. The scattering in hyperspectral infrared images are discussed in more detail in Chapters 3 and 4.

1.7   Objectives of the thesis

The objective of the thesis is to understand and remove scattering from hyperspectral infrared images and extract pure absorbance spectra from infrared chemical images.

Time resolved metabolic response of an algal cell (*Thalassiosira weissflogii*) in a controlled microfluidic channel is measured by means of FTIR micro spectroscopy. This prototype experiment is indicative of high potentials of the technique in measuring chemical changes of biological samples. However, unlike algal cell most of the biological cells have inhomogeneities that result in angular scattering of the light. The light that reaches the detector is partially absorbed

15

and partially scattered by the sample, so measuring the pure absorbance in the forward direction is not possible for samples with high scattering coefficients. In addition, depending on the properties of the source (such as brightness and coherency), the intensity of the light detected by each pixel of the detector changes.

The transmitted intensity through a sample depends strongly on the degree of the coherence of the source, when the size of the sample is comparable to the effective transverse coherence of the incident light. In order to observe the effect of spatial coherency of the incident light on the images measured by the FTIR technique, fringe patterns of a united states air force target (USAF) are measured by a synchrotron and thermal source, respectively. In order to measure the effect of the source on Mid-Infrared spectra, a 25µm radius polymer (PMMA) sphere is measured again with two sources. The result show, that with the current method of data collection, the measured spectra are a complex mixture of the sample geometry, spatial coherency of the source and the collective optics.

In order to gain insight on an ideal measurement, the broadband image of a 25µm radius PMMA sphere is simulated by Green's function of the Maxwell's equation.

In order to remove scattering, an optimization algorithm is provided for correcting the infrared spectra. This algorithm fits the measured electric fields of the sphere to a simulated one through an iterative process for finding the complex refractive index of the sample. It is found out that the recovery of the pure absorbance of highly scattering samples is possible with the measurement of the phase in addition to the amplitude of the electric field.

16

Chapter 2

2 Fringe Corrections

In this chapter FTIR hyperspectral images of algal cells (*Thalassiosira weissflogii*) in a micro fluidic channel are presented. The channel is flowed by water and nutrients to provide a controlled environment. The micro channel is modeled as a multilayer thin film (see Section 2.4). Although, the normal incident light transmits in the forward direction through the sample, the measured spectra are hindered by multiple internal reflection of the light from the boundaries of the layers of the film. In this chapter, a review on the complexities involved with hyperspectral imaging of live cells in a microfluidic channel is presented. Then a method for correcting multiple internal reflections from hyperspectral infrared images is introduced, and chemometric analysis of the infrared images of an algal cell is provided. The analysis reveals information about the phenotypic photosynthesis cycle of the algal cells.

2.1 Introduction

By employing a high-resolution microscope equipped with a multi element infrared detector - focal plane array (FPA), and a bright infrared source, chemical and structural variation of cells can be observed. Here, short-term acclimation of an algal cell responding by stress to its environment is revealed by employing synchrotron FTIR imaging combined with a preprocessing approach including fringe correction, and data analysis. Live cells must usually be kept in an aqueous environment. However, water is highly absorbing in the mid-infrared range (Meglinski, 2015) (Rahmelow & Hubner, 1997). A thin transparent sample is achieved by placing the cell in a microfluidic channel. Prior studies of (Kuimova, Chan , & Kazarian, 2009) (Miyamoto, et al.,

17
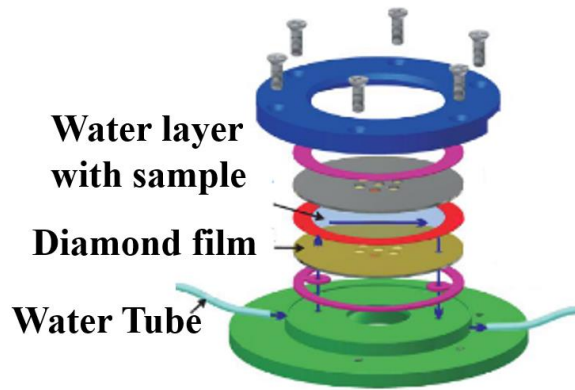
Figure 7 Demountable liquid flow cell using submicrometer thick diamond windows

2007) (Wieliczka, Weng, & Querry, 1989) revealed free flotation and mobility of the cell in this geometry, that requires rapid measurement so that the sample is stationary during the measurement. Rapid measurement reduces spectral resolution and signal to noise ratio(S/N). Here, an assembly with sub-micron thick diamond windows is employed, as shown in Figure 7. (Nasse, Ratti, Giordano, & Hirschmugl, 2009) A bright synchrotron source is used to achieve diffraction limited spatial resolution (Quaroni, et al., 2014).

The demountable microfluidic channel is shown in Figure. 7, when the windows of a microfluidic cell are separated by a distance close to the wavelength of probing radiation, multiple internal reflections are common, and lead to well understood spectral features that hinder the analysis of the data. (Ibrahim, Predoi-Cross, & Povey, 2013) These sinusoidal spectral features are called fringes.

There are two categories of fringe correction techniques: software based, and hardware based. In hardware-based techniques, the sample is rotated so that the angle of incidence is the Brewster angle to achieve maximum transmittance (Farrington, Hill, O'Donnell, & Pomery, 1990) (Harrick, 1977) (Hetch, 1974). A spectrum measured by this technique is only accurate in low absorptivity regions, and this experimental geometry is not always feasible. Various software-based techniques for fringe correction exists. Examples are interferogram editing, fringe fitting and subtraction from

18

the spectrum (Hirschfeld & Mantz, 1976) (Hirschfeld T. , 1978) (Clark & Moffatt, 1978) (Konevskikh, Ponossov, Blümel, Lukacs, & Kohler, 2015), low frequency filtering (Melin, Perromat, & Déléris, 2001), synthetic background generation based on the fringes in a sample interferogram, and digital filtering of the spectrum along with Savitzky-Golay algorithm (Savitzky & Golay, Smoothing and Differentiation of Data by Simplified Least Squares Procedures., 1964). Here we will introduce an alternative method to remove the spectral fringes and recover high quality hyper spectral time dependent chemical images based on Konvskikh et al. (Konevskikh, Ponossov, Blümel, Lukacs, & Kohler, 2015). The hyper spectral time dependent chemical images are 4 dimensional (x, y, λ, t) cubes, containing 64x64x1037x5 independent pieces of information. To extract statistically reliable information from these large data sets statistical methods must be employed. Principal Component Analysis (PCA) has been widely used in spectroscopy to reduce data and determine compounds since the nineteen-seventies.

Recently, Hobro et al. (Hobro, et al., 2015) has shown, PCA not only resolves the spectral features of a hyperspectral cube; it also provides insight into the spatial distribution of the compounds. The macromolecules are identified by wavelength dependent PC loadings, that define a new coordinate system for the hyperspectral cube. The projections of the measured data onto the new coordinate leads to new images (PC scores), that highlight the spatial distribution of largest chemical variations in the dataset. PCA is used to demonstrate that the fringe removal of spectral fringes is robust. Analysis of the spatial and spectral PCs of the stressed and control algal cells provides an interpretation of the short-term acclimation process of the algal cell as it responds to a stressed environment.

19

2.2 Methods

2.3 Experiment

Batch cultures of *Thalassiosira weissflogii* acclimated to ambient conditions (30 μM NO_3^-) under constant irradiation of 120 $\mu M/(m^2 s^2)$ photons at 20 °C at CO_2 concentration of 390 pmm are studied. For single cell measurement, diatoms harvested from the batch cultures are mounted in a liquid-flow cell, which supports a controlled aqueous environment. Cells were maintained in the 390ppm CO_2 conditions by flowing a water medium prepared at ambient conditions, and stressed cells were obtained by exposing the cells to water medium pumped with air containing 5000 ppm CO_2, at °20 C and under continuous illumination of photosynthetically active radiation (PAR).

Measurements, both for stressed and control samples, were conducted on three independent biological replicates (i.e. three distinct cultures). A synchrotron-based source (IRENI at SRC) coupled to a FTIR Bruker Hyperion 3000 microspectrometer with a focal plane array (FPA) detector (128 x 128 pixels) was used to collect spectrally resolved images of the algal samples. A 20x, 0.6 NA objective was used to illuminate the sample, and a 74x objective 0.6 NA objective was used to collect and image the transmitted radiation onto the detector, where a geometrical sample of 0.54 x 0.54 mm^2 per pixel was obtained, collecting images every 15 minutes for at least 2-hour duration. The short-term acclimation of the algal cell to the two conditions (control and stressed) was monitored in the spectral range of 948 cm^{-1} to 2946 cm^{-1}, with a spectral resolution of 4 cm^{-1}. Measured spectra were smoothed using the Savitsky-Golay function of order 2 with 9 points.

20

Infrared transmission hyperspectral data cubes are obtained by collecting two sets of images, one background hyperspectral data cube and one sample data cube. Reference data cubes were taken from the aqueous environment of the water as close as possible to the algal cell being studied. The second set of data cubes (sample data cubes) was taken from region including the algal cell. The division of a sample data cube by the background data cube allowed to remove the background effects and resulted in a transmittance data cube. Since the background image must be devoid of algal cells, it is not possible to use the identical location for both the sample and background. The difference between the two locations leads to slightly different water thicknesses, in the sample and background data cubes. This leads to variations in the frequencies of the fringes. Resulting in fringes with multiple frequencies.

2.4   Fringe Simulation in a micro channel

The matrix theory of optical systems was used to study fringe behavior in a micro fluidic channel. In this theory, the complex amplitude of the forward and backward waves through the boundaries of an optical system is calculated by use of the matrix method (Saleh & Teich, 2007). The wave transfer matrix of a system relates the forward and backward collected waves at input and output planes of the system. The forward and backward waves collected at the input plane of the system are shown by U_i^+, and U_i^-, while U_o^+ and U_o^- denote the forward and backward waves collected at the output plane. The wave-transfer matrix M relates these set of forward and backward waves as follows:

$$\begin{bmatrix} U_o^+ \\ U_o^- \end{bmatrix} = \begin{bmatrix} M_{11} & M_{12} \\ M_{21} & M_{22} \end{bmatrix} \begin{bmatrix} U_i^+ \\ U_i^- \end{bmatrix} \qquad (2.1)$$

21
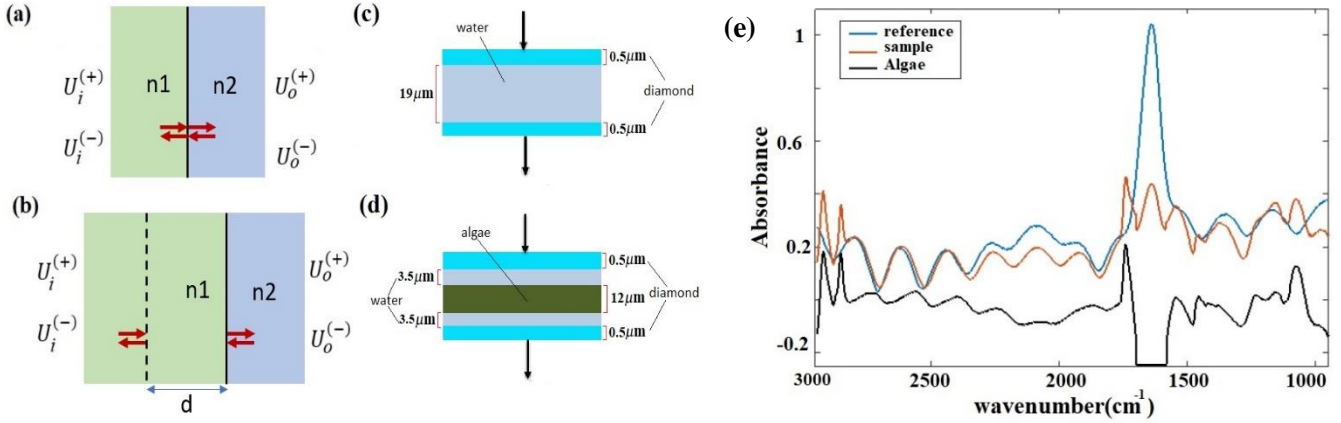
Figure 8 (a) Single dielectric boundary made of two materials with refractive indexes of n1, and n2. (b) A slab of material with refractive index of n1 and width of d followed by a boundary. (e) The blue curve simulates the absorption through the channel, in the absence of algal cell; the red curve simulates the absorption through the channel including the algal cell (the reference transmittance is assumed to be 1 for red and blue curves). The black curve is calculated by subtracting the blue curve from the red one and simulates the algal cell absorbance.

The wave transfer matrix of a multilayered medium, made of *n* layers is described by the matrix product of each single medium. If the transmission matrix of each medium is M_1, M_2, M_3, ...M_n, then the total transfer matrix is defined as

$$M = M_n \dots M_2 M_1 \quad (2.2).$$

The transmittance through the multilayered medium is

$$|t| = \frac{1}{M_{11}} \quad (2.3)$$

By solving the Maxwell's equations and applying suitable boundary conditions, the transfer matrix through a single dielectric boundary as shown in Figure 8 (a), with a refractive index of n_1, and n_2, is calculated as

$$M = \frac{1}{2n_2} \begin{bmatrix} n_2 + n_1 & n_2 - n_1 \\ n_2 - n_1 & n_2 + n_1 \end{bmatrix} \quad (2.4)$$

With the same approach, the transfer matrix through a homogeneous medium with a width of *d*, followed by a boundary as shown in Figure 8 (b) is described by

22

$$M = \frac{1}{2n_2}\begin{bmatrix} (n_2 + n_1)\exp(-j\phi) & (n_2 - n_1)\exp(j\phi) \\ (n_2 - n_1)\exp(-j\phi) & (n_2 + n_1)\exp(j\phi) \end{bmatrix} \quad (2.5)$$

where $\phi = n_1 k_0 d$, and k_0 is the propagation constant. The reference transmittance was modeled as three layers of material, including a 0.5 µm diamond, a 19 µm layer of water and another 0.5 µm layer of diamond suspended in air. The first boundary between air and diamond was modeled using Eq. (2.4), and the rest was modeled by means of Eq. (2.5) The sample transmittance in the micro channel is modeled as five layers of thin film: 0.5 µm layer constituted by the top diamond window, represented by the 3.5 µm water layer over the cell, a 12 µm layer given by the algae, a 3.5 µm layer of water under the cell, and another 0.5 µm layer given by the lower diamond window. The refractive index of diamond (2.4) and air (1) were considered as constant values across the entire spectra. Algal cell and water were assumed as absorbing materials with complex refractive indexes, which were calculated by the method described in Section 3.3.1 using a standard spectrum and Kramers-Kronig relation. The water infrared spectrum was extracted from the KnowItAll spectral collection (KnowItAll, 2017), and the algal cell standard was estimated by the method explained in the supplementary materials. The absorbance is defined, starting from transmittance:

$$A = -\log\left(\frac{T_{ref}}{T_{samp}}\right) = \log(T_{samp}) - \log(T_{ref}), \quad (2.6)$$

where A is absorbance, T_{ref} is the background transmittance, and T_{samp} is the sample transmittance.

2.5   Fringe Correction

Fringes were removed with an Extended Multiplicative Signal Correction (EMSC) method. EMSC is a model-based preprocessing technique that is extensively used for preprocessing of IR

microspectroscopy data; it is based on Lambert-Beer law on the vibrational absorbance of materials. It models the absorption spectrum of a sample as the sum of its theoretical components. The EMSC model that is used to remove complex fringe patterns from spectra is the extension of the model presented by Konveskikh et al. (Konevskikh, Ponossov, Blümel, Lukacs, & Kohler, 2015) and is defined as

$$A(v) = a + b * m(v) + \sum_i [d_i \cos(x_i v) + d_{i+1} \sin(x_i v)] + e * v + \varepsilon(v), \quad (2.7)$$

where A is the absorption spectrum, v is the wavenumber, $m(v)$ is the standard spectrum, b is the scaling factor, $e * v$ represent the linear effects, and $\varepsilon(v)$ is the noise combined with the spectral structures that are not accounted for by the model. One period of the fringe in the wavenumber domain is $2\pi/x$. Eq. (2.7) could be written in the matrix format as

$$A = M_{sc}P + E, \quad (2.8)$$

where p is the fitting parameter vector, containing a, b, d_i, d_{i+1} and e, which is found by least-squares regression of each spectrum onto M_{sc}. M_{sc} is the matrix of model spectra and is defined as

$$M_{sc} = \begin{bmatrix} 1 & m(v_1) & \sin(x_1 v_1) & \cos(x_1 v_1) & ... & v_1 \\ 1 & m(v_2) & \sin(x_1 v_2) & \cos(x_1 v_2) & ... & v_2 \\ \vdots & \vdots & \vdots & \vdots & \vdots & \vdots \\ 1 & m(v_k) & \sin(x_1 v_k) & \cos(x_1 v_k) & ... & v_k \end{bmatrix}, \quad (2.9)$$

where k is the number of wavenumbers. The standard spectrum $m(v)$ is being approximated in 5 steps:

1) Water absorption regions of 2946-2489 cm^{-1}, 2219-1702 cm^{-1}, and 1581 to 950 cm^{-1} are set to zero.

24

2) The average spectrum of the hyperspectral data is calculated, as the base of the standard spectrum. It is considered that there are minimum fringes present in the average spectrum.

3) Regions of [1585, 962] and [2780, 1766] cm^{-1} are baseline corrected, separately.

4) The region of 1766 to 2790 cm^{-1} is replaced with corresponding region of standard Matrigel, that is a gelatinous protein mixture (Matrigel, n.d.).

5) The resulting spectrum is normalized at Si-O peak at 1076 cm^{-1}.

For the case of two parallel windows, with a distance d, a sinusoid with a constant frequency depending on the optical parameters of the assembly is added to the spectrum. Thus

$$d = \frac{N}{2n\Delta v} \quad (2.10)$$

Δv, and n is the refractive index of the water layer. The water thickness was determined to be between 20 to 25 µm in the measurements. The corresponding angular frequency of the fringe is 0.0052 to 0.0465 rad/cycle. The Fast Fourier transform (FFT) of the absorbance spectrum for the spectral region between 1766 to 2790 cm^{-1}, where the signal is dominated by the fringe effect, was calculated to determine the fringe frequencies of each spectrum, since there are no absorption bands in this spectral range. A short spectral region in the absorbance spectrum was chosen to calculate the FFT, and then used to calculate the frequencies that expand across the entire spectral range. To accurately detect the frequency components for such a short range of information, many frequency components are required. Spectra are zero padded in the wavenumber domain to increase the frequency resolution in the Fourier domain. In the Fourier domain, the first 10 dominant frequencies between 0.0052 to 0.0465 rad/cycle are chosen as the fringe frequencies. In the result and discussion section, we show that the dispersion impact was negligible in the micro channel, and the fringe pattern could be estimated by inserting these frequencies into Eq. (2.7). To

25
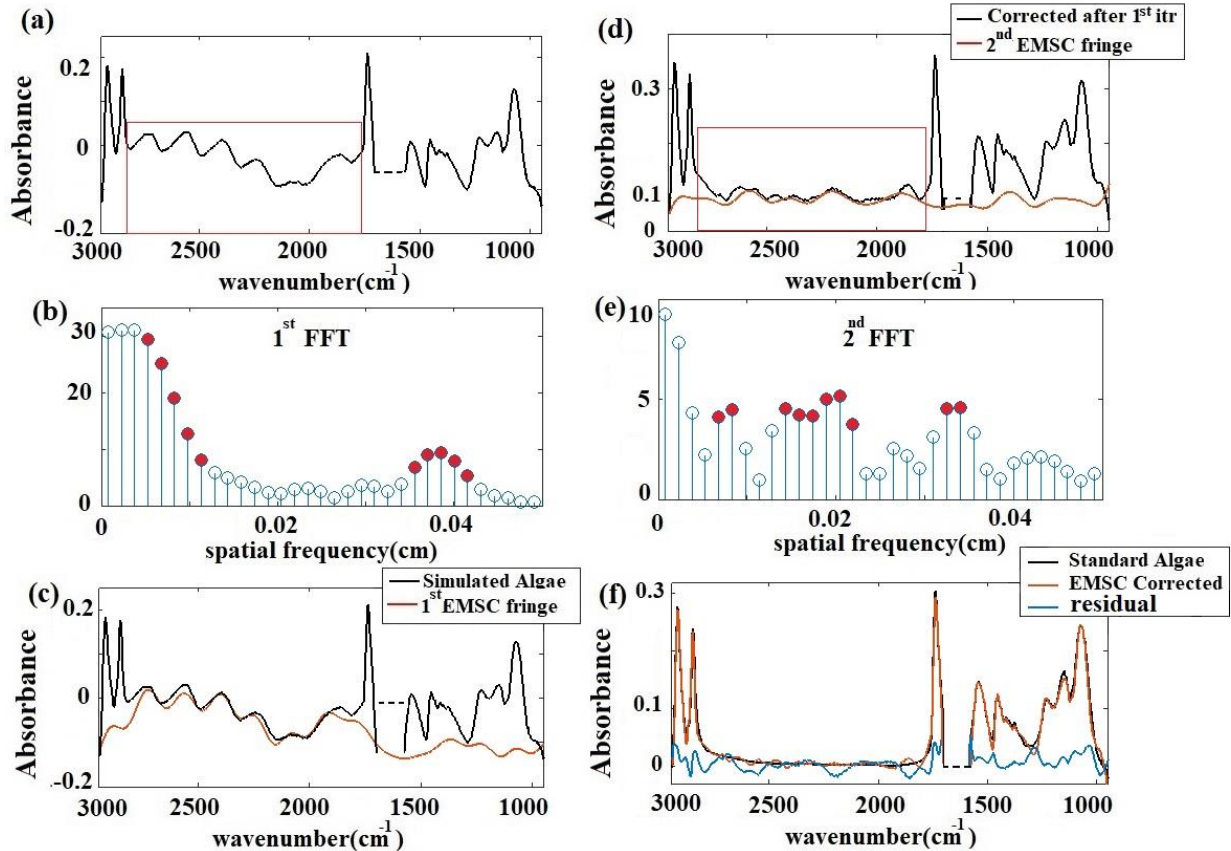
Figure 9 (a) Simulated algae spectrum with the method of Section 2.2. The red box shows the region chosen for estimating fringe frequencies. (b) FFT of the spectrum shown in red box in Figure 9 (a). Strength of the frequency components determined from the FFT. Red circles show the frequencies that are chosen for calculating the fringe pattern. (c) The estimated spectral fringes pattern (red) and the simulated algae spectrum (black). (d) Corrected spectrum after the first iteration(black) and the estimated fringe pattern at the second iteration(red). (e) FFT of the black curve in spectral region of 1766 to 2790 cm^{-1}. (f) EMSC corrected signal(red) after two iterations compared to the standard algae spectrum (black).

remove the fringes, the approximated fringe pattern was subtracted from the raw spectrum. This procedure was repeated until no fringes were observed across the region of 1766 to 2790 cm^{-1}.

Figure 9 (a) shows the simulated algae spectrum. The red box shows the region chosen for estimating fringe frequencies. Figure 9 (b) shows the FFT of the spectrum in the red box in Figure 9 (a). Red circles show the frequencies that are chosen for calculating the fringe pattern. Figure 9 (c) shows the estimated spectral fringes pattern (red) and the simulated algae spectrum (black). Figure 9 (d) shows the corrected spectrum after the first iteration(black) and the estimated fringe pattern at the second iteration(red). Figure 9 (e) shows the FFT of the black curve in spectral region

26
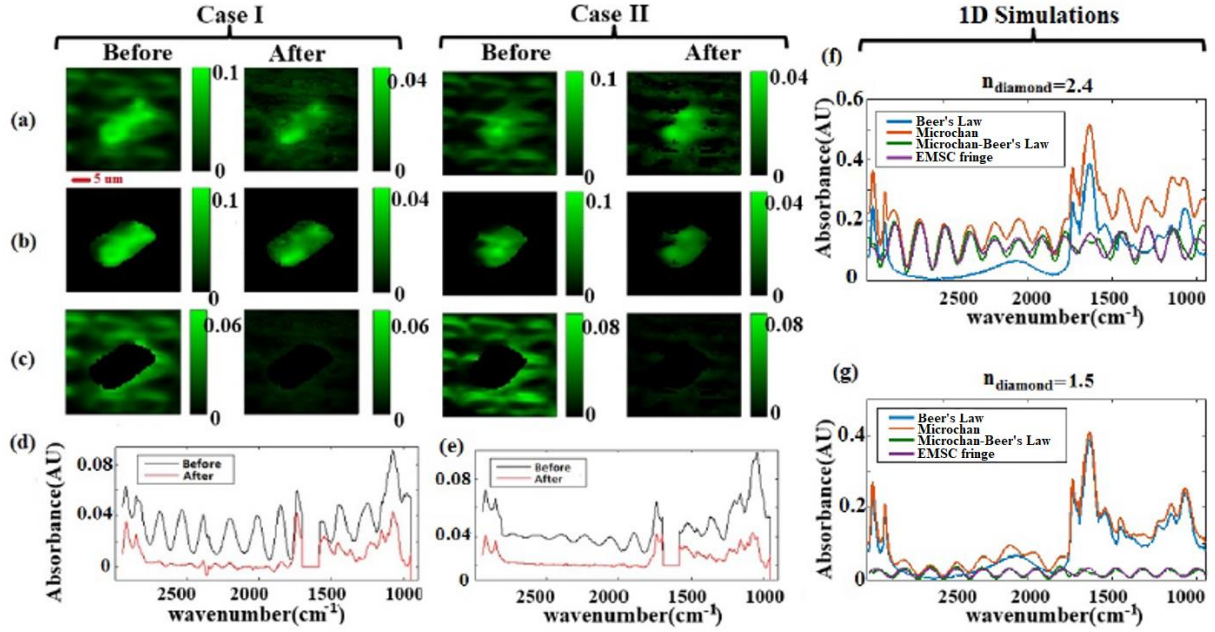
Figure 10 (a) The chemogram images for the two cases, before, and after correction, with black to green scale bar (black-green, low-high) (b) Pixels which are classified as cell by Otsu's method (c) Pixels which are classified as background. (d) Average spectra before and after fringe correction.

of 1766 to 2790 cm^{-1}. Figure 9 (f) shows the EMSC corrected signal (red) after two iterations compared to the standard algae spectrum (black).

2.6 Chemogram Image

To understand spatial variation of overall absorption of the sample, an integration under the spectral region (2947 cm^{-1} – 1693 cm^{-1} and 1585 cm^{-1} - 952 cm^{-1}), excluding the water region is calculated for each pixel. The resulting images, the so-called chemograms, reveal the overall absorption bands and the fringes. Examples are displayed in Figure 10 (a), with black to green scale bar (black-green, low-high).

27

2.7 Image Segmentation

Fringes dominate the spectra in the regions of the image where there are no algal cells, since there are no relevant chemical absorption bands at that point in space. A mask selects pixels that contain algal cell absorption signature for further chemical analysis. Our uniform approach for each IR image is as follows: 1) The integrated image of Si-O peak image at 1074 cm^{-1} is calculated 2) integrated image of silicate region 1058 to 1089 cm^{-1} is determined, 3) summation of these two integrated images is computed, 4) pixel spectra are divided into two class of cell and non-cell pixels.

Otsu's method is used to divide the images into two classes, defined as C1 = cell, and C2= background. Otsu's method is an optimum global thresholding method based on Bayes decision rule, which maximizes between class variance of 1D array, which is the normalized histogram of the images, in this study. The threshold found by this algorithm, selects 20% of the total pixel spectra, that are aligned with the visible images, and are known to be part of the algal cell. This approach facilitates automatic identification of all pixels for each cell at each time point.

2.8 Principal Component Analysis (PCA)

PCA reduces dimensionality of the data and facilitates further chemical analysis. It helps us to visualize chemical responses of algal cell to elevated CO_2. Spectra of the masked cube are decomposed into their largest variance components by PCA. Wavenumbers are considered as the PCA parameters. Approximately 5000 spectra are extracted from each individual algal cell replicate (8 measurements over time span of two hours) to identify the average spectrum and largest variance spatial components (PC2 and PC3). These spectra are fed into the MATLAB Statistics and Machine Learning Toolbox for PCA. To remove the effects of water and CO_2

28

absorption bands, only wavenumber ranges of 2946 to 2489 cm^{-1}, 2219 to 1702 cm^{-1}, and 1581 to 950 cm^{-1} are considered as PCA variable.

2.9 Results and Discussions

Two different cases of fringes are observed in the experiments. Case I: Fringes appear with a high amplitude in the average spectrum and a low contrast in the chemogram (Figure 10, Case I). Case II: Fringes appear with a low amplitude in the average spectrum and a high contrast in the images (Figure 10, Case II). The strength of the fringe pattern present in the data depends on the placement of the two diamond windows with respect to each other in replicates of the experiment. Figure 10 (a) shows the chemogram images, before and after fringe correction. The images are classified into two regions of cell, and non-cell by Otsu's method. Figure 10 (b) shows pixels considered as cell, and Figure 10 (c) shows pixels considered as background pixels. The average spectra before and after fringe correction are plotted in Figure 10 (d). Note that there are smaller spectral and spatial fringes in the chemogram images and the average spectra after correction. Importantly, fringe correction preserves the strong spectral features and even reveals peaks, such as the CO_2 band at 2360 cm^{-1} (due to varying atmospheric CO_2 in the optical beam path). In Figure 10 c), the background variation decreases after fringe correction in both cases and demonstrates that the spatial fringes attenuate after spectral fringe correction. Figure 10 (f) and (g) shows the simulated absorbance through the channel in two conditions. In Figure 10 (f), refractive index of the diamond is considered as 2.4, while in Figure 10 (g), the refractive index of the diamond is 1.5. In Figure 10 (f) and (g), the red spectrum shows the simulated transmittance through the channel by means of matrix theory of optical systems and considering the micro channel as a seven-layer system. The blue spectrum shows the result of Beer's law, considering the total absorption of the micro channel as addition of the absorbances of each single layer. The green spectra which looks

29

like sinusoidal is the subtraction of blue from red and demonstrates the fringe pattern all over the spectrum. Although the amplitude of the green fringe pattern changes with the wavenumber as shown in Figure 10 (f), the fringe pattern estimated by EMSC (shown by purple), accurately models the fringes. Dispersion effect is minimum in both cases, and estimated fringes in region of 1766 to 2790 cm^{-1} can be extended to all the spectral region. Konvskikh et al. showed that dispersion effect is minimum for samples with constant refractive index of less than 2.4. (Konevskikh, Ponossov, Blümel, Lukacs, & Kohler, 2015)

Reducing the data to principal components allows an overall assessment of data before and after correction. The PCA before and after fringe correction are shown in Figure 11 for two different CO_2 condition (ambient – control & LtoH – 5000 ppm). Figure 11 (a) and (b) show the first, second, and third principal components of the hyperspectral cube before any corrections. Figure 11 (c) and (d) shows the first, second, and third principal components after fringe correction. Original data variances were dominated by fringes. (Similar results were obtained for PCA of spectra with significant scattering contributions. Scattering features can dominate spectral principal components before preprocessing corrections). Once the spectral fringes were removed for each individual spectrum, spatial variations and spectral fringes were greatly reduced in the frequency dependent loadings of principal components (average, second and third principal components). After removing the fringes and applying PCA, the frequency dependent variance spectra showed signatures corresponding to lipid and carbohydrate associated bands of the spectra (Figure 11 (d)). The contributions of the second and third principal components to describing the overall spectra are less than 2% of the total variation. This result suggests that changes in the lipid and carbohydrate macromolecular pools are minimal, as one would expect for a cell maintained at constant, controlled conditions, and measured over a period of 75 minutes. Detecting these small

30

variations is possible only after applying data preprocessing algorithms. The results (PC loadings) of the analysis on three replicates are consistent and prove the reliability of the procedure.

While it is desirable to evaluate the distribution and time resolved modifications of macromolecular pools under controlled hydrated environment in viable algal cells, there are some challenges. The geometry of the microfluidic channel lead to infrared images that contain both spatial and spectral fringes. Interpretation and statistical analysis of spectra with fringes can be misleading and even impossible. Appropriately executed fringe correction substantially improves the quality of images and spectra and facilitates the analysis of the hyperspectral cube.

31
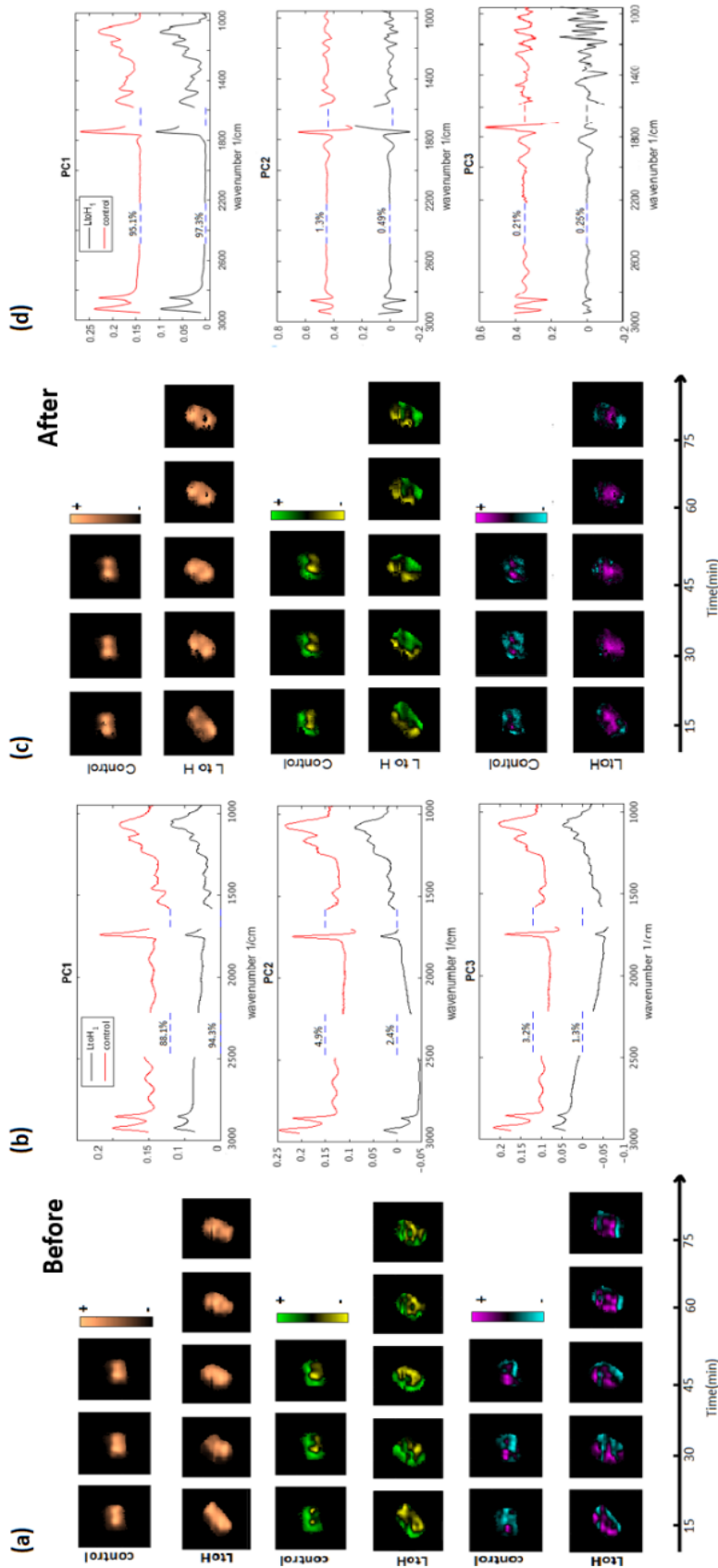
Figure 11 (a) PCA score images before fringe correction for control and stressed conditions. (b) PCA loading spectra before fringe correction. (c) PCA score images after fringe correction for control and stressed conditions. (d) PCA loading spectra after fringe correction.

المنارة للاستشارات

www.manaraa.com

Chapter 3

3   Spatial Coherence of the light source

A prototype measurement indicative of the ability of the FTIR imaging in revealing the phonotypic changes in cells was provided in Chapter 2. However, there are some limitation with this technique. For example, when the sample has semi-spherical inhomogeneities (that is the case for most of the biological materials), the measured spectra are distorted with scattering contributions.

In this chapter, it is shown that the scattering contributions in the pixelated spectra are related to the spatial coherency of the light source. United states air force (USAF) targets are measured with synchrotron and thermal sources. The results show evidence of distinct complex coherency factors in vertical and horizontal direction for synchrotron source, without this knowledge a spectroscopist might misinterpret the spectral information.

3.1   Introduction

Conventional Synchrotron Fourier transform infrared (FTIR) microscopy, along with advanced methods of data analysis has become an established method for chemical imaging of live biological cells (Holman H.-Y. N., Bechtel, Hao, & Martin, 2010) (Loutherback, Birarda, Chen, & Holman, 2016) (Miller, et al., 2006) (Didonna, Vaccari, Bek, & Legname, 2011) (Hirschmugl & Gough, 2012). However, scattering and absorption signatures (Bassan, et al., Resonant Mie Scattering (RMieS) correction of infrared spectra from highly scattering biological samples, 2009)in infrared microscopic imaging (pixelated data) are not well understood.

There are several studies about the mechanisms of light scattering from biological cells (Liu, Capjack, & Rozmus, 2005) (Su, Capjack, Rozmus, & Backhouse, 2007). It is shown that the non-homogeneities in cells are equivalent to spheres with relevant sizes and refractive indexes (Mourant, et al., 1998) (Tao Su, Capjack, Rozmus, & Backhouse, 2007).The results show that small organelles play a significant role in light scattering from cells, and the volume fraction of organelles affects both the total amount of the scattered light and the angular distribution of scattered light (Dunn & Richards-Kortum, 1996).

Several Mie scattering correction techniques for infrared spectroscopy of single cells have been published (Bassan, et al., 2010) (KOHLER, et al., 2008) (Dijk, Mayerich, Carney, & Bhargava, 2013) (Konevskikh T. , Lukacs, Bl˙umel, Ponossov, & Kohler, 2015). There is a tendency to apply these algorithms for correcting the scattering contributions in the pixelated spectra. While these algorithms have successfully corrected the scattering in the spectral microscopic imaging, we have encountered many situations where they failed. Scattering is dependent on the chemical and physical properties of the sample, and the apparent scattering contribution in the measured pixelated spectra is dependent on the numerical aperture and the point spread function of the microscope. In this chapter we are pointing to the source contribution in the apparent scattering. Here, the relation between the spatial coherency of the source and the spatial contribution of the scattering in the pixelated data is highlighted.

The light observed at the detector is the interference pattern of the incident light and the light scattered by the sample. Scattering is angular dependent as shown in Figure 12 (a). In a regime

34
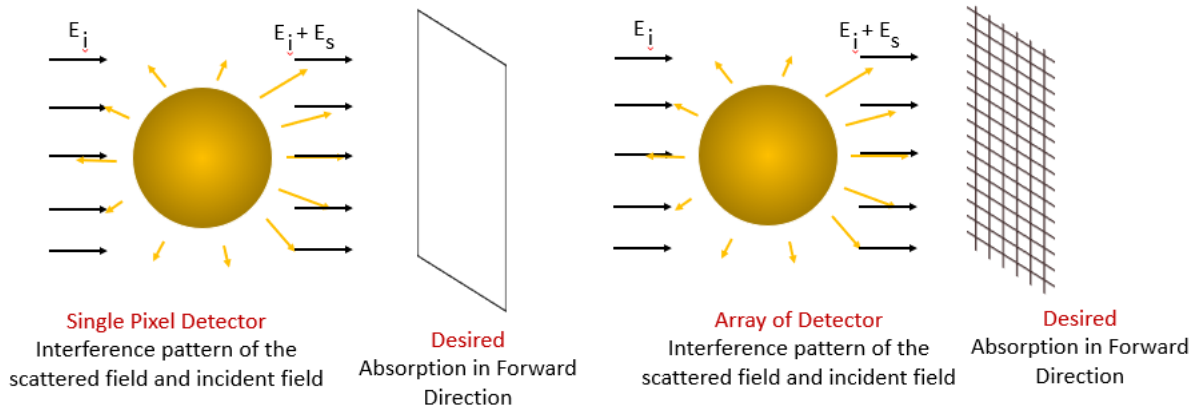
Figure 12 Interference of the scattered light and incident light is spatially varying.

where the geometric cross section of a sample g is smaller than the area of the detector G (G > g) for rotationally invariant scatterers, the extinction cross section does not depend on the spatial coherence of the source (Greffet, Cruz-Gutierrez, Ignatovich, & Radunsky, 2003). In the case of chemical imaging, the light is detected by an array of detectors (G < g). In this regime (G < g) the amount of the scattered light is spatially varying Figure 12 (b), and the observed interference pattern is dependent on the tendency of the incident light to interfere with the scattered light (Fischer, Dijk, Visser, & Wolf).

Spatial coherence is a property of light that describes the correlation between two points in the space and the ability of the two points to interfere in extent of wave in averaged time (Deng & Chu, 2017). Consider two analytic signals $\boldsymbol{u}(r_1, t)$ and $\boldsymbol{u}(r_2, t)$ observed at two space points r_1 and r_2 with zero relative time delay. When $r_1 = r_2$, the two waveforms are perfectly correlated. As r_1 moves further away from r_2 some degree of correlation loss can be expected.

The mutual intensity of the light at pinholes r_1 and r_2 is defined as

$$J_{12} = \langle \boldsymbol{u}(r_1, t)\boldsymbol{u}^*(r_2, t) \rangle. \qquad (3.1)$$

35

J_{12} shows the degree of correlation between two signals. The complex coherence factor of the light is

$$\mu \triangleq \frac{J_{12}}{[I(r_1)I(r_2)]^{1/2}}, \qquad (3.2)$$

where $I(r_1)$ and $I(r_2)$ are the intensity of the light at points r_1 and r_2. Van Cittret-Zernike theorem (Zernike, 1938) (Cittert, 1934) (Dorrer, 2004) relates the spatial coherence between two points of the wavefront with the shape and the intensity of the light source as well as the wavelength and distance of the propagation. This theory defines a quantity of Eq. (3.2) as follows,

$$\mu(r_1 - r_2, z) = \exp(j2\pi \frac{|r_1^2 - r_2^2|}{2\lambda z}) \times \frac{\iint_s I(x,y) \exp\left[-j2\pi\left(\frac{x_2 - x_1}{\lambda z}x + \frac{y_2 - y_1}{\lambda z}y\right)\right]dxdy}{\iint_s I(x,y)dxdy}. \qquad (3.3)$$

where $\vec{r_1} = x_1 i + y_1 j$, and $\vec{r_2} = x_2 i + y_2 j$, are two points in space, s is source size and $I(x, y)$ is the intensity distribution of the light source. For a uniform square non coherent source of a side length of a, and place a set of double slits of pitch b after the source at distance z, when $I(x, y) = 1$ within the emitting area, Eq. (3.1) becomes

$$\mu(\lambda) = \left|\frac{\sin\left(\frac{ab\pi}{\lambda z}\right)}{ab\pi/\lambda z}\right| \quad (3.4)$$

Notice that the $|\mu|$ depends only on the $(\Delta x, \Delta y)$. The coherence area A_c is defined as:

$$A_c \triangleq \iint_{-\infty}^{\infty} |\mu(\Delta x, \Delta y)|^2 \Delta x \Delta y \qquad (3.5)$$

Synchrotron radiation has spatial coherence properties (Coisson, 1995) (Huang, 2013), while thermal radiation, consisting of a large number of independent spontaneous emission from a collection of excited atoms or molecules, shows very small spatial coherence properties. (Goodman, Statistical Optics, 1985) Gonzaga-galeana has shown that absorption of a sphere is

36
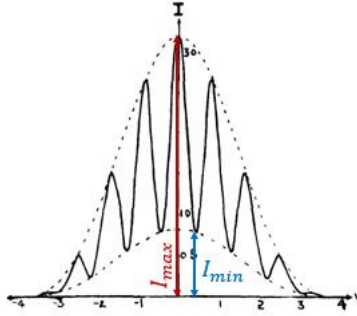
Figure 13 Fringe pattern of a Yong's double slit

controllable by changing the spatial coherence of the source (GONZAGA-GALEANA &
ZURITA-SÁNCHEZ, 2018). It is crucial to consider the light source in interpretation of any
image. Synchrotron and thermal light sources are currently employed in FTIR imaging, and
broadband infrared laser sources are in their early stages of production. Lasers are known as fully
coherent light sources, while synchrotron and thermal sources (like flashlights) are partially
coherent and non-coherent respectively. Coherency of the light can have profound effect in the
diffraction limited imaging, and it is important to be acknowledged in the analysis of hyperspectral
cubes of data.

The spatial coherence property of a synchrotron and a globar source is investigated by looking
at the visibility of the fringe pattern in Young's experiment with 3 slits. In order to understand the
effect of the spatial coherency on the broadband infrared images, the chemical images of a
microsphere measured by both sources are presented.

It is shown that in diffraction limit imaging, that the size of the sample is in the same range as
the wavelength of the light, a source with a higher complex coherence factor can more profoundly
stimulate electromagnetic shape resonances inside of the sample, resulting in spatially varying
spectra for a homogenous sample.

37

3.1.1 Experiment

A FTIR Bruker Hyperion 3000 microspectrometer with a focal plane array (FPA) detector is used for the measurements. The source of the microspectrometer was switch between a thermal source and synchrotron source (Infrared Environmental Imaging at the synchrotron radiation center) for the measurements. A 20x (0.6 NA) condenser objective and a 74x objective (0.6 NA) was used for illumination and collecting the transmitted radiation onto the detector, where a geometrical sample of 0.54x0.54 μm^2 per pixel was obtained.

A positive high-resolution USAF target is measured and the fringe pattern of the element 1 of group 8 with bar thickness of 3.9μm is investigated. Due to the Van Cittret-Zernike theorem the wave fronts smooth out as they propagate away from the source. Degree of spatial coherence μ or visibility of a source is measured as follows:

$$\mu = \frac{I_{max} - I_{min}}{I_{max} + I_{min}} \qquad (3.6)$$

Where I_{max} is the maximum observed intensity and I_{min} is the first observed minimum in the fringe patters as shown in Figure 13. A high value of visibility implies that the light beam passed through each bar of the target can interfere more strongly at the image plane. The calculated
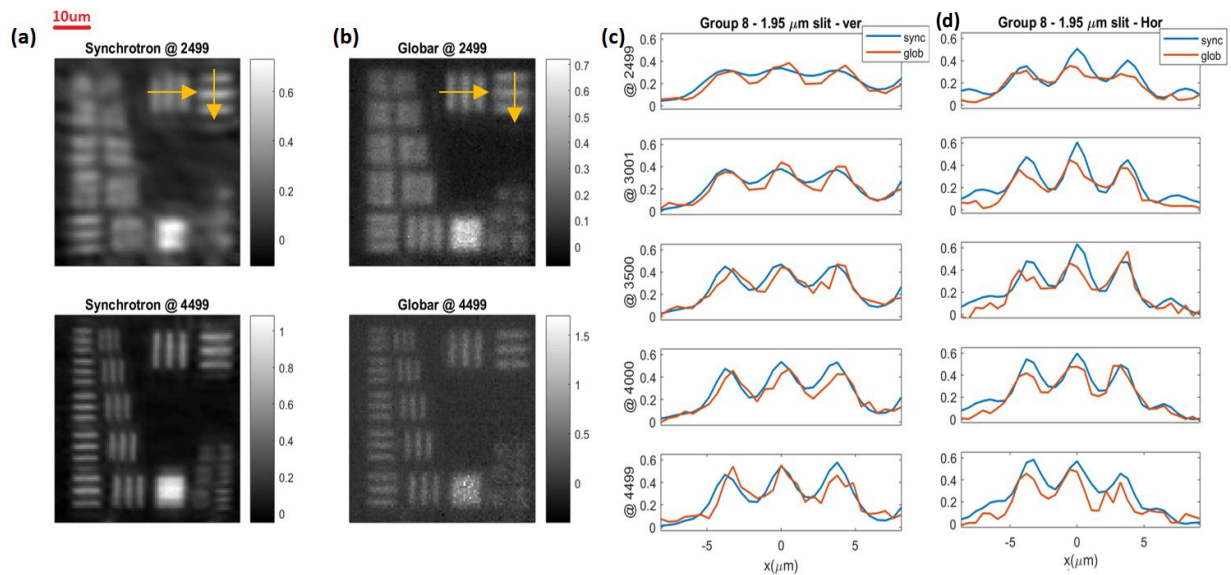
Figure 14 Synchrotron Vs Globar measurements. (a) Synchrotron image at 2499 cm⁻¹. (b) Globar image at 2499 cm⁻¹. (c) Synchrotron image at 4499 cm⁻¹. (d) Globar image at 4499 cm⁻¹. (f) Line scans through vertical slits of element 1 Group 8 at wavenumbers of 2499, 3001, 3500 and 4499 cm⁻¹. (e) Line scans through Horizontal slits of element 1 Group 8 at wavenumbers of 2499, 3001, 3500 and 4499 cm⁻¹.

visibility is smoothed out with Savitzky- Golay filter with polynomial order of 3 and frame length of 31.

For the microsphere measurements, A 20µl droplet of a solution containing Poly (methyl methacrylate) PMMA microsphere with 16-40 µm radius was dropped on a glass slide. A single bead with 25 µm radius was casted by a small hook that was dipped in glue. Measurements were done by a FTIR Bruker Hyperion 3000 micro spectrometer, coupled to a source channel, which could be switched between a globar source and a Synchrotron (SRC at IRENI). A focal plane array detector (128 x 128 pixels) with a 20x (0.6 NA) condenser, and A 36x (0.5 NA) objective were used to reach pixel sizes of 1.1×1.1 µm^2.

3.1.2 Results

Figure 14 (a) and (b) shows the images of the USAF target at 2499 cm⁻¹ and 4499cm⁻¹ measured by a synchrotron and a globar source respectively. The images measured by synchrotron has higher
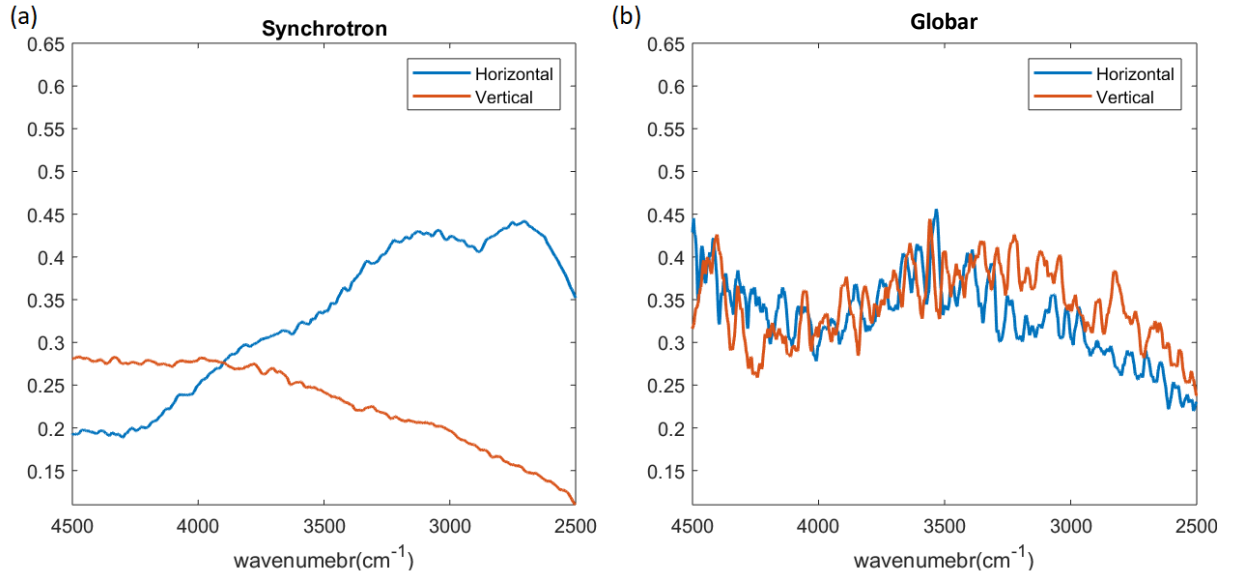
Figure 15 (a) Visibility of the synchrotron source as a function of wavelength for group 8- element 1 of the USAF target in horizontal and vertical directions. (b) Visibility of the thermal source as a function of wavelength for group 8- element 1 of the USAF target in horizontal and vertical directions.

quality compare to the globar. Looking at the synchrotron image at 2499 cm^{-1}, where the element 1 of group 8 is present, extra side lobes are observed especially for the horizontal bars. Figure 14 (c) shows the line scans through the vertical bars of group 8 element 1 for both synchrotron and globar at 2499 cm^{-1}, 3001 cm^{-1}, 3500 cm^{-1}, 4000 cm^{-1} and 4499 cm^{-1} wavenumbers, the line scans are along the yellow arrow shown in the images. Three fringe peaks corresponding to the three bars are observed in the line scans. Figure 14 (d) shows the line scans through yellow arrow along the vertical bar for four different wavenumbers, 2499 cm^{-1}, 3001 cm^{-1}, 3500 cm^{-1} and 4499 cm^{-1}. 3 peaks corresponding to the 3 vertical bars of the USAF target are present in the line scan of the images measured with globar source at 2499 cm^{-1} and 3001 cm^{-1}, 3500 cm^{-1}, 4000 cm^{-1} and 4499 cm^{-1}. The line scans through the vertical bars for the synchrotron source has 5 peaks at 2499 cm^{-1}, 3001 cm^{-1}, 3500 cm^{-1}, 4000 cm^{-1} and 4499 cm^{-1}.

Figure 15 (a) shows the calculated visibility of the synchrotron source in horizontal and vertical directions. The visibility of the vertical bars is constant between 4499 cm^{-1} and 3950 cm^{-}

[1], and then starts to decrease with the wavenumber (resolution decreases). The visibility of the horizontal bars remains constant between 4500 cm^{-1} and 4300 cm^{-1}. It increases from 4300 cm^{-1} to 3050 cm^{-1}, and then reduces from 3050 cm^{-1} to 2877 cm^{-1}, then goes up till 2703 cm^{-1}, and finally it decreases till 2500 cm^{-1}. Figure 15 (b) shows the vertical and horizontal visibility for the globar source in the vertical and horizontal direction. The measured visibility is noisy for the globar source. The visibility trend is similar in both vertical and horizontal directions. It reduces from 4500 cm^{-1} to ~4050 cm^{-1} and then start to incline from 4050 cm^{-1} to 3500 cm^{-1} and then it decreases from 3500 cm^{-1} to 2500 cm^{-1}.

Figure 16 shows the measurements of the 25µm radius PMMA bead with the synchrotron and globar light sources. Figure 16 (a) shows the absorption image of the PMMA bead at 1728 cm^{-1} measured by synchrotron. Figure 16 (b) shows the corresponding PMMA image by a globar source. Figure 16 (c), and 15 (d) shows a stack of spectra from center to the edges of the sphere, along vertical and horizontal direction. The top panel is a spectrum from the pixel at the edge of the sample, that is marked with a yellow square in the image. The chemical images measured by the globar source are noisier compare to the synchrotron source. In Figure 16 (c) and (d) the measured spectra with globar are plotted with blue and the ones measured with synchrotron are plotted with red color. Slow oscillatory variations (wiggles) are observed in the baseline of the spectra measured with the synchrotron source, these baseline variations in the synchrotron results are dependent on the location of the pixel. A constant baseline is observed in all the pixels measured by the globar source. High frequency ripple structure features are observed at spectra of the close to the edges of the sample for the synchrotron source, these structures cannot be detected by the globar source, because of the low signal to noise ratio. The absorption peaks of the PMMA at low frequency region in both horizontal and vertical directions are attenuated.

41
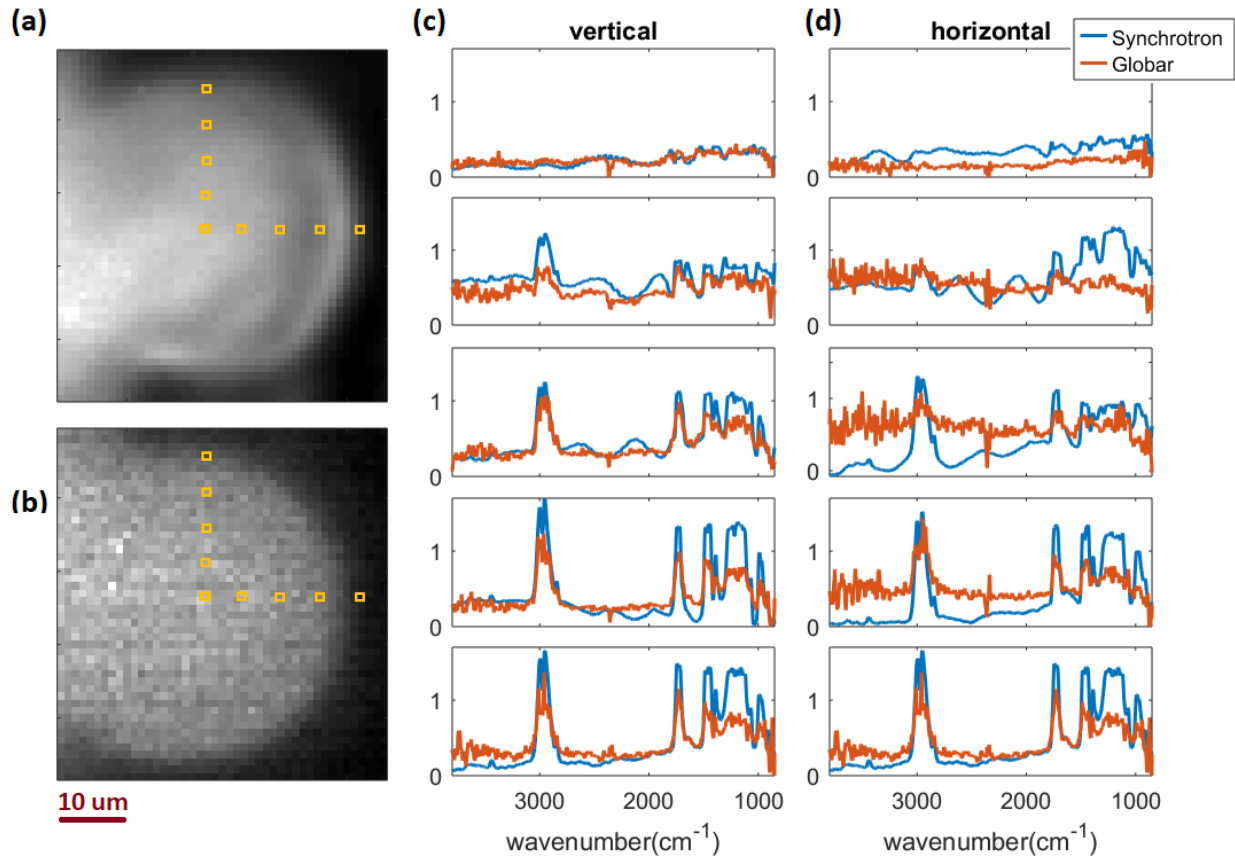
Figure 16 Heper spectral Image of a 25 um radius Poly(methyl methacrylate) (PMMA) microsphere (a) Absorbance image at 1728 cm^{-1} measured with a synchrotron source. (b) Absorbance image at 1728 cm^{-1} measured with a thermal (Globar) source. (c) Infrared specra along the red arrow. The top panel shows the spectra from the center of the sphere located at 0x0 and the bottom panel shows the spectra at 0x20.9.

3.1.3 Discussion

The extra side lobes in the line scans through the horizontal bars of the group 8 element 1, that are shown in Figure 14 (d) are related to the higher spatial coherency of the synchrotron source along the red arrow. Using multibeam synchrotron source result in different spatial coherency factors along different directions. At the IRENI beamline a large fan of radiation from a dedicated bending magnet was splitted into 12 beams and subsequently rearranged these into a 3x4 matrix beam bundle to illuminate a large field of view (Nasse, et al., 2011). Freitas et al., report an important improvement related to the beamline optics by extracting only one beam along the bending magnet radiation. (FREITAS, et al., 2018).

42

The visibility trends shown in Figure 15 (a) are consistent with the claim that the spatial coherency of the light source is not constant in the whole field of view along vertical and horizontal directions. It is expected that the visibility of the fringes (resolution) decreases with a decrease in the frequency of the light. However, for the synchrotron source the visibility along the horizontal bars increases as the frequency of the light decreases. The visibility trend for the globar source shown in Figure 15 (b) is distorted by noise, but with a rough estimate we could say that the visibility of the globar source is linearly decreasing with frequency of the light. The visibility of the globar source for wavenumbers larger than 3500 cm^{-1} is larger than synchrotron, the fringe pattern of the globar source shown in Figure 14 verifies that the fringe patterns of the globar source at wavenumbers 3500 cm^{-1} , 4000 cm^{-1} and 4499 cm^{-1} has five peaks instead of two. The presence of the peaks at the fringe pattern of the globar source is explained by the fact that the coherency of the signals passing through bars depends on the distance between the bars, the size of the source, so it is expected that the globar source show spatial coherent properties at some wavenumbers.

The visibility trends for other elements of the group 8 are also calculated and the result show similar behavior.

In Figure 16 (b) and (c) the spectra that are measured from the center of the sample have larger absorption peaks, compare to the one that are close to the edge. The baseline of the spectra measured with the globar are constant across the spectral range, while the baseline of the spectra measured with synchrotron changes pixel to pixel. We relate this phenomenon to the difference in spatial coherence of the two sources. If the diameter of the sphere is smaller than the skin depth ($\delta = \frac{\lambda}{4\pi n_i}$), the absorbed power by the sphere depends complicatedly on the complex coherence factor of the source (GONZAGA-GALEANA & ZURITA-SÁNCHEZ, 2018). The sample that is

43
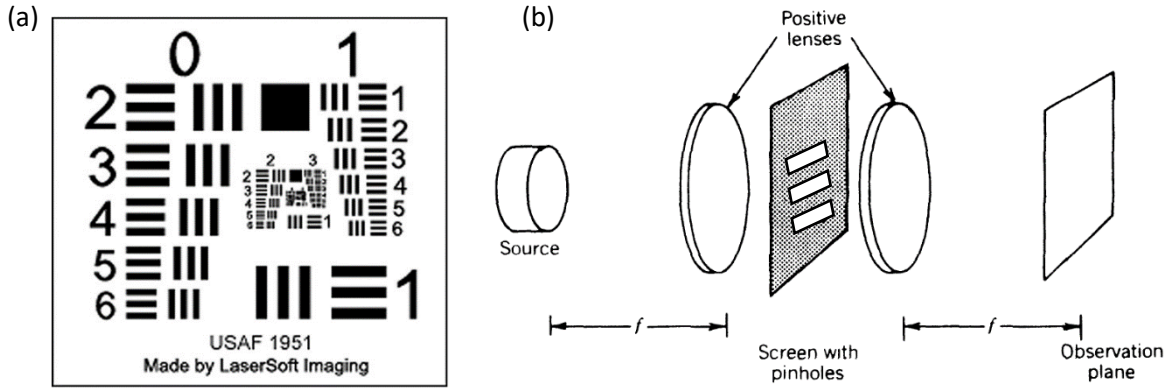
Figure 17 (a) USAF Target. (b) Simplified optical system made of a source, two positive lenses with focal length of f and three pinholes.

illuminated with a globar (non-coherent) source is responding to the randomly oriented plane waves, as a result the spectra are free of wiggle structures, that are due to the interference of the illuminated and the scattered light (Blˇumel, Baˇgcıoˇglu, Lukacs, & Kohler, 2016). On the other hand, the spectra that are measured by the synchrotron source have spatially varying wiggle structures. For a homogenous sphere imaged with a partially coherent source it is expected to observe similar wiggles structures in the spectra that are along the vertical and horizontal direction. However, the spectra measured with synchrotron source do not have similar wiggle structure along vertical and horizontal directions. Alike the extra side lobes observed for the fringe patterns of the USAF target along the horizontal direction, we relate this to the nature of light collection from the bending magnet at IRENI beamline (Nasse, et al., 2011). The appearance of the ripple structures at the spectra close to the edges of the sphere are the result of formation of electromagnetic shape resonances in the sphere.

Apart from the brightness (incident power), the globar and synchrotron sources, are distinct by their spatial coherency factor. Hence, the spatial interference patterns that are observed in the pixelated images measured by a synchrotron source are distinct from the ones measured with a globar source.

44
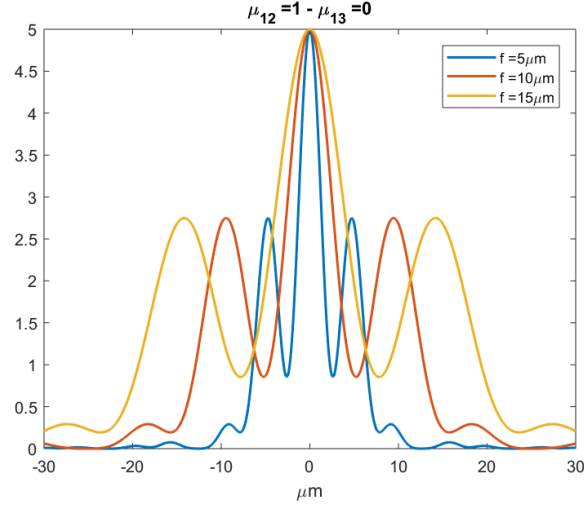
Figure 18 Fringe pattern at λ=4 µm, for slit width of 1.95 µm.

3.2   2D Measurement of spatial coherence for 3 slits

In order to gain insight on the amount of the spatial coherence of the sources, the fringe patterns of USAF target are fitted to the Fraunhofer diffraction pattern of three slits.

The imaging system used for measuring the USAF targets is simplified to the optical system shown in Figure 17 (b).

For three slits with width δ, and equal intensities $I(r_1) = I(r_2) = I(r_3) = I$, and monochromatic light, the interference pattern calculated by Fraunhofer diffraction pattern becomes:

$$I(x) = \left(\frac{A}{\lambda f}\right)^2 sinc\left(\frac{\delta}{\lambda f}x\right)^2 \times \left\{3 + 4\mu_{12}\cos\left(\frac{2\pi}{\lambda f}(\Delta\xi_{12}x + \alpha_{12})\right) + 2\mu_{13}\cos\left(\frac{2\pi}{\lambda f}(\Delta\xi_{13}x + \alpha_{13})\right)\right\}$$

(3.5)

Where A is the area of the pinholes, f is the focal distance of the lens, λ is the wavelength, μ_{12} is the complex coherence factor between pinholes 1 and 2, and μ_{13} is the complex coherence factor

45
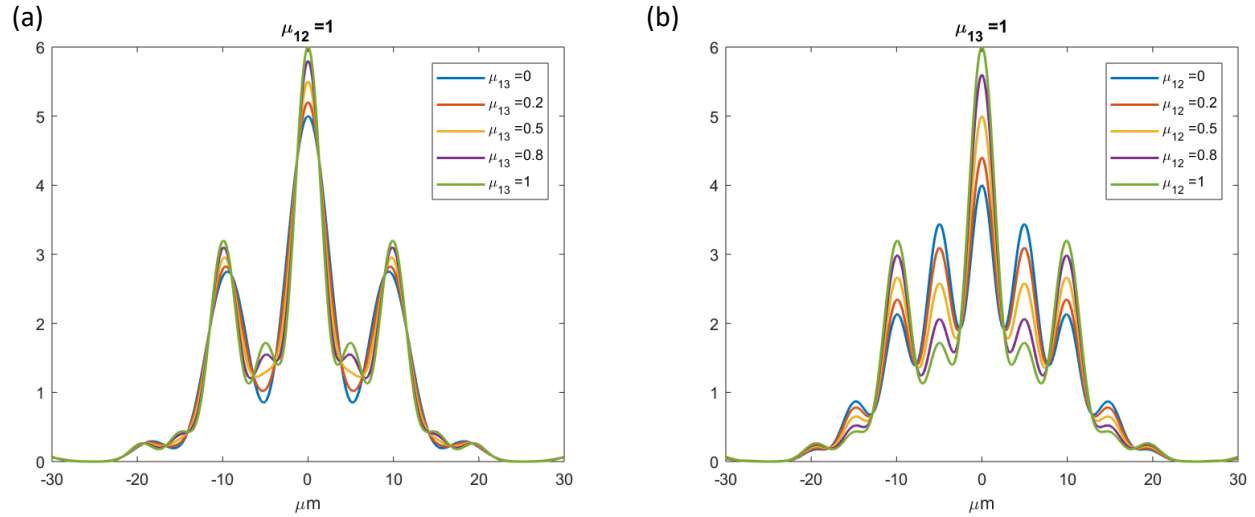
Figure 19 Interference pattern of 3 slits for slit width of 1.95µm at λ= 4 µm. (a) 100% coherency between slit 1 and 2, while the coherency between slit 1 and 3 is increasing. (b) 100% coherency between slit 1 and 3, while the coherency between slit 1 and 2 is increasing.

between pinholes 1 and 3. α_{12} is the phase difference of the light fields passing through pinhole 1 and 2. α_{13} is the phase difference of the light fields passing through pinhole 1 and 3. $\Delta\xi$ is the corresponding distances between the pinholes.

To understand the effect of spatial coherence factors (μ_{12} and μ_{13}), a set of simulations for Element 1 of group 8 of the USAF (width of 1.9 µm) at λ = 4 µm is done. Figure 17 shows that as the fringe patterns for 3 different values of effective focal distances. The FWHM of the fringe pattern at f = 10 µm is ~10 µm, which is corresponding to the magnification of ~1, so f = 10 µm chosen for the rest of the analysis.

Figure 19 (a) shows the interference pattern as the coherency between slit 1 and 2 increases. We can see that for μ_{13} < 0.5, only three strong interference patterns are observed, while for larger values of μ_{13} extra side lobes at ~ ±5 µm become present.

Figure 19 (b) shows the situation, where there is 100 % coherency between slits 1 and 3, and the value of μ_{12} is increasing from 0 to 1. Although the number of fringes remain constant in all cases, the intensity of the interference pattern increases as μ_{12} increases.

46

3.2.1 Curve Fitting

To measure spatial coherency factors, μ_{12} and μ_{13} for globar and synchrotron sources, the measured interference patterns (shown in Figure 14) at the center of a slit are normalized and then fitted to Eq. (3.5).

The fitting is done by least square linear regression. Eq. (3.5) is decomposed to its orthogonal components by forming matrix M as follows:

$$M =$$

$$\begin{bmatrix} 1 & 4S\cos\left(\frac{2\pi}{\lambda f}\Delta\xi_{12}x_1\right) & 4S\sin\left(\frac{2\pi}{\lambda f}\Delta\xi_{12}x_1\right) & 2S\cos\left(\frac{2\pi}{\lambda f}\Delta\xi_{13}x_1\right) & 2S\sin\left(\frac{2\pi}{\lambda f}\Delta\xi_{13}x_1\right) & 3S \\ 1 & 4S\cos\left(\frac{2\pi}{\lambda f}\Delta\xi_{12}x_2\right) & 4S\sin\left(\frac{2\pi}{\lambda f}\Delta\xi_{12}x_2\right) & 2S\cos\left(\frac{2\pi}{\lambda f}\Delta\xi_{13}x_2\right) & 2S\sin\left(\frac{2\pi}{\lambda f}\Delta\xi_{13}x_2\right) & 3S \\ \vdots & \vdots & \vdots & \vdots & \vdots & \vdots \\ 1 & 4S\cos\left(\frac{2\pi}{\lambda f}\Delta\xi_{12}x_n\right) & 4S\sin\left(\frac{2\pi}{\lambda f}\Delta\xi_{12}x_n\right) & 2S\cos\left(\frac{2\pi}{\lambda f}\Delta\xi_{13}x_n\right) & 2S\sin\left(\frac{2\pi}{\lambda f}\Delta\xi_{13}x_n\right) & 3S \end{bmatrix} \quad (3.6)$$

Where $S = 2\left(\frac{A}{\lambda f}\right)^2 \left[sinc(\frac{\delta}{\lambda f}x)\right]^2$.

By solving the equation of

$$Int(x) = Mp \quad (3.7)$$

where Int is the wavelength dependent interference pattern passing through the center of the slit, and $P = [p_1 \quad p_2 \quad p_3 \quad p_4]$ is the parameter vector. Then $\mu_{12} = \sqrt{p_2^2 + p_3^2}$, $\alpha_{12} = tan^{-1}\left(\frac{p_3}{p_2}\right)$, $\mu_{13} = \sqrt{p_4^2 + p_5^2}$, $\alpha_{13} = tan^{-1}\left(\frac{p_5}{p_4}\right)$.

Apart from the p, there is another unknown in Eq. (3.6) f, which is the focal length of the simplified imaging system shown in Figure 17 (b). To select a f value following steps are done:

47
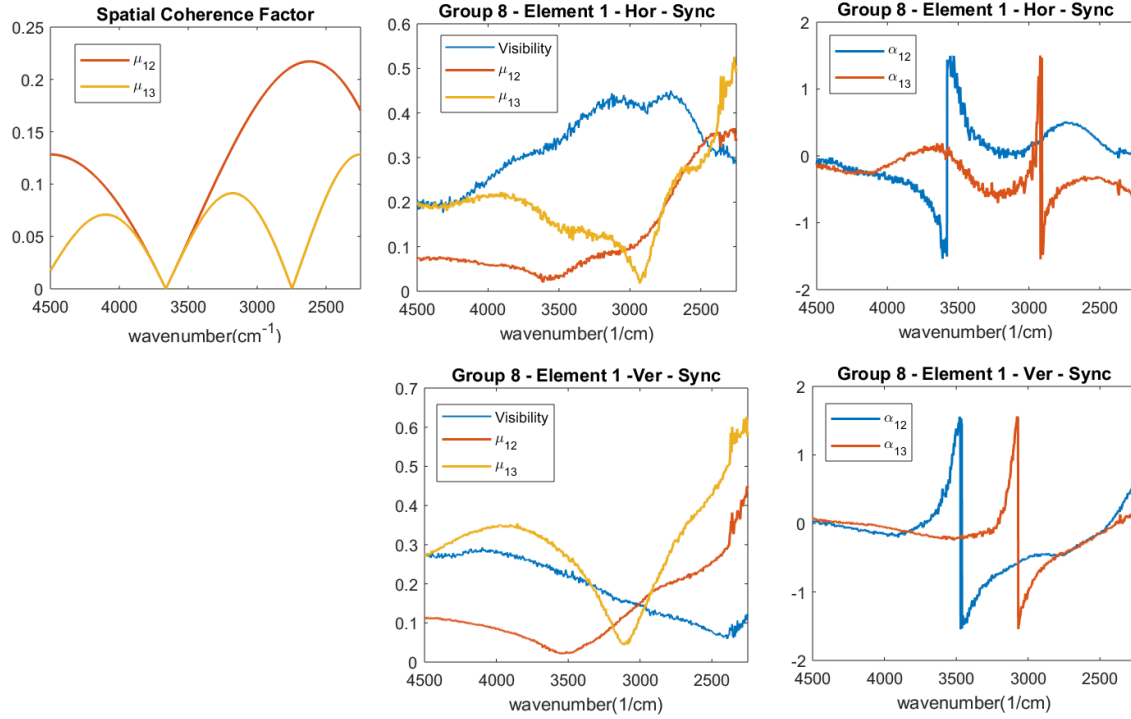
Figure 20 Spatial Coherence Factor for synchrotron source. (a) Simulated spatial Coherence factor μ_{12} ($\delta = 3.9\ \mu m$), and μ_{13} ($\delta = 7.8\ \mu m$). (b) Fitted values of spatial coherence factors for horizontal bars (group 8 – element 1). (c) Fitted values of α_{12} and α_{12} for horizontal bars (group 8 – element 1). (d) Fitted values of spatial coherence factors for vertical bars (group 8 – element 1). (b) Fitted values of α_{12} and α_{12} for horizontal bars (group 8 – element 1).

1) A range of f values (1 to 40 µm, with step size of 1 µm) are selected.

2) Curve fitting is done for each of these f values

3) The best fitted fringe and the corresponding f, μ_{12} and μ_{13} are selected based on

minimum error between the fitted interference pattern and the measured one.

3.2.1.1 Results

The values of μ_{12} and μ_{13} for a non-coherent light source after passing through slits are

predicted by Eq. (3.2) as shown in Figure 20 (a). In the simulations it is considered that the

condenser focuses the light in an area of 140x140 µm^2 (a = 140 µm), the sample (USAF, Group 8-

element1, b = 3.9 µm) has been moved up out of the focus of the condenser for roughly about 100

48
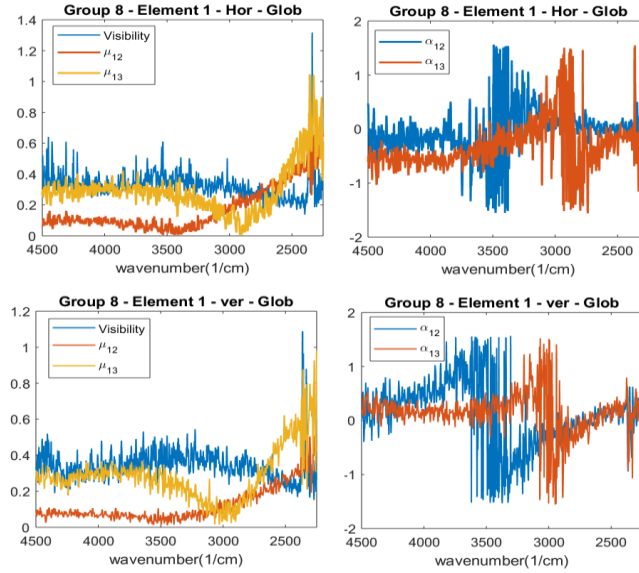
Figure 21 Spatial Coherence Factor for globar source. (a) Fitted values of spatial coherence factors for horizontal bars (group 8 – element 1). (b) Fitted values of α_{12} and α_{12} for horizontal bars (group 8 – element 1). (c) Fitted values of spatial coherence factors for vertical bars (group 8 – element 1). (d) Fitted values of α_{12} and α_{12} for horizontal bars (group 8 – element 1).

µm (z= 100 µm) to compensate for the light diffraction in the glass. Figure 20 (a) shows the simulated values for μ_{12} and μ_{13} for a non-coherent light source.

Figure 20 (b) to (e) shows the fitted values of μ_{12} and μ_{13} to horizonal and vertical bars of group 8 – element 1 with the method discussed in Section 3.2.1. The μ_{12} and μ_{13} curves measured for horizontal and vertical of bars have similar behavior .

Figure 21 shows the result of the same analysis for a globar source.

49

Chapter 4

4   Coherent Hyperspectral Image simulations

The hyperspectral image of a 25µm PMMA sphere is simulated by Green's function of the Maxwell's equation. The incident light is an ideal coherent plane wave propagating in the direction of the optical axis. The simulated image that is called a true image gives an insight on how a perfect hyperspectral infrared cube must looks like apart from the complexities introduced by measuring optics and the source. This information will guide us toward designing a new instrument for measuring infrared spectra.

Atomic force microscopy and infrared-spectroscopy (AFM-IR) is a method for measuring infrared spectra at the surface of a sample with nanometer spatial resolution. This method is derived by combining infrared spectroscopy and scanning probe microscopy. The spectra measured with this method have rapid sharp peaks that are usually considered as noise and are being smoothed out. Our simulations show that this spike features measured with AFM-IR are related to the nearfield components of the absorbed light. The measured spectral spikes possess information regarding to the physical shape of the sample, and they could be used for 3-dimensional reconstruction of the samples with super resolution.
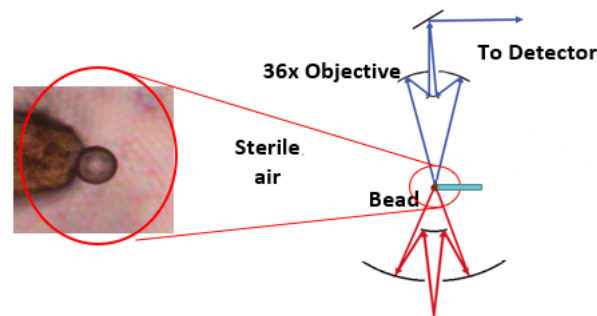
Figure 22 A visible image of the 25µm PMMA bead measured at IRENI. The scale bar is 20 µm.

On the other hand, it is considered that conventional FTIR measures only the far field components of the electric field. In order to gain an insight about the differences between the near field and far field spectra, the near field and far field spectra of a 25µm radius PMMA are simulated at the same image plane. In calculation of the far field spectra only the far field components of the Green's function are used.

4.1 Introduction

FTIR hyperspectral images are difficult to simulate and visualize. The result is inherently high-dimensional (x, y, z, λ) and needs a huge computational power. The Mie theory provides a rigorous solution to Maxwell's equations for a spherical scatterer. The theory has been used to characterize absorption in atmospheric simulations, to approximate cellular structures in spectroscopic imaging of biological tissues. (Berisha, Dijk, Bhargava, Carney, & Mayerich, 2017) In this chapter Green's function of the Maxwell's equation is provided to extend the former applications to non-spherical objects for infrared imaging.

In order to evaluate the numerical result calculated with the Green's function, a spherical scatterer is chosen, and the results are confirmed with Mie theory. The simulations are compared with experiment as well. The differences between the theoretical and the experimental results are explained by the fact that in the experiments the incident light is a partially coherent synchrotron beam, and the numerical aperture of the collective optics is not infinite.

4.2   2D Image simulation

To simulate the broadband infrared images of a micrometer size bead, first the complex refractive index of the material is measured by infrared spectroscopy of the corresponding thin films. By knowing the complex refractive index, the distribution of the electric field is simulated by Green's function of the Maxwell's equation (Economou, 1979) (Goedecke & O'Brien, 1988), and the results are confirmed by Mie theory (Bohren & Huffman, 1998).

The image is formed in the far field, where the near field components of the electric and magnetic field are considered as zero. The far field approximation of the electric field distribution is calculated by means of the free space Green's function of the Maxwell's equation.

To consider the nonidealities involved with the imaging system, the point spread function (PSF) - impulse response of the microscope - of the system is measured and convolved with the simulated images. The refractive index measurement, far field Green's integration and PSF convolution is explained in Sections 4.3.1, and 4.3.2. Finally, at the result section calculated images of a PMMA bead with 25 µm radius are shown.

52
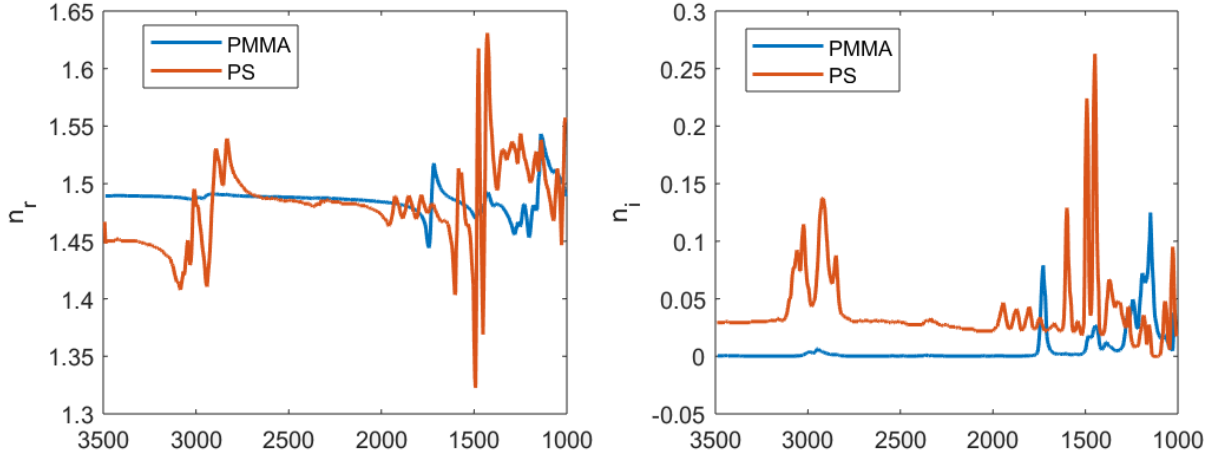
Figure 23 Complex refractive indexes of PMMA and PS thin film, calculated by absorption spectrum and the Kramers-Kronig's relation.

4.2.1 Refractive Index Calculation from Measured Spectra

In broadband infrared imaging, the refractive index of the material cannot be considered as a constant real value. The complex refractive index of a material can be obtained by knowing the constant real part of the refractive index and the pure infrared absorbance spectrum. The complex refractive index is defined as $n(v) = n_r(v) + in_i(v)$, where n_r is the real part and n_i is the imaginary part. The imaginary part of a refractive index of a thin film is proportional to its absorbance spectrum by Beer's law as follows

$$n_i = \frac{Aln(10)}{4\pi l v} \qquad (4.1)$$

where A is the absorbance spectrum, l is the thickness of the film, and v is the wavenumber. Knowing the imaginary part, the real part of the refractive index is calculated by the Kramers-Kronig relation,

$$n_r(v) = n_0 + \frac{2}{\pi} P \int_0^\infty \frac{s n_i(s)}{s^2 - v^2} ds \qquad (4.2)$$

53

where n_0 is the constant part of the real part of the refractive index, and P denotes the Cauchy principal value of the integral. Figure 23 (a) and (b) show the real and imaginary part of the refractive index for PS and PMMA thin films calculated by this method.

4.2.2 Wave Propagation by Far-field Green's Integral

4.2.2.1 The Green's function of the Maxwell's equation in free space

In mathematics, a Green's function is the impulse response of an inhomogeneous linear differential equation defined on a domain, with specified initial and boundary conditions. This method allows us to compute the electric and magnetic fields explained by Maxwell's equations.

The electric and magnetic-field vectors in a free space satisfy Maxwell's equations

$$\nabla . \vec{E}(\vec{r}, t) = 0, \qquad (4.3)$$

$$\nabla . \vec{B}(\vec{r}, t) = 0 \qquad (4.4)$$

$$\nabla \times \vec{E}(\vec{r}, t) = -\frac{\partial \vec{B}}{\partial t}, \qquad (4.5)$$

$$\nabla \times \vec{B}(\vec{r}, t) = \frac{1}{c^2}\frac{\partial \vec{E}}{\partial t} \qquad (4.6)$$

A necessary condition for $\vec{E}$ and $\vec{B}$ to satisfy Maxwell's equations is that each of their components satisfy the wave equation

$$\nabla^2 u(r, t) - \frac{1}{c^2}\frac{\partial^2 u(r,t)}{\partial t^2} = 0 \qquad (4.7)$$

The scalar function $u(r, t)$ represents any of the three components of the E_x, E_y, E_z or the three components of the B_x, B_y, B_z , Where $\vec{E}$ is the electric field, and $\vec{B}$ is the magnetic field, and

54

c is the speed of light. In a linear, homogeneous, and isotropic media, where we have stationary state, we can write

$$\vec{E}(\vec{r}, t) = \vec{E}(\vec{r})e^{i\omega t}, \qquad (4.8)$$

$$\vec{B}(\vec{r}, t) = \vec{B}(\vec{r})e^{i\omega t}. \qquad (4.9)$$

where $\omega = \frac{2\pi c}{\lambda}$. Stationary Maxwell equations are

$$\vec{B}(\vec{r}) = \frac{1}{i\omega}\nabla \times \vec{E}(\vec{r}), \qquad (4.10)$$

$$\vec{E}(\vec{r}) = -\frac{\mu}{i\omega\varepsilon}\nabla \times \vec{B}(\vec{r}), \qquad (4.11)$$

where μ is the magnetic permeability and ε is the electric permittivity. Applying $\nabla \times$ to the stationary Maxwell Eq. (4.10) and Eq. (4.11) yields the field equations.

$$\nabla \times \left[\nabla \times \vec{E}(\vec{r})\right] - n^2(\vec{r})k_0^2\vec{E}(\vec{r}) = 0, \qquad (4.12)$$

$$\nabla \times \left[\nabla \times \vec{B}(\vec{r})\right] - n^2(\vec{r})k_0^2\vec{B}(\vec{r}) = 0, \qquad (4.13)$$

where k is the wave vector $k = \frac{\omega}{c} = nk_0$ and $k_0 = \frac{2\pi}{\lambda_0}$, where $n(\vec{r})$ is the complex refractive index and λ_0 is the wavelength of the light in free space. Substituting the electric and magnetic fields $\vec{E}(\vec{r})$, and $\vec{B}(\vec{r})$ into the wave Eq. (4.12) yields the Helmholtz equations

$$\nabla^2 U + k^2 U = 0 \quad (4.14)$$

To solve the Helmholtz Eq. (4.14), the Green's function method can be used. The E&M Green's function is a 3×3 matrix (a tensor) given by

$$G(\vec{r}, \vec{r}') = \left\{\left(\frac{3}{k^2R^2} - \frac{3i}{kR} - 1\right)\hat{R}\hat{R} + (1 + \frac{i}{kR} - \frac{1}{k^2R^2})I\right\}g(R), \qquad (4.15)$$

55

where,

$$\hat{R} = \frac{\vec{r} - \vec{r}'}{|\vec{r} - \vec{r}'|}, \qquad (4.16)$$

$$g(R) = \frac{1}{4\pi} \frac{e^{ik|\vec{r} - \vec{r}'|}}{|\vec{r} - \vec{r}'|} = \frac{1}{4\pi} \frac{e^{ikR}}{R}, \qquad (4.17)$$

and,

$$I = \begin{bmatrix} 1 & 0 & 0 \\ 0 & 1 & 0 \\ 0 & 0 & 1 \end{bmatrix}, \quad (4.18)$$

is the unit tensor. The Green's function defined in (4.15) satisfies the field equation

$$\nabla \times \left[\nabla \times \vec{G}(\vec{r}, \vec{r}') \right] - k^2 \vec{G}(\vec{r}, \vec{r}') = I\delta(\vec{r} - \vec{r}'). \quad (4.19)$$

The $\hat{R}\hat{R}^*$ components of $G(\vec{r}, \vec{r}')$ is

$$\hat{R}\hat{R} = \begin{bmatrix} \hat{R}_x\hat{R}_x & \hat{R}_x\hat{R}_y & \hat{R}_x\hat{R}_z \\ \hat{R}_y\hat{R}_x & \hat{R}_y\hat{R}_y & \hat{R}_y\hat{R}_z \\ \hat{R}_z\hat{R}_x & \hat{R}_z\hat{R}_y & \hat{R}_z\hat{R}_z \end{bmatrix}, \qquad (4.20)$$

where $\hat{R}_x = (x - x')/R$, $\hat{R}_y = (y - y')/R$, $\hat{R}_z = (z - z')/R$. In the absence of magnetic

properties of the sample the electric field $\vec{E}(\vec{r})$ satisfies the Lippmann-Schwinger equation

$$\vec{E}(\vec{r}) = \vec{E}^{(incident)}(\vec{r}) + k^2 \int_{all\ space} [n^2(\vec{r}') - 1] G(\vec{r}, \vec{r}') \cdot \vec{E}(\vec{r}') d^3\vec{r}', \ (4.21)$$

where the integral extends over all space, $\vec{E}^{(incident)}(\vec{r})$ is the incident field (which can take

any shape or form), $k = \frac{2\pi}{\lambda}$ is the angular wavenumber, and λ is the wavelength. The validity of

(4.21) can be verified by inserting (4.21) into the field Eq. (4.12) using the theory of distributions

for $\vec{E}$ and observing (4.19).

56

In the case of interest in biology and chemistry, the index of refraction outside of the sample is $n = 1$. Using this information, we see immediately that the integral in (4.21) does not give any contributions outside of the sample, since outside of the sample the term $(n^2 - 1)$ is identically zero. Therefore, if we restrict our attention to the case where $n = 1$ outside of the sample, the Lippmann-Schwinger Eq. (4.21) simplifies to

$$\vec{E}(\vec{r}) = \vec{E}^{(incident)}(\vec{r}) + k^2 \int_{interior\ of\ the\ sample} G(\vec{r}, \vec{r}')[n^2(\vec{r}') - 1]\vec{E}(\vec{r}')d^3\vec{r}',$$

(4.22)

This is the key observation, which we are going to use for imaging. According to (4.22) we can obtain the electric field anywhere in space by knowing the inside field of the sample.

To obtain the field inside the sample, the scatterer is subdivided into several small volume elements in which the electric field vector is approximated by a constant value. This leads to the following discretized version of Eq. (4.22), that is

$$E_m = E_{0,m} + \sum_j G_{mj} (n_m^2 - 1).E_m,$$ (4.23)

where E_m and n_i are the electric field, and complex refractive index at volume element of m, and G_{mj} is defined as

$$G_m = \int_{V_j} G(r_m, r')k_0^2 d^3r',$$ (4.24)

where the position r_m represent the center of volume element m and V_j denotes that the integral is over volume j. In case with $m \neq j$, it can be acceptable to use the approximation

$$G_{mj} = G(r_m, r_j)k_0^2 V_j.$$ (4.25)

In the case when $m = j$, it is necessary to use a more precise method. In order to avoid integrating over the very strong singularity of G, the volume integral (4.24) is transformed to a surface integral (YAGHJIAN, 1980) (Lavrinenko, Laegsgaard, Gregersen, Schmidt, &

57

Sondergaard, 2017). By using (4.15) and (4.17) and the Gauss law G_{ij} at the source region could be calculated by

$$G_{mm} = -I + \oint_{\partial V_m} (\hat{n}'\nabla' - I\hat{n}'.\nabla')g(r_m, r')dA', \quad (4.26)$$

where ∂V_m is the surface of the volume element m. $\hat{n}'$ is the outward surface normal vector of volume element m at the position on the surface r'. dA' is the infinitesimal surface area. G_{mm} depends only on the shape of element m, and its position (Lavrinenko, Leagsgaard, Gregersen, Schmidt, & Sondergaard, 2014).

Integral (4.22) in spherical coordinate has the following form

$$\vec{E}(\vec{r}) = \vec{E}^{(incident)}(\vec{r}) + k^2 \int_{interior\ of\ the\ sample} G(\vec{r}, \vec{r}')[n^2(\vec{r}') - 1]\vec{E}(\vec{r}')r^2 sin\theta d\varphi d\theta dr.$$

(4.27)

For a spherical sample, Eq. (4.23) is

$$\vec{E}(\vec{r}) = \vec{E}^{(incident)}(\vec{r}) + k^2 \int_0^a \int_0^\pi \int_0^{2\pi} G(\vec{r}, \vec{r}')[n^2(\vec{r}') - 1]\vec{E}(\vec{r}')r^2 sin\theta d\varphi d\theta dr.$$

(4.28)

To calculate the image only far field components are considered. The terms with R^2 in the denominator vanish in the far field, and the Green's function of (Eq. (4.15)) reduces to

$$G(\vec{r}, \vec{r}') = \{-\hat{R}\hat{R} + I\}g(R). \quad (4.29)$$

Knowing the electric field, the magnetic field, H can be calculated by means of Eq. (4.11) and knowing $\vec{H} = \vec{B}/\mu_0$.

The intensity of the electromagnetic field is defined by mean of the pointing vector $\vec{S}(\vec{r})$ as followed

58

$$\vec{I}_{true}(\vec{r}) = \langle \vec{S}(\vec{r}) \rangle = \frac{1}{2\mu_0} \mathcal{R}[\vec{E}(\vec{r}) \times \vec{B}(\vec{r})^*], \qquad (4.30)$$

where the angular brackets indicate cycle averaging (Hetch, 1974).

For imaging purposes that the detector is located at the far field. The detected image is the dissipated power at the surface of FPA

$$P(\vec{r}) = \vec{I}_{true}(\vec{r}).\vec{A} . \qquad (4.31)$$

4.2.2.2 Integration Method: Gaussian Quadrature

In numerical analysis, a quadrature rule approximates the definite integral of a function, usually stated as a weighted sum of function values at specified points within the domain of integration. The integrand in Eq. (4.22) is periodic with respect to φ, with period of 0 to π , so the trapezoidal rule integration can be used along φ direction. θ is chosen as the Gaussian quadrature variable and w is an array containing the corresponding weight factors, so Eq. (4.22) is modified as follows

$$\vec{E}(\vec{r}) = \vec{E}^{(incident)}(\vec{r}) + k^2 \int_0^a \int_0^\pi \int_0^{2\pi} G(\vec{r},\vec{r}')[n^2(\vec{r}') - 1]\vec{E}(\vec{r}')r^2 sin\theta w d\varphi dr. \qquad (4.32)$$

Eq. (4.32) is implemented in MATLAB. The convergence of the technique is evaluated by Mie theory for spherical objects (Walter & Patch, 2018).

The convergence analysis of the integral is done in 3 dimensions, for 3 spheres with radius of 1, 3 and 25 µm at the shortest wavelength of 4000 cm^{-1} and complex refractive index of 1.3+0.1i.

N_r is the discretization in r, N_φ is the discretization in φ, and N_θ is the discretization in θ. The percentage error is calculated by calculating real part of E_x with different discretization (doubling in each dimension until the integral converges at each dimension) and then the relative error is

$$error = Re\{\frac{E_x(n) - E_x(n-1)}{E_x(n)}\} \times 100 .$$

59

As an example, the convergence analysis for the 1µm sphere is reported. First by keeping the value of N_r and N_θ constant the minimum value of N_φ, that makes the integral convergent along φ is chosen. The errors analysis for N_φ values are summarized in Table. 1.

Table 1 Convergence analysis for a 1µm sphere with refractive index of 1.3+0.1i at 4000 wavenumbers along φ

N_r	N_φ	N_θ	$\max(Re\{E_x(n) - E_x(n-1)\})$	error	CPU time (s)
129	9	9	3.58e-03	0.46	11
129	18	9	4.62e-09	0.00	38

$N_\varphi = 18$ is chosen, and then the convergence along r is checked. The result is summarized in Table. 2.

Table 2 Convergence analysis for a 1µm sphere with refractive index of 1.3+0.1i at 4000 wavenumbers along r

N_r	N_φ	N_θ	$\max(Re\{E_x(n) - E_x(n-1)\})$	error	CPU time (s)
17	18	9	6.03e-2	5.04	4
33	18	9	1.77e-2	1.50	7
65	18	9	4.41e-3	0.38	16
129	18	9	1.10e-3	0.09	29
257	18	9	2.74e-04	0.02	37
513	18	9	6.84e-05	0.01	53
1025	18	9	1.71e-05	0.00	46

Now the value of $N_r = 1025$ is chosen, and the convergence along the θ is analyzed as shown in Table. 3.

60

Table 3 Convergence analysis for a 1μm sphere with refractive index of 1.3+0.1i at 4000 wavenumbers along θ

N_r	N_φ	N_θ	$\max(Re\{E_x(n) - E_x(n-1)\})$	error	CPU time (s)
1025	18	9	2.01e-2	1.68	108
1025	18	18	3.21e-3	0.27	338
1025	18	36	1.35e-04	0.01	356

The value of $N_\theta = 36$ is chosen. Now for minimizing the value of N_r while we are sure that the integral is convergent along the other directions the convergence is checked by reducing the value of N_r as shown in Table. 4.

Table 4 Reducing the value of Nr for an efficient calculation for a 1μm sphere with refractive index of 1.3+0.1i at 4000 cm^{-1}.

N_r	N_φ	N_θ	$\max(Re\{E_x(n) - E_x(n-1)\})$	error	CPU time (s)
1025	18	36	7.24e-8	0.00	356
513	18	36	2.88e-7	0.00	162
257	18	36	1.16e-6	0.00	102
129	18	36	1.85e-05	0.01	50

Finally the values of $N_r = 257$, $N_\varphi = 18$ and $N_\theta = 36$ are chosen so the Green's integral converges for the sphere with radius of 1μm, refractive index of $1.3 + 0.1i$ at $4000 \text{ cm}^{-1} \equiv \lambda = 2.5$ μm.

The same analysis is performed for spheres with radius of 3μm and 25 μm, the corresponding values of N_r, N_φ and N_θ are showin in Table.5.

61

Table 5 Convergence Analysis for the Green's function for a sphere with refractive index of 1.3+0.1i at 4000 cm^{-1}.

r(μm)	N_r	N_φ	N_θ	CPU time (s)
1	257	18	36	102
3	257	36	36	194
25	513	72	144	1320

4.3   Experiment

A 20µl droplet of a solution containing Poly (methyl methacrylate) PMMA microsphere with 16-40 µm radius was dropped on a glass slide. A single bead with 25 µm radius was casted by a small hook that was dipped in glue. Measurements were done by a FTIR Bruker Hyperion 3000 micro spectrometer, coupled to a source channel, which could be switched between a Globar source and a Synchrotron (SRC at IRENI). A focal plane array detector (128 x 128 pixels) with a 20x (0.6 NA) condenser, and a 36x (0.5 NA) objective were used to reach pixel sizes of 1.1x1.1 µm^2. The measurement was done with two sources to compare the results.

4.3.1 Point Spread Function

PSF is the response of an imaging system to a point source. It shows the degree of spreading (blurring) of the point object and is a measure for quality of an imaging system.

PSF mimics diffraction effects, chromatic aberrations and other factors that distort the true image of the sample. Mathematically, the measured image, and the true form of the object, are related by the following equation

62
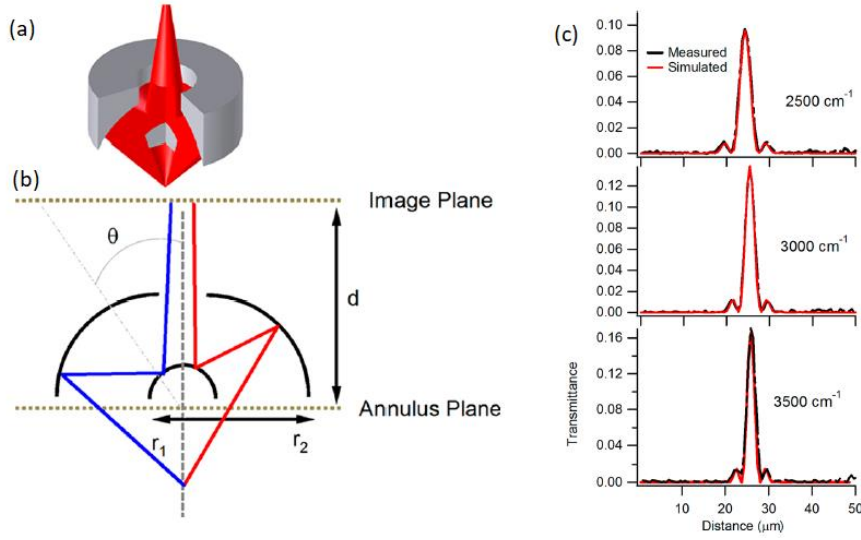
Figure 24 (a) Three-dimensional schematic of objective (top) and condenser (bottom) Schwarzschild optics used at IRENI. (b) Schematic diagram showing cross-section of a cylindrically symmetric Schwarzschild optic. (c) PSFs for the 74× objective lens within the Hyperion 3000 IR microscope. Center profiles through measured PSFs at 3500, 3000, and 2500 cm−1 are overlaid with simulated curves resulting from the fitting results. (Mattson, Nasse, Rak, Gough, & Hirschmugl, 2012)

$$I_{meas}(\text{x}, \text{y}) = I_{true}(\text{x}, \text{y}) * PSF(x, y), \qquad (4.25)$$

where $I_{meas}(\text{x}, \text{y})$ is the measured image, and $I_{true}(\text{x}, \text{y})$ is the ideal image of the sample. By measuring the PSF for a given optical system, and convolving the ideal image with the PSF, the blurring effects of the system are considered. The wavelength dependent PSF of the Bruker Hyperion 3000 IR microscope for a 36x (0.5 NA) Schwarzschild objective was measured by a 2 µm pinhole, which approximates a point source object. The Schwarzschild objective is made of two concave/convex concentric parabolic mirrors, offset from one another as shown in Figure 24.

The wave propagation through a Schwarzschild objective can be crudely modeled by plane wave transmission through an annulus at the image plane and is described by the equation

$$I(\theta) = I_0 \left(\frac{2J_1(x)}{x} - \frac{2\varepsilon J_1(\varepsilon x)}{x} \right)^2, \qquad (4.26)$$

where J_1 is first order Bessel function, $x = kr_2 sin\theta$; k is $\frac{2\pi}{\lambda}$; r_2 is the radius of the primary mirror(Figure 24 (b)); θ is the angular position at the image plane with respect to the central axis

63

of Schwarzschild objective; r_1 is the radius of the secondary mirror, and $\varepsilon = \frac{r_2}{r_1}$ (Mattson, Nasse,

Rak, Gough, & Hirschmugl, 2012).

4.4 Results

4.4.1 Simulations

To model optical properties of cells and cell nuclei in the infrared region, poly (methyl methacrylate) (PMMA) microspheres are chosen for further studies. To understand the complexities involved with the scattering features of the spectra in the diffraction limit, where the ratio of wavelength and radius of the sample is $0.1 < \lambda/r < 10$, the hyperspectral image of a PMMA bead is simulated.

Figure 25 (a) shows the image simulation path: first electric field distribution is calculated for a sphere, then the intensity at a detector close to the sphere is convolved with the measured PSF to consider the blurring effects of the microscope. Figure 25 (b) shows the absorbance distribution calculated on the XY plane at z = 25.6 for a PMMA sphere with a radius of 25μm. Energy distribution is shown in the form of $-\log(|E|^2)$ for four different wavenumbers, 1148 cm^{-1}, 1732 cm^{-1}, 2508 cm^{-1} and 2952 cm^{-1}. 1148 cm^{-1} and 1732 cm^{-1} are a low frequency ($\lambda/r = 0.35$), and mid frequency ($\lambda/r = 0.23$) absorption band respectively. The energy is distributed uniformly at these two absorption bands. Figure 25 (b) shows that an electric field shape resonance happens at 2508 cm^{-1}($\lambda/r = 0.16$), where there is no absorption band. Inspecting visually the electric field at 2508 cm^{-1} in Figure 25 (b), enhancement of the electric field at the edges of the sphere, and its suppression at the center are observed. Figure 25 (b) shows the energy distribution at a weak absorption band-2952 cm^{-1} ($\lambda/r = 0.14$), although the shape resonances are present at low absorbance peaks, they are less dominant compare to the 2508 cm^{-1}. Hence, in addition to

64

scattering, presence of shape resonances can lead to variation in the spectra from one pixel to another.

Figure 25 (c) shows $-\log(|E|^2)$ for four different wavenumbers, namely 1148 cm^{-1}, 1732 cm^{-1}, 2508 cm^{-1} and 2952 cm^{-1} at the position of the virtual detector, z = 25.6 µm. Figure 14 (d) illustrates $-\log(|E|^2|)$ for four different wavenumbers, namely 1148 cm^{-1}, 1732 cm^{-1}, 2508 cm^{-1} and 2952 cm^{-1} at the position of the virtual detector.

Figure 25 (d) show the corresponding images after convolution with the PSF (Impulse response of the system). Comparing Figure 25 (c) and (d), the images shown in Figure 25 (d) are blurred compare to the images of Figure 25 (c). Figure 25 (e) shows the spectra extracted from the simulated hyperspectral cubes at the virtual detector, and after convolving with the PSF. It is shown that the near field features observed at the virtual detector are blurred after passing through the microscope. Figure 25 (d) also shows that the spectrum from the center of the sphere looks like the absorption spectrum of a PMMA thin film. However, by moving further away from the center, the spectra become distorted. This is due to light scattering, and enhancement of the electric fields at the edges of the sphere. For example, in Figure 25 (e) the spectrum corresponding to the pixel at (x = 0 µm, y = 20.9µm) does not have any of the PMMA absorption peaks.

The simulated images of a 25 µm radius PMMA bead show that homogeneity in the absorption images of a solid sphere is not expected in the measurements for all wavenumbers. The absorbance images look homogenous only in large absorption bands, such as 1732 cm^{-1} (when $\lambda/r = 0.35$). In addition, the spectra of a PMMA bead are space dependent, and the shape of the spectra changes by moving away from the center of the solid sphere.

65
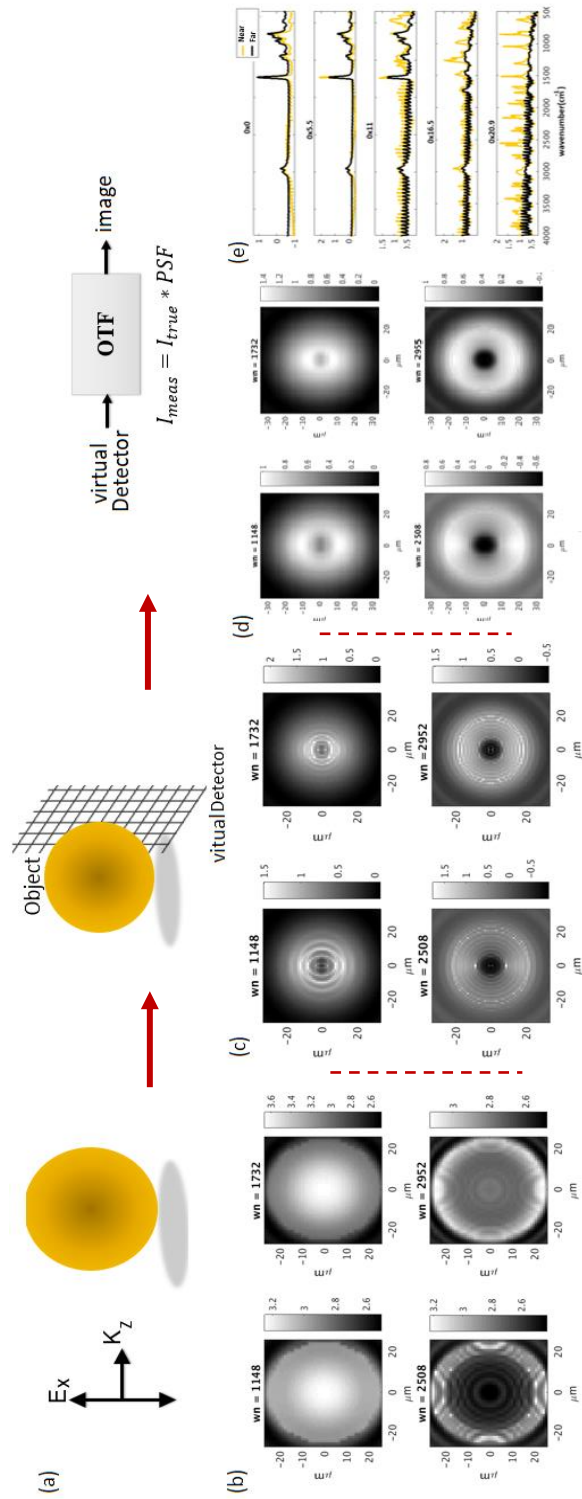
Figure 25 (a) A x polarized field is incident on the sphere, a virtual detector is placed close to the sphere, the true image at the virtual detector is convolved with PSF (b) $-log(|E|^2)$ at XY plane ($z = 25.6$)at 1148 cm^{-1}, at 1732 cm^{-1}, at 2508 cm^{-1} and 2952. (c) $-log(|E|^2)$ at the XY plane ($z = 25.6$) at 1148 cm^{-1}, at 1732 cm^{-1}, at 2508 cm^{-1} and 2952. (d) Electric field after passing through the microscope, $-log(|E|^2)$ at the XY plane ($z = 25.6$) at 1148 cm^{-1}, at 1732 cm^{-1}, at 2508 cm^{-1} and 2952. (e) Pixel spectra obtained from 0x0, 0x5.5, 0x11, 0x16.5 and 0x20.9 positions.

66
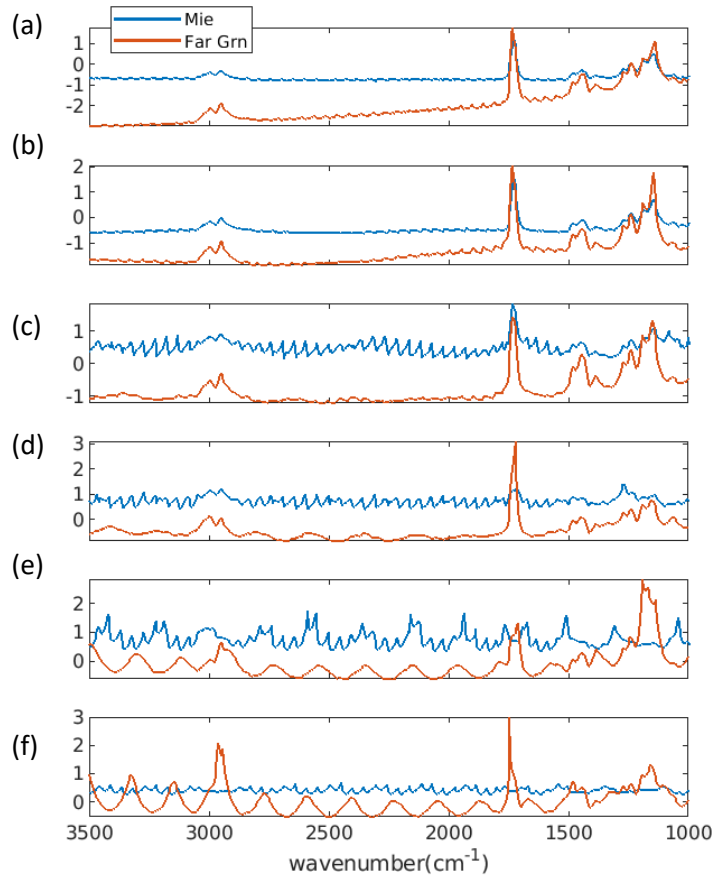
Figure 26 Farfield spectra Vs Nearfield spectra of a 25µm radius PMMA sphere at z = 25.6µm. (a) at center of the sphere. (b) radial distance of 5µm. (c) at radial distance of 10µm. (d) at radial distance of 15µm. (e) at radial distance of 20µm. (d) at radial distance of 25µm.

Figure 26 shows the near field and far filed spectra of the 25µm radius sphere at z location of

25.6µm for two simulations. The blue curve shows the result of the near field simulation, while

the red curve shows the spectra calculated by far field tensor Green's function. The spectra shown

in Figure 26 (a) to (f) show pixelated spectra of the sphere from center to the edge with radial

distance of 5µm. It is considered that intensity is equal to the square of the absolute value of normal

component of the electric field to the detector. The near field spectrum at the center of the sphere

has a negative baseline, and it is free of any ripple or wiggles.

A negative baseline in the absorbance spectrum might seem unusual at very first and one could

claim that the sphere is generating energy, and this disagrees with conservation of the energy. A

67
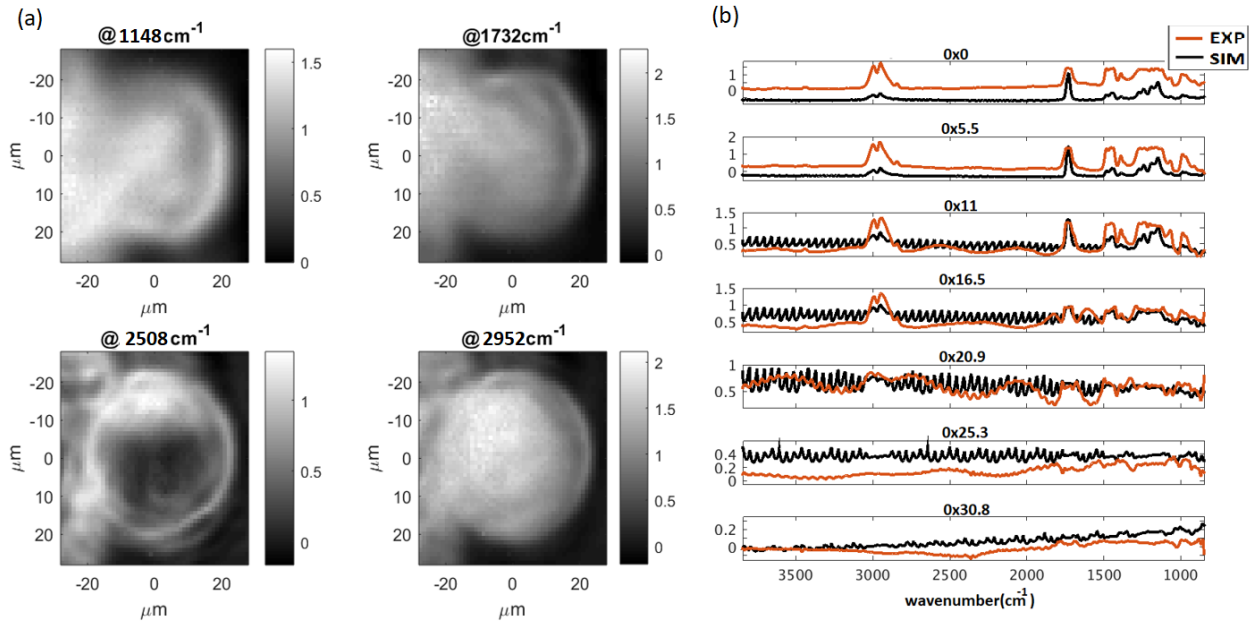
Figure 27 Measurement VS simulation, 25µm radius PMMA bead. (a) Projection Images measure at of 1148 cm⁻¹, 1732 cm⁻¹, 2508 cm⁻¹ and 2952 cm⁻¹. (b) Simulated spectra compare to measure spectra of the 25µm radius PMMA bead. The x-y location of each spectrum is written on the title of the image.

negative baseline is indicative of presence of shape resonances inside of the sphere, or it might simply happen because the scattering off the sphere will result in bending the light and focusing the light at a specific position. By integrating the energy over an area larger than the scattering area of the sphere, one could see that the law of conservation of the energy is valid. The ripples (fast varying signatures) appear at the spectra that are close to the edge of the sphere in the nearfield spectra. Apart from the ripples, wiggles are observed at Figure 26 (e).

The spectrum that is calculated by the far field Green's function at the center of the sphere shown in Figure 26 (a) has a linear slope that is decreasing with wavenumber, while this slope vanishes toward the edges of the sphere. The ripples are not preserved at the simulated far filed spectra, even at the pixels close to the edges. The absorbance bands at Figure 26 (e), and (f) are distorted, these spectra are at radial distances of 20µm, and 25µm respectively. There is no absorbance band in the near field spectra, although some spectral features are present in the far-field spectra.

The spectra shown in Figure 26 are calculated by considering that intensity is simply square of the absolute value of the electric field.

Figure 27 (a) shows the measured chemical images (hyperspectral images or a broadband image) of a 25µm PMMA sphere at 1148 cm^{-1}, 1732 cm^{-1}, 2508 cm^{-1} and 2952 cm^{-1}. The red spectra shown in Figure 27 (b) show the measured spectra. The black spectra show the corresponding near field simulated spectra, that are convolved with the PSF, and have the most similarity between the measurement and the simulations. Although the object is homogenous like the simulations, the measured images show some variation in the absorption image across the sphere. PMMA does not have any absorption band at 2508 cm^{-1}, but the measured image at 2508cm^{-1} looks hollow. This is the result of the presence of shape resonances at this wavenumber. There is an agreement between the simulated and measured spectra at the center of the sphere.

The absorption peaks both in simulation and experiment vanish at distances larger than 20µm away from the center of the sphere. However, the baseline of the simulated and measured spectra is different. It is shown that as we move from the center to the edges of the sphere there is more wiggles (slow oscillatory variation due to the interference of the incident and scattered wave) in the measured spectra compare to the simulations. Also, more ripple structure (high frequency oscillatory variations due to the electromagnetic resonances) (Blumel, Bagcioglu, Lukaccs, & Kohler, 2016) is observed in the simulation compare to the experiment. It is assumed that the incident light is fully coherent for the simulations, while the measurement is done by the synchrotron source at IRENI, that is considered as a partially coherent source. In addition, if the incident light was not normal to the sphere, different shape resonances might be excited compare to the situation that incident light is normal to the sphere (which is the case in the simulations).

69

With the insight gained from the simulations and the experiment, we concluded that the scattering features observed in the pixels are the results of two phenomena, (I) resonance of the light in the 3 dimensional geometry of the sample, and (II) bending of the light as the result of a sudden change in the value of the refractive index at the boundaries of the sample.

The conclusion is that for removing the scattering from pixelated data, an inverse scattering method is needed. An inverse method that maps a 2-dimnesional image to a 3-dimensional volume of the sample. In the next chapter an inverse method for removing scattering from pixelated broadband images is provided.

Chapter 5

5 Super Resolution 3D Refractive Index Recovery

The results of Chapters 3 and 4 show that in diffraction limit, scattering is a function of axial position of the image plane, geometrical shape of the sample and coherency of the light source. In addition, depending on the numerical aperture of the collecting optics (ability of the lens to collect scattered light), the spatially resolved scattering contribution in the spectra is changing.

In this chapter an algorithm for recovery of the true complex refractive index of the highly scatterer is presented. It is first demonstrated that the real part of the refractive index has the main role in the spectral scattering contributions. Then it is shown that the constant real part of the refractive index can be estimated by spectral information at regions far from the absorption bands. Then by rephrasing the Green's function of the Maxwell's equation as a state space equation, and by using the electric field images instead of intensity images, the true complex refractive index of a homogenous sphere (a standard material that is a gelatinous protein mixture) is recovered by an iterative algorithm.

Then it is shown that the algorithm can be extended for recovery of the refractive index of samples with inhomogeneities. The result show that by employing a suitable mesh grid for the Green's integration, the refractive index of the sample could be recovered with super resolution.

In order to evaluate the robustness of the algorithm for handling real data, the sensitivity of the algorithm to noise is tested. Then the algorithm is applied to broadband holographic images of a melanosome. The recovered refractive indexes are promising. However, due to the lack of

71

information about the axial position of the image plane the imaginary part of the refractive index of the melanosome are not recovered.

Consider that the algorithm uses the electric field of the sample at the image plane not the intensity. Phase microscopy is a method for measuring amplitude and phase of the electric field, and we propose that instead of conventional FTIR, for truly remove the scattering form the hyperspectral images, the broadband phase microscopy is necessary.

5.1 Introduction

Many samples in microscopy are largely transparent, thus absorbing little or no light. When light passes through such an object, the predominant effect is the generation of a spatially varying phase shift. This effect is not directly observable with a conventional microscope and a sensor that responds to light intensity (Goodman, Fourier Optics, 2005). Traditionally, dye labels and other contrast agents are used in conventional optical microscopy and fluorescence techniques; however, these usually degrade the sample and are limited to known molecular species. Vibrational spectroscopic imaging techniques, such as infrared hyperspectral imaging allow, for nonperturbing molecular study of micrometer-thick samples (Yeh, Kenkel, Liu, & Bhargava, 2015).

Fourier transform infrared (FT-IR) imaging technology along with advance methods of data analysis is one of the most powerful techniques for identification and localization of chemical compounds. This technique has numerous applications in life sciences such as chemistry, biology, agronomy, and medicine. Improving the resolution of conventional FT-IR microscopes is associated with two main parameters: (i) the numerical aperture of the imaging systems and (ii) the properties of the light source, such as total flux, directionality and coherency.

Hyperspectral infrared imaging is now used more often for single cell cycle study and disease pathology (Baker, et al., Using Fourier transform IR spectroscopy to analyze biological materials, 2014) (Fernandez, Bhargava, Hewitt, & Levin, 2005) (Heraud, et al., 2010) (Mattson, et al., 2013) (Holman H.-Y. N., Bechtel, Hao, & Martin, 2010) (Vaccari, Birarda, Businaro, Pacor, & Grenci, 2012) (Tobin, et al., 2010). Size of the non-homogeneities in tissues and biological cells is in the same order as the mid-IR wavelength, light behaves as a wave in interaction with tissue, as a result strong scattering features are observed in infrared microscopy spectra of tissues specifically single cells. There are complexities with scattering correction of microscopy spectra, for instance Schwarzschild objective partially block the scattered light by the obscuration of the small mirror. The scattered light that does not reach the detector leads to apparent absorption signature in the measured spectra. (Konevskikh T. , Lukacs, Blümel, Ponossov, & Kohler, 2015). Several Mie scattering correction methods for infrared spectroscopy of single cells have been published (Bassan, et al., Resonant Mie Scattering (RMieS) correction of infrared spectra from highly scattering biological samples, 2009) (KOHLER, et al., 2008) (Dijk, Mayerich, Carney, & Bhargava, 2013) (Konevskikh T. , Lukacs, Blümel, Ponossov, & Kohler, 2015) (Solheim, et al., 2019). These algorithms are based on fitting the measured data to a known reference spectrum, that is not spatially varying. Applying the same algorithms to hyperspectral images washes out the slight spatial changes in the microscopy spectra and blurs the corresponding chemical images.

Although Schwarzschild objective partially blocks the scattered light, it can be considered as a one to one mapping of the sample voxels to the image voxels. The scattering contribution observed at 2D pixels are the result of the interference pattern of the light scattered from all voxels within the sample, so for correcting the spectral scattering features and solving the inverse problem, 3D structure of the sample must be considered. Martin, et al. (Martin, et al., 2013)

73

initially reported spectro-microtomography (a mapping of 2D intensity images to 3D intensity inside the sample) by means of filtered back-projection algorithm and full FPA field of view IR images taken as a function of sample orientation for full tomographic reconstruction. However, filtered back-projection does not consider diffraction. This result in an enhanced reconstruction of the refractive index. Diffraction tomography is an algorithm that incorporates wave nature of the light. Diffraction tomography recovers the 3D refractive index of the sample by mapping 2D measured images consist of amplitude and phase of the electric field to 3D map of the refractive index of the sample (Muller, Schurmann, & Guck, 2016).

Employing infrared lasers in infrared imaging (Yeh, Kenkel, Liu, & Bhargava, 2015) , and advent of the infrared refractive optics made of Zinc Selenide (ZnSe) pave the way for the next generation of IR microscope that deploy the coherent imaging methods such as diffraction tomography. Tomographic phase microscopy is based on phase-shifting laser interferometric microscopy (Choi, et al., 2007). A tomographic phase microscope is generally consisting of two parts, (i) a microscope based on a Mach-Zehnder heterodyne interferometer, that provides quantitative phase images and (ii) a device that controls the angle of coherent illumination impinging the sample. Point spread function (PSF) of a tomographic phase microscope depends on the method chosen for controlling the angle of illumination. The hybrid method of data collection explained by Park, et all (PARK, SHIN, & PARK, 2018) result in minimum loss of information in the measured phase images.

The main purpose in infrared chemical imaging is to recover the spatially varying map of the imaginary part of the refractive index at sample position. This map is used for determination of the chemistry at every pixel, and ultimately at every voxel within the sample. Current diffraction tomography algorithm cannot accurately recover the imaginary part of the refractive index. Here

74
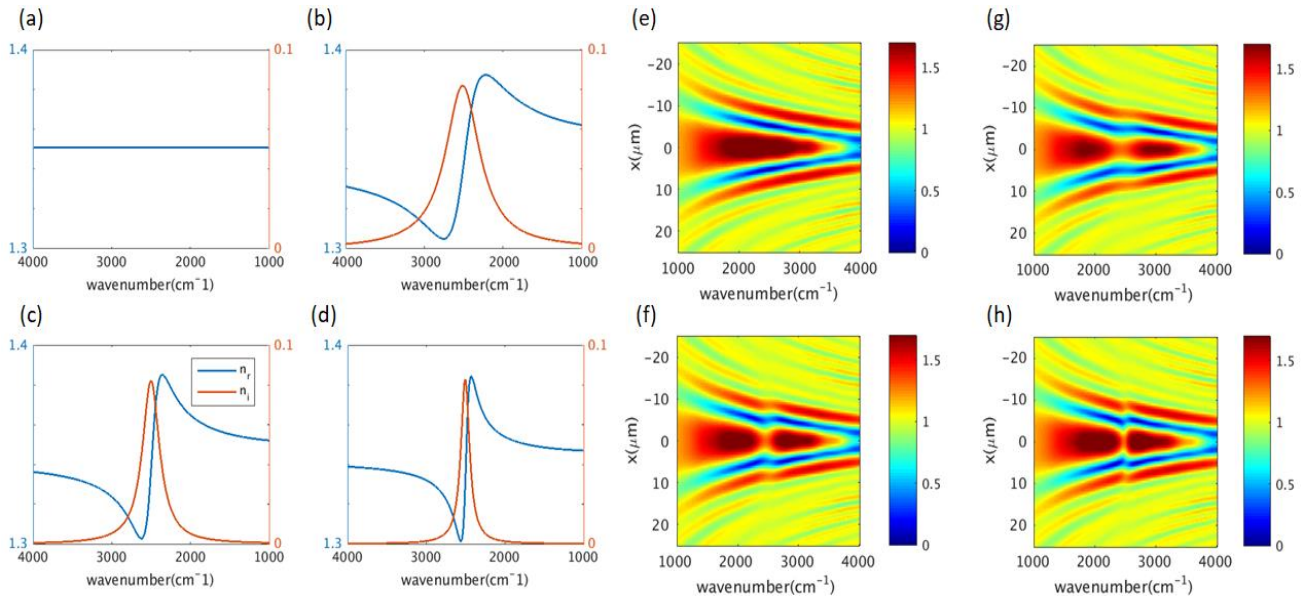
Figure 28 Visualization of the scattering off a sphere of radius 3 μm as a function of the wavenumber, observed in a plane orthogonal to the optical axis, located at a distance of 20μm from the center of the sphere. The vertical displacement from the optical axis is denoted by x. Four cases are shown(a) and (c) Material 1: constant real refractive index of 1.35. (b) and (g) Material 2: Absorption peak at 2500cm^{-1} with FWHM of 300 cm^{-1} (c) Material 3: Absorption peak at 2500cm^{-1} with FWHM of 175 cm^{-1} (d) and (h) Material 4: Absorption peak at 2500cm^{-1} with FWHM of 87.5 cm^{-1}.

a new algorithm based on solving a system of linear equations for solving the inverse scattering problem for a homogenous sample is presented. It is demonstrated that this algorithm has super resolution capabilities.

5.2 Methods

Electric permittivity is a property of a material that measures the resistance of the material in forming an electric field inside it. This quantity, that is described by Lorentz oscillator model provides the underlying rational for the presence of frequency-dependent absorption and scattering. Electric permittivity ε is a complex variable, showing the magnitude and phase of the displacement of the oscillator (nucleus and electron binding forces behave like a spring). The real and imaginary part of the ε are related to resonance angular frequency of the oscillator ω_0, and plasma frequency of the material ω_p by

75

$$\varepsilon_r(\omega) = 1 + \frac{\omega_p^2(\omega_0^2 - \omega^2)}{(\omega_0^2 - \omega^2)^2 + \omega^2\gamma^2}, \tag{5.1}$$

and

$$\varepsilon_i(\omega) = \frac{\omega_p^2\gamma\omega}{(\omega_0^2 - \omega^2)^2 + \omega^2\gamma^2}. \tag{5.2}$$

Where γ is a constant. The complex refractive index is related to the electric permittivity by

$$n(\omega) = \sqrt{\varepsilon}. \tag{5.3 (a)}$$

$$\varepsilon = \varepsilon_r(\omega) + i\varepsilon_i(\omega) + 0.8 \tag{5.3 (b)}$$

Where n is the complex refractive index and ε is the complex electric permittivity. The constant value of 0.8 is added to the ε, so that the constant real part of the refractive index becomes ~1.33, which is the value for most of the biological samples. Lorentz oscillator model provides the underlying rational for the presence of frequency-dependent absorption and scattering (Almog, Bradley, & Bulovi´c).

In order to visualize broadband scattering and absorption by microspheres, broadband chemical images of 4 spheres are simulated with the method of Chapter 4. The radius of all the microspheres is $3\mu m$ under irradiation of a horizontally polarized plane wave, each microsphere has a complex refractive index as shown in Figure 28 (a) to (d). The results are shown in Figure 28 (e) to (h).

Figure 28 (a) to (d) show the real and imaginary part of the refractive index of the 4 simulated spheres. Figure 28 (a) shows a material with a constant refractive index in Mid-IR range of the spectrum. The materials shown in Figure 28 (b) to (d) have an absorption peak at 2500 cm^{-1}. The materials are defined by the Lorentzian function described by Eq. (5.3). The Lorentzian function

76

describing these materials are manipulated so that the full width half maximum of the peaks divides by 2 from Figure 28 (b) to (c). Figure 28 (e) to (h) shows the horizontal line profile of the absorbance through the center of the images of the spheres made of the materials with refractive indices shown in Figure 28 (a) to (d). The image plane is located $20\mu m$ away from the center of the sphere. Relating scattering to the real part of the refractive index and absorption to the imaginary part, Figure 28 (e) shows the wavelength dependent scattering as a function of wavenumber for a non-absorbing material. Figure 28 (g) shows the case for a material with a wide absorption band. The broadband intensity profile shown at Figure 28 (g) has a local minimum at 2500 cm^{-1}, but the overall shape of the scattering in Figure 28 (e) and (g) are similar. This shows that the dispersion resulted from the absorption peak does not affect the overall scattering. As the absorption peak becomes sharper and sharper - Figure 28 (g) to (h) - the dispersion effect demonstrates itself as a jump in the scattering distribution of the sample, but the general distribution of the scattering is preserved. This result illustrates that scattering is mostly dependent on the constant real part of the refractive index. This leads us toward identifying an optimization algorithm for finding the imaginary part of the refractive index, using the forward scattered light and the real part of the refractive index.

5.2.1 Recovering absorptivity by inverse scattering

In the absence of scattering, absorbance is related to the imaginary part of the refractive index by

$$n_i = \frac{A\, ln(10)}{4\pi l v}. \qquad (5.4)$$

where n_i is the imaginary part of the refractive index, A is the absorbance, and l is the effective thickness of the absorbing material. Scattering can dominate infrared spectra of samples with the

77
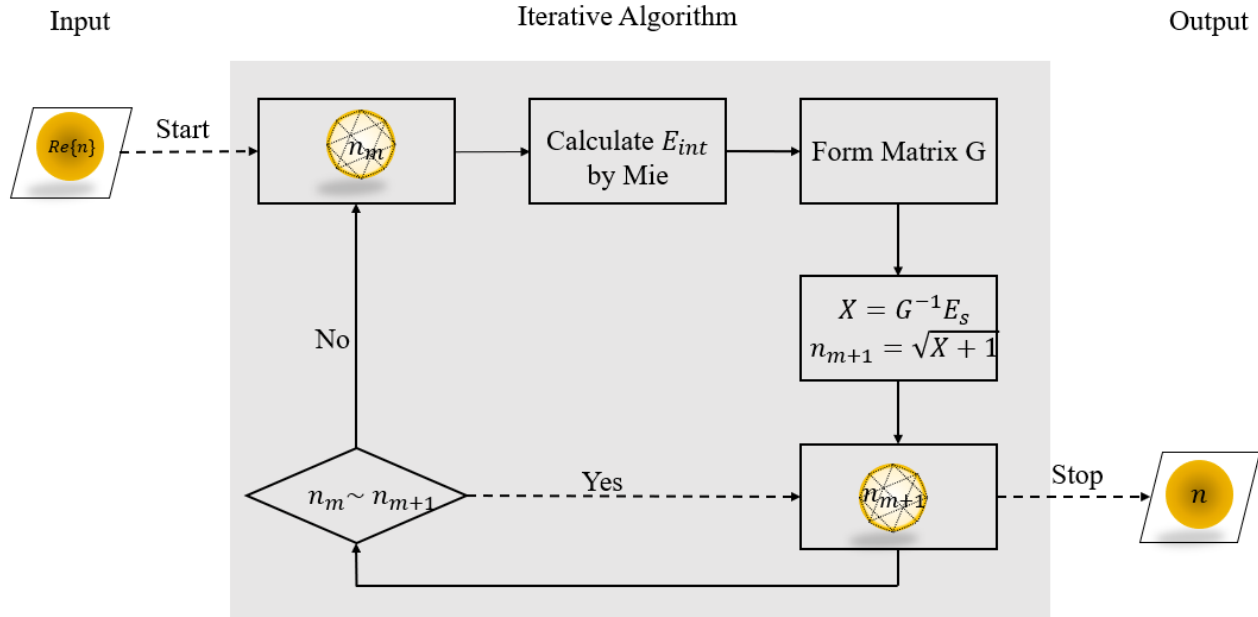
Figure 29 Flowchart of the inverse scattering method for recovering n_i

sizes in the order of infrared wavelength (3 to 10 µm), and as a result Eq. (5.4) does not hold anymore.

Recovering n_i from measurements and removing the scattering features helps with chemometric analysis and makes us one step closer to quantitative infrared spectroscopy. We show below that recovering the exact value of n_i at the presence of scattering is possible, if the amplitude and phase of the electric field at the FPA and an approximation of the real part of the refractive index n_r are known. The presented algorithm for n_i recovery is demonstrated in Figure 29.

In order to reduce the number of iterations of the algorithm, a 3D mask of the sample is obtained through a structural imaging technique, for example visible microscopy. In wide field FTIR infrared micro-spectroscopy, the beam width covers the whole field of view at the focal plane, so it is assumed that the sample is irradiated by a plane broadband infrared source. For recovering the value of n_i in frequency range of 1000 cm^{-1} to 4000 cm^{-1} the measured phase images are fitted to the simulated phase images by an iterative optimization algorithm. In order to simulate

78

the phase image, the electric and magnetic field of the sample is approximated by a numerical method such as Green's function (according to Chapter 4), Finite-Difference Time Domain (FDTD) or Finite Element Method (FEM) at the image plane.

Discretized Green's integral considers the effect of each voxel of the sample separately in the image formation. By reformulating the Green's integral in a matrix format, as explained in Section 5.2.2, the state Matrix G (free space Green's function limited to the constraint of the sample) and state variables $\vec{X}$ (complex electric susceptibility) are defined, and a linear system of equations is formed. Solving the linear system of the equations for $\vec{X}$, and comparing the results with the initial refractive index we can recover the spatially resolved complex refractive index in an iterative algorithm, which is summarized as follows:

Algorithm

Input: $n_0(\vec{r}')$, $o(\vec{r}')$, N
$n_0(\vec{r}')$ - initial guess for the refractive index
$o(\vec{r}')$ - object function
$\vec{r}'$ - vector position inside of the sample
N – number of voxel discretization of the sample

Output: $n(\vec{r}')$
$n(\vec{r}')$ - complex refractive index

Initialization. Choose $n_m(\vec{r}') = n_0(\vec{r}')$ for $m = 0$, discretize the sample to N voxels
General Step ($m = 0, 1, 2, ...$):
 1) Simulating the internal field for the object $o(\vec{r}')$ with $n_i(\vec{r}')$
 2) Integration and forming matrix G
 3) Solving the equation $G\vec{X} = \vec{E}_s$ by SVD
 4) Calculating n_{m+1}
 5) Go to 1
Until $|n_{m+1} - n_m| \leq \varepsilon$

79

5.2.2 Green's integral as a state-space equation

As it is explained in Chapter 4, the Green's function method allows us to compute the electric and magnetic fields explained by Maxwell equations. Defining $o(\vec{r}')$ as the object function or 3D geometrical shape of a homogenous sample, the field observed at the position $\vec{r}$ E_{FPA}, is calculated according to

$$\vec{E}_{FPA}(\vec{r}) = \vec{E}_{inc}(\vec{r}) + k^2 \int (n(\vec{r}')^2 - 1)\bar{\bar{G}}(\vec{r} - \vec{r}')\vec{E}_{int}(\vec{r}')o(\vec{r}')d^3\vec{r}', \qquad (5.5)$$

Where $\vec{r} = (x, y, z)$ is the coordinate of the image plane, and the sample coordinate is $\vec{r}' = (x', y', z')$, and $n(\vec{r}) = n_r(\vec{r}) + jn_i(\vec{r})$ is the complex refractive index at the position $\vec{r}$. $E_{int}(\vec{r}')$ is the internal field of the sample $o(\vec{r}')$, $k = \frac{2\pi}{\lambda}$ and $\bar{\bar{G}}(\vec{r} - \vec{r}')$ is the tensor free space Green's function of the Maxwell's equation. Since, the image plane is located at the far field, only the far field terms of the Green's function are considered in the calculations. The tensor Green's function is defined in subsection 4.3.2.1. Defining $X(\vec{r}') = n(\vec{r}')^2 - 1$, we have

$$\vec{E}_{FPA}(\vec{r}) - \vec{E}_{inc}(\vec{r}) = k^2 \int X(\vec{r}')\bar{\bar{G}}(\vec{r} - \vec{r}')\vec{E}_{int}(\vec{r}')o(\vec{r}')d^3\vec{r}'. \qquad (5.6)$$

For the pixel $\vec{r}_j$ at the image plane, Eq. (5.5) in discretized format is

$$\vec{E}_{FPA}(\vec{r}_j) - \vec{E}_{inc}(\vec{r}_j) = k^2 \sum_{\vec{r}_l'} X_l \bar{\bar{G}}(\vec{r}_j, \vec{r}_l')\vec{E}_{int}(\vec{r}_l')o(\vec{r}_l')\Delta V, \qquad (5.7)$$

where $j = 1, 2, \ldots M$, shows the index of the pixels at the image plane and $l = 1, 2, \ldots N$, the indexes of the sample voxels, and $\Delta V = dxdydz$. Defining the scattering vector as

$$\vec{E}_s = \vec{E}_{FPA}(\vec{r}_j) - \vec{E}_{inc}(\vec{r}_j) = \begin{pmatrix} e_{x_j} \\ e_{y_j} \\ e_{z_j} \end{pmatrix}, \qquad (5.8)$$

where e_{x_j}, e_{y_j}, e_{z_j} are the three components of the scattered field, and considering

80

$$k^2 \bar{\bar{G}}(\vec{r}_j, \vec{r}_l')\vec{E}_{int}(\vec{r}_l')\Delta V = \begin{pmatrix} g_{x_{jl}} \\ g_{y_{jl}} \\ g_{z_{jl}} \end{pmatrix}, \qquad (5.9)$$

For each pixel at the image plane we have

$$\sum_{l=1}^{N_{voxels}} g_{x_{jl}} X_l = e_{x_j}, \qquad (5.10)$$

$$\sum_{l=1}^{N_{voxels}} g_{y_{jl}} X_l = e_{y_j}, \qquad (5.11)$$

$$\sum_{l=1}^{N_{voxels}} g_{z_{jl}} X_l = e_{z_j}, \qquad (5.12)$$

or,

$$G_x \vec{X} = \vec{E}_{sx}, \qquad (5.13)$$

$$G_y \vec{X} = \vec{E}_{sy}, \qquad (5.14)$$

$$G_z \vec{X} = \vec{E}_{sz}, \qquad (5.15)$$

Merging equations of (5.13) to (5.15),

$$G\vec{X} = \vec{E}_s, \qquad (5.16)$$

where G is a $3M \times N$ matrix, and $\vec{X}$ and $\vec{E}_s$ are vectors with dimensions of $N \times 1$ and $3M \times 1$, respectively. If $3M > N$, then the system of linear equations is overdetermined, by solving the equation for $\vec{X}$ we can calculate $n(\vec{r}')$.

5.2.3 Real part of the refractive index n_r

By measuring the average infrared spectrum of the sample and removing scattering features by EMSC method, we can obtain a global standard spectrum. This is adequate to determine a

81

frequency dependent complex refractive index by means of Eq. (5.4). and the Kramers-Kronig relation. The real part of the refractive index n_r is

$$n_r(v) = n_{con} + \frac{2}{\pi} \boldsymbol{P} \int_0^{\infty} \frac{s n_i(s)}{s^2 - v^2} ds, \qquad (5.17)$$

where v is the wavenumber, n_{con} is the real constant part of the refractive index, and $\boldsymbol{P}$ denotes the Cauchy principal value of the integral. This value of $n_r(v)$ is used as an initial guess for the refractive index. As we show below the starting values for $n_r(v)$ only needs to be within a factor of 2 of the experimental values for $n_r(v)$ to be able to start the iterative method and converge to acceptable values across the entire spectrum.

5.2.4 Calculation of the internal and scattered fields

For an arbitrary sample, the internal field and scattered field of the sample can be simulated by one of the numerical methods such as FDTD or FEM. The focus of the current paper is on a rotationally symmetric objects, such as sphere which their forward projections are invariable along angular direction. Absorption and scattering of spheres are described by the method explained in Chapter 4. Convergence of the Green's integral Eq. (5.5) is investigated for a homogenous sphere with radius of 3µm. The internal field of the sphere is simulated in spherical coordinate with discretization of $N_r \times N_\phi \times N_\theta = 257 \times 36 \times 36 = 333072$ nodes, where N_r is the discretization along radial distance, N_ϕ discretization along the azimuth angle, and N_θ is the discretization along the polar angle.

The scattered field $\vec{E}_s$ is calculated at a 20×20 µm² window located $20 \mu m$ away from the sample. The energy evaluation of the field at image plane shows that the window is large enough that we could consider most of the light is captured, and the window is a good approximation of a

82

4π detector (supplementary materials B). The scattered field is calculated by Eq. (5.5), by inserting the calculated internal field in Eq. (5.5).

5.2.5 Solving the system of linear equations by singular value decomposition (SVD)

Singular value decomposition is used for solving Eq. (5.16). Singular value decomposition of any $m \times n$ matrix such as G with $m \geq n$ is the product of three matrices $G = USV^T$ where the columns of U and V are orthonormal, and the matrix S is a diagonal with positive real entries. Diagonal elements of S are called singular values of matrix G, and the columns of matrix U are called right singular values of Matrix G and columns of matrix V are called left singular values of G. The Moore-Penrose Pseudoinverse of matrix G is

$$G^{-1} = VS^{-1}U^*. \quad (5.18)$$

then, Eq. (5.13) is solved as

$$\vec{X}(r) = G^{-1}E_s \quad , \quad (5.19)$$

$$\vec{n}(r) = \sqrt{\vec{X}(r) + 1}. \quad (5.20)$$

5.2.6 Noise Analysis

In order to evaluate the ability of the algorithm in handling real data, noise analysis are done. Digital measured images are degraded by several types of noise, such as, salt and pepper noise, Gaussian noise, Poisson noise (Photon-noise), and speckle noise. [1][2].

Poisson noise is a basic form of uncertainty associated with the measurement of light. It originates from discrete nature of light, and photon counting. Image sensor measure the irradiance

83

by counting the number of photons that reached the detector in a given time interval. The photons captured by the detector turn into electron charges by the photoelectric effect. The random individual arrival of the photons leads to noise. Photon arrival can be treated as independent events that follow random temporal distribution. As a result, photon counting is a classic Poisson process, and the number of photons N measured by a given sensor element over time interval *t* is described by the discrete Poisson probability distribution [3]

$$\Pr(N = k) = \frac{e^{-\lambda t}(\lambda t)^k}{k!} \quad (5.21)$$

Where λ is the expected number of photons per unit time interval, which is proportional to the incident irradiance. This is a standard Poisson distribution with a rate parameter λt that corresponds to the expected incident photon count. The uncertainty described by this distribution is known as photon noise [3].

In order to investigate the ability of the algorithm to handle noise, Poisson noise is added to the simulated images. Real and imaginary part of the electric field are first normalized between 0, and 1. The result is then scaled by $\frac{N_{photon}}{10^{12}}$, where N_{photon} is the number of photon counts. Next, Poisson noise is added to the real part and imaginary part of the refractive index separately by using the imnoise MATLAB command. Then the electric filed image is scaled back to its original value. Noise analysis are done for the case where $N_{photon} = \infty$ (no noise), and for three other cases where $N_{photon} = 125, 250, 500$. A 75 nm radius sphere with complex refractive index of 1.45+0.1i is chosen for the noise analysis. The radiated light has a wavelength of 532 nm, and the size of the image window is $1060 \times 1060 \text{ nm}^2$, and the image is placed 20μm away from the center of the sphere.

84
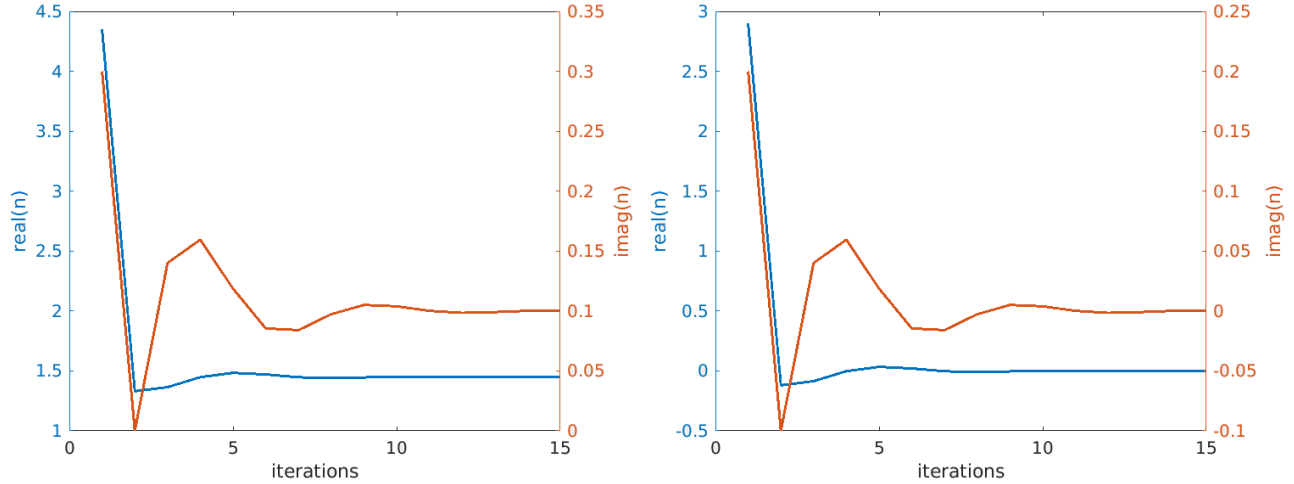
Figure 30 (a) Convergent with initial value of 4.35+0.3i, (b) error of the algorithm with initial value of = 4.35+0.3i.

5.3 Results

The algorithm is evaluated by recovering the complex refractive index of a homogenous sphere. Convergence of the method is dependent on the value of the refractive index, wavenumber, radius of the sphere, gap between the sample and screen, size of the screen and its pixels. To mimic the realistic experiment, where we are limited to far field geometry, the screen is placed far enough from the sample that the nearfield components do not contribute significantly to the result (Bansal, 1999).

The algorithm is used to recover the refractive index of a homogenous sphere with radius of 1.5 µm and refractive index of $n = n_r + n_i i = 1.45 + 0.1i$ at 2500 cm^{-1}. The simulated image plane is a $20 \times 20 \ \mu m^2$ window placed 20 µm away from the centre of the sphere, far enough from the sample that near field effects are reduced in strength to be within the measurement noise, size of the pixels at the image plane are $\frac{\lambda}{10} \times \frac{\lambda}{10} \ \mu m^2$. The radius of the convergence of the algorithm is larger than $3n$. For $n_0 = 3n$ the algorithm converges after 15 iterations (~220 mins - Mortimer)

85
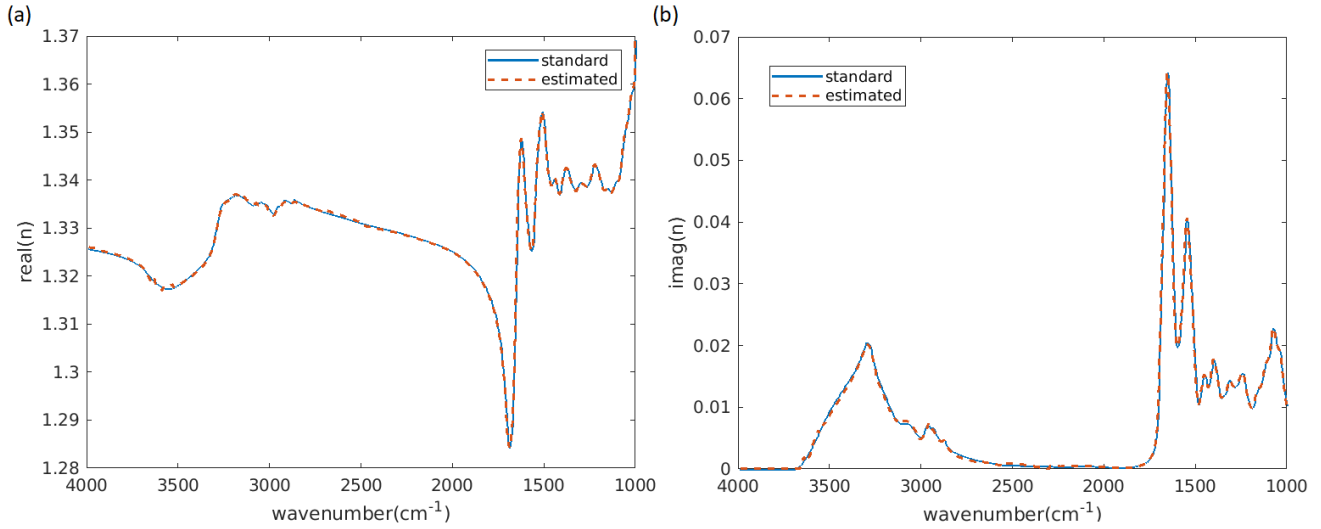
Figure 31 (a) Real part of the refractive index of Matrigel. Blue curve shows the standard spectrum and red shows the estimated version by the algorithm. (b) Imaginary part of the refractive index of the matrigel, standard versus estimated by the algorithm.

with 3 digits of precision. If n_r is known, then the algorithm converges after 13 iterations (191 mins - Mortimer) with 3 digits of precision, with increasing the number of iterations, we reached accuracy of the machine precision. Figure 30 (a) shows the convergent of the real and imaginary part of the refractive index with initial guess of $n_0 = 4.53 + 01i$, and Figure 30 (b) shows the corresponding error. The algorithm converges with 3 digits of precision after 15 iterations. The algorithm is convergent for larger distance between the sample and the detector, we have test this by increasing the gap between the sample and detector as much as 5mm (larger than the distance between the sample and the objective). The algorithm is also convergent for smaller size spheres. We have tested the convergence for spheres radius of as small as 50 nm at 2500 cm^{-1}. The extend of the image plane must be increased for spheres with diameter of larger than 4 μm.

The spectral validation is done by testing the algorithm for a 3μm radius sphere made of Matrigel (a gelatinous protein mixture). Figure 31 shows the complex refractive index of matrigel (blue curve), and the recovered complex refractive index by the presented method. The fingerprint region of the spectrum is recovered with precision of 10^{-3}. Refractive index of the material is a

86

www.manaraa.com

continues function of the wavenumber, so the initial guess for $n_0(\vec{r}')$ is obtained by the nearest calculated wavenumber. At each time 16 spectral calculations were running in parallel on Mortimer, the high-performance computing system at UWM.

Figure 32 shows the simulated images of a 75 nm radius sphere with complex refractive index of 1.45+0.1i as the noise increases. Independent of the number of the photons that reach the detector the algorithm converges after 3 iteration with precision of 10^{-3} for the initial value of 1.33. The convergence is independent of the pixel sizes. The algorithm converges for nodes (pixels) that are $\lambda/10$ away from each other. Table 6 shows the ability of the algorithm to recover large imaginary part of the refractive index at presence of noise. The algorithm can recover imaginary part of the refractive index as large as 3. For the convergence analysis of the table. 6, the radius of the sphere is 0.6µm, the wavelength of the incident light is 4µm, the window of the image plane is $8.5 \times 8.5\ \mu m^2$ and the initial guess is $n_0 = 1.33$.

Table 6 Convergence of the algorithm for materials with large imaginary part of refractive index

n_{sphere}	#photons/pixel	Iterations	Converge to
1.45+0.1i	125	3	1.4488+0.1023i
1.45+1i	125	7	1.4465+1.0018i
1.45+2i	125	18	1.4515+1.9915i
1.45+3i	125	85	1.4546+3.0206i
1.45+4i	not convergent		

87
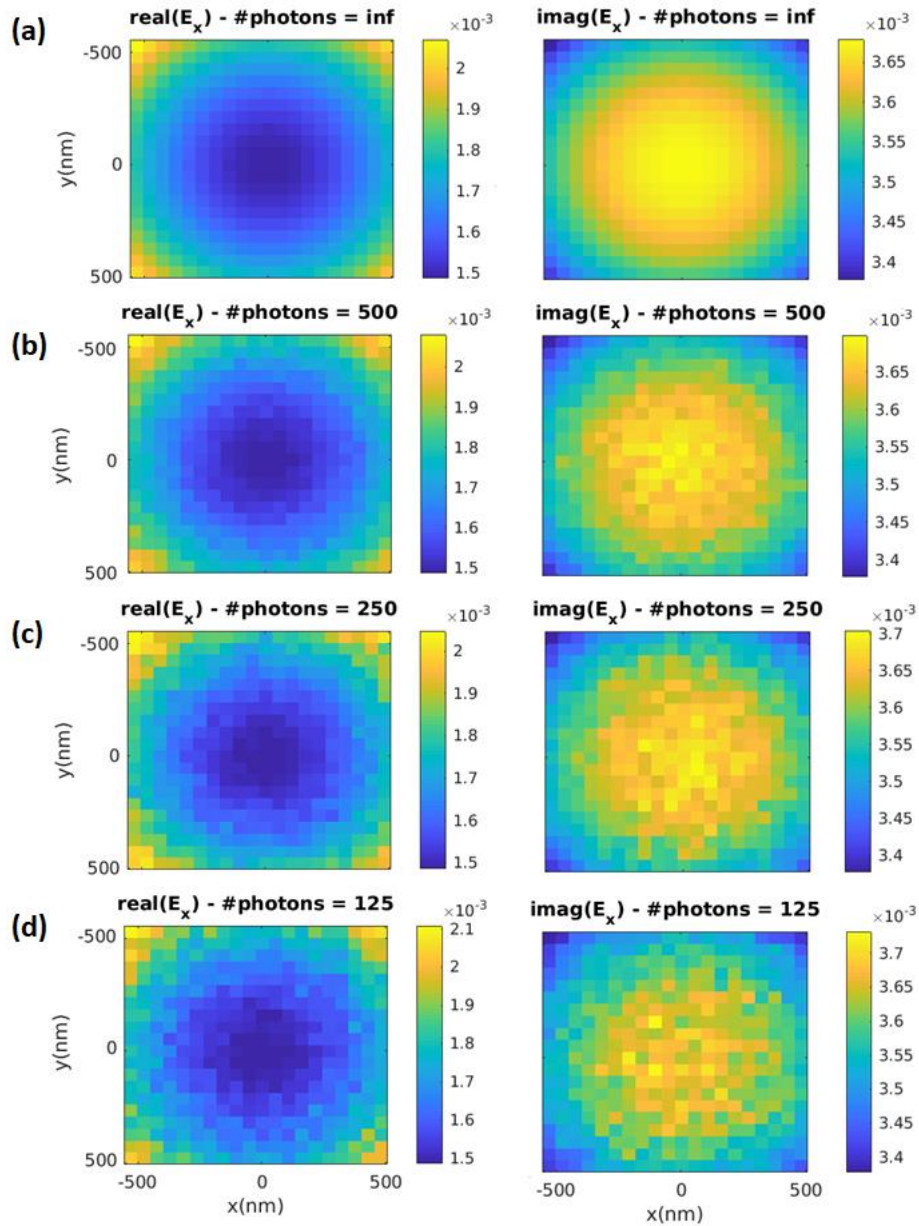
Figure 32 Poisson noise in the field images. The simulated images are for a 75 nm radius sphere with complex refractive index of 1.45+0.1i. The wavelength of the irradiated light is 532 nm, and the window size is 1060x1060 nm^2. The images are simulated 20 um away from the sample. (a) Original simulated field image with no noise. (b) The field image with $N_{photon} = 500$. (c) The field image with $N_{photon} = 250$. (d) The field image with $N_{photon} = 125$.

5.4   Discussion

Advent of broadband infrared laser sources, and optical materials such as ZnS leads to development of new infrared microscopy techniques enabling scientists to measure the complex electric field in infrared. For example, an infrared tomographic phase microscope (Choi, et al., 2007) can be designed to measure phase and amplitude of the transmitted light. Here we presented a new reconstruction algorithm for 3-dimensional (3D) recovery of the complex refractive index of the sample. The result show that our algorithm has super resolution capability. We have shown that our method removes the undesired scattering spectral features present in the infrared hyperspectral images. The heart of the algorithm is a Green's Integral that is rephrased as a state space equation. The optics are considered as a linear space-invariant system, where the sample is the input of the system and image is the output.

3D infrared spectral imaging was reported by Martin et al. (Martin, et al., 2013) for the first time. Although Martin, et al. could successfully resolve spectral features at specific positions of the sample, hollow regions were present in their reconstructed images. In diffraction limit where the size of the sample is in the same order as the incident light, light behaves as a wave, and it does not travel in straight line through the sample. This explicit wave nature of the light results in enhanced reconstruction of the refractive index at some positions (Muller, Schurmann, & Guck, 2016). Diffraction tomography algorithms based on Born and Rytov approximations are currently being used for 3D diffraction tomography. Fundamental to diffraction tomography is the Fourier diffraction theorem, that relates the Fourier transform of the measured forward scattered data with the Fourier transform of the object. The theory is valid when the inhomogeneities in the object are only weakly scattering (Kak & Slaney, 1988). In addition, the imaginary part of the refractive index cannot be recovered accurately with the diffraction tomography algorithm.

89

3D spatial resolution of an optical diffraction tomography (ODT) setup depends on the point spread function (PSF) of its microscope as well as its reconstruction algorithm. Fourier diffraction theory assumes that the scattered light is passed through a thin slice of the sample, and as the result the axial resolution of the algorithm depends on the depth of field, and scanning capabilities of the microscope (PARK, SHIN, & PARK, 2018), (Krauze, Kus´, S´ladowski, Skrzypek, & Kujawin´ ska, 2018). In the presented algorithm, it is considered that measured electric field at each pixel of the detector is the result of the interference pattern of all the voxels of the sample. This result in higher lateral and specifically axial resolution.

In a real experiment, the measured complex electric field $\overrightarrow{E_s}$ is the result of the convolution of the PSF with $\vec{E_s}$, in other words $\overrightarrow{E_s} = \vec{E_s} * PSF$, and depending on the numerical aperture of the microscope objective, the scattered light is partially missing, by rotating the sample and also the direction of the incident light, the missing cone spatial frequency information is being imaged. 3D point spread function of the microscope could be measured to recover the exact value of $\vec{E_s}$ (PARK, SHIN, & PARK, 2018).

For biological sample, dispersion effect is negligible independent of the full width half maximum of the absorption band, and the scattered signal could be related to only the real part of the refractive index (Figure 28), so initiating the algorithm with only the real part of the refractive index helps in finding the local solution of the problem.

Figure 29 summarizes the algorithm for the case where the geometrical shape and the real part of the refractive index are known. However, the algorithm could be applied to a sample with unknown shape. knowing the geometrical shape and the real part of the refractive index helps the algorithm to converge faster. Figure 30 shows that the algorithm is convergent for 3n radius of

90

convergent. In most cases, the average infrared spectrum of the sample is known, so there is a very low chance that the initial guess ends up out of the radius of convergence. Figure 31 shows the ability of the method to remove the scattering features present in the spectral data and recover the complex refractive index with a high accuracy. The algorithm converges to the complex value of the refractive index after 15 iterations with 10^{-3} accuracy, by increasing the number of iterations, the algorithm converges to the value of the refractive index with machine precision.

In the result section it is shown that the algorithm is convergent for a sphere with radius of 1.5 μm, at 2500 cm^{-1}, which is less than the diffraction limit ~ 4 μm. This shows that the algorithm has the potential to reconstruct super resolution 3D images taken by a conventional diffraction-limited tomographic phase microscope.

The extent of the screen is chosen depending on the physical properties of the problem. Properties such as the distance between the sample and screen, the refractive index of the sample and size of the sample. For the homogenous sphere studied in Figure 30 the algorithm is convergent disregard to the extend and pixelization of the screen. This is because the sphere is homogenous and the number of equations is more than the number of unknowns.

It is shown that the algorithm can be applied to non-homogenous spheres as well and the results are provided in Section 5.5.1. The algorithm is also being applied to experimental holographic images measured by a visible diffraction tomography microscope, and the preliminary results are provided in Section 5.5.2.

The reconstruction algorithm presented here is an optimization problem, that is trying to minimize the error between the measured complex electric field and its simulated value. However, intensity is the only quantity, that is measured by conventional infrared microscopes. In section

91

5.5.3 the algorithm is adjusted so that it is applicable to the infrared hyperspectral cubes which are measured by the conventional infrared microscopes.

5.5 Appendix

5.5.1 Extending the algorithm for a non-homogenous sphere

For a non-homogenous sample, the sphere is discretized to voxels. Depending on the number of the voxels and their shape, matrix G in Eq. (5.16) changes. Convergence of the algorithm, and finding a solution for Eq. (5.19) relies on stability of the matrix G.

The stability analysis of matrix G is done by calculating its condition number. Consider computing matrix-vector product $\vec{E}_s = G\vec{X}$, where $G \in \mathbb{R}^{n \times n}$:

Let $\vec{X} = \vec{s_1}$. Suppose we can compute $\widetilde{\vec{E}_s} = G\tilde{\vec{X}}$ with $\tilde{\vec{X}} = \vec{s_1} + \epsilon \vec{s_n}$. $\vec{s_1}$ is the right singular vector corresponding to the smallest singular value, say $\sigma_1 = 1$.

Then $G \tilde{\vec{X}} = \sigma_1 \vec{s_1} + \sigma_n \epsilon \vec{s_n}$. If $\sigma_n \gg 1/\epsilon$, then $\left\| G\tilde{\vec{X}} - G\vec{X} \right\|$ will be quite large. This is the same as having large $\mathcal{K} = \frac{\sigma_1}{\sigma_n}$, where $\mathcal{K}$ is the condition number of matrix G.

A 3-layer sphere is used for stability analysis of the algorithm. The sphere has a radius of 3 μm, and each layer of the sphere is 1μm thick. The core, the central layer and the shell have the refractive indices of 1.5, 1.4, and 1.3 respectively, and the surrounding material has a refractive index of 1.33. The internal field of the sphere is calculated for 257×36×36 nodes inside of the sphere at 2000 cm^{-1}. The image plane is inserted 20μm away from the sample and its area is 20×20 μm^2, it is divided to 41×41 pixels. For this analysis because of the limitation of the Mie, the voxels have a geometrical shape of a shell.
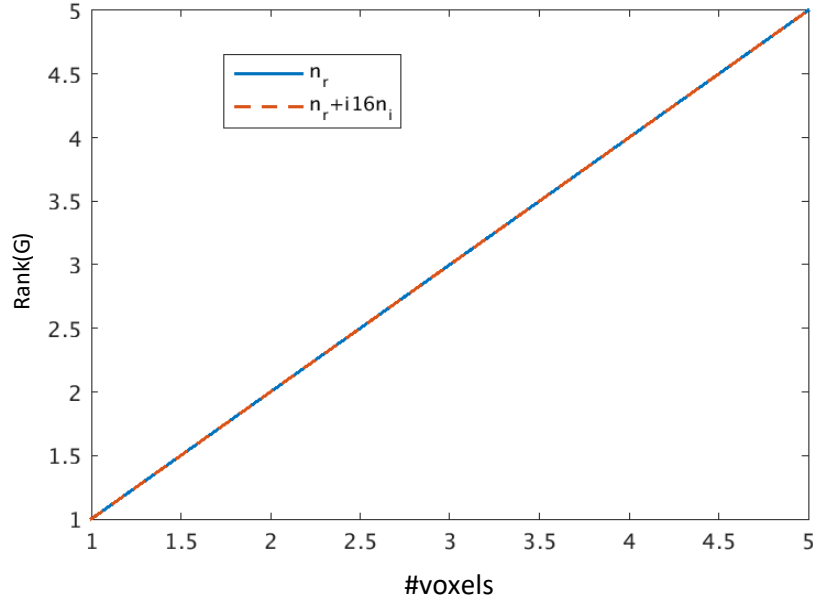
Figure 33 Rank of G as a function of number of the voxels

The rank of a matrix is the maximal number of linearly independent columns of the matrix. If the rows of matrix G are linearly independent, then matrix G is called full ranked. For the linear system of $G\vec{X} = \vec{E}_s$, and the augmented matrix of $(G|\vec{E}_s)$,

- If $rank(G) = rank(G|\vec{E}_s)$ = the number of rows in $\vec{X}$, then the system has a unique solution

- If $rank(G) = rank(G|\vec{E}_s) <$ the number of rows in $\vec{X}$, then the system has many solutions

- If $rank(G) < rank(G|\vec{E}_s)$, then the system is inconsistent.

Rank of the matrix G as a function of the voxels of the sphere is shown in Figure 33. As the number of voxels inside of the sphere increases, the rank of the matrix increases as well.

93
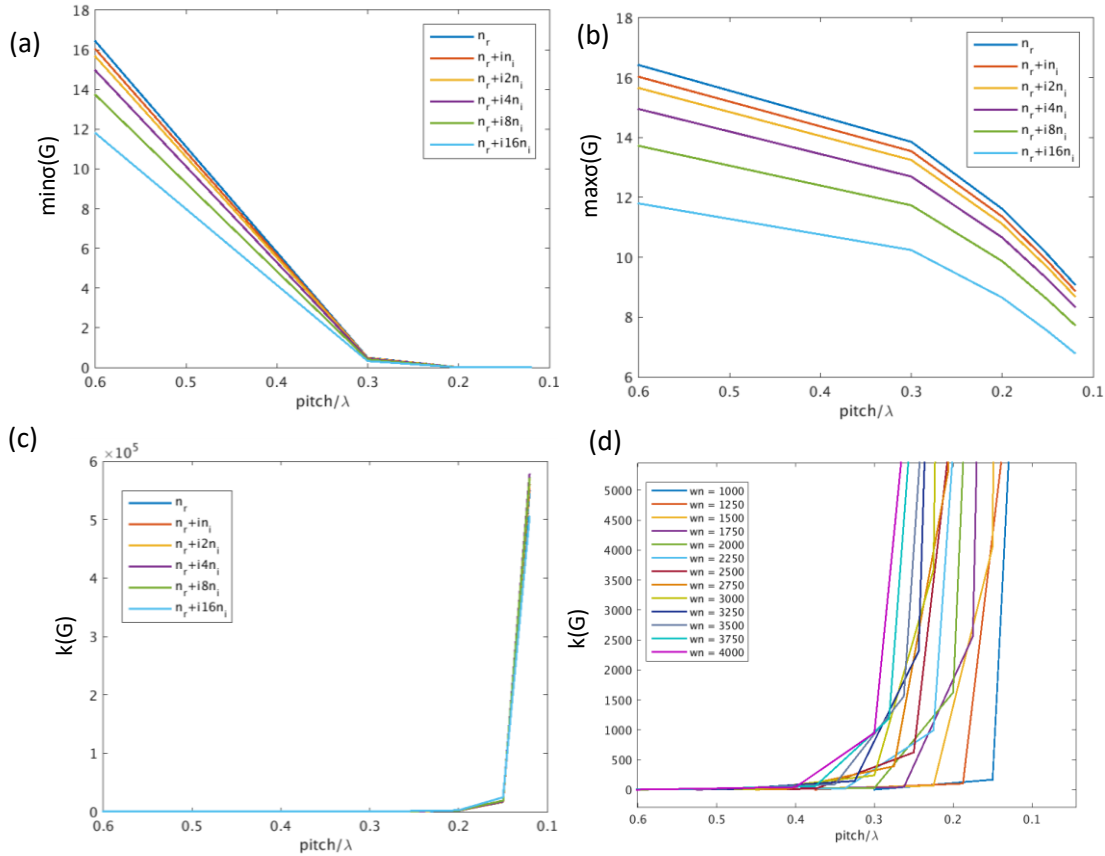
Figure 34 Stability analysis (a) Minimum of the singular values of the matrix G. (b) Maximum of the singular values of matrix G. (c) The condition number of the matrix G, when the imaginary part of the refractive index increases. (d) Condition number as different wavenumbers.

This is expected, because the individual elements of the matrix G are the integration of the electric field that is present in that location multiplied by the Green's function.

For the stability analysis the minimum and maximum singular value, and the condition number of matrix G are calculated. Figure 34 (a) shows the minimum of the singular value of matrix G as a function of $pitch/\lambda$. Pitch here means the thickness of the layer voxel, and λ is the wavelength. The value of the condition number is shown for 6 different value of the refractive index. When the imaginary part of the refractive index increases the condition number decrease, meaning that the algorithm becomes more stable. The imaginary part of the refractive index is doubled in each round of the simulations. The value of n_i is 0.02, 0.01 and 0.005 for core, the central layer and the

94

shell respectively. Figure 34 (b) shows the maximum of the singular value of the matrix G. Figure 34 (c) shows the condition number of the matrix G for different refractive indices. Figure 34 (d) demonstrates the condition number for the case that the refractive indices of the layers are kept at the constant values of 1.5+0.02i, 1.4+0.01i, and 1.3+0.005i, while the wavelength of the incident light is changing.

In order to obtain a better understanding about the effect of the size and shape of the voxels on the condition number of the matrix G, the condition value of the matrix is calculated for different discretization. Then the convergence of the algorithm for each case is tested. The results are summarized in tables 7 to 9. Each cell of the table that is filled with green color is indicative of the specific case, where the algorithm converged with radius of convergence of at least zero. The condition number of the matrix change as the shape or the number of the voxels change, so it is concluded that the convergence of the algorithm is dependent on the shape and the number of the voxels inside of the sphere.

Table 7 Condition number of the matrix G for the voxels that look like water melon slice.

N_r \ N_ϕ	1	2	4
3	1.5717e3	7.0031e3	1.2877e4
6	1.6521e6	1.6906e6	1.0335e7

95

Table 8 Condition number of matrix G for the case where $N_\phi = 1$.

N_r \ N_θ	1	2	4
3	1.5717e3	5.4947e5	7.4716e11
6	1.6521e6	7.4079e12	-

Table 9 Condition number of matrix G for the voxels with shape of volume element in spherical

coordinate

N_r	N_θ	N_ϕ	$\mathcal{K}$
3	2	2	5.5009e5
3	2	4	1.8771e6
6	2	2	7.4116e12

The radii of the convergence for the green cells of tables 7 to 9 are evaluated. The radius of the convergent and the error in each case are summarized in table 4. In these set of calculations, it is expected that the real part of the refractive index n_r is known and the initial guess $n_0 = n_r$. $\max(n_s)$ is the radius of the convergence for the initial guess of $n_0 = n_r$. For example, the first row of the table shows that, for the case where $(N_r, N_\theta, N_\phi) = (3,1,1)$, the condition number has a value of 1571, and the radius of the convergence is $64n_i$, and the algorithm converges after 1 iteration. The errors are shown in the last three columns. n is the complex refractive index of the

96

sample, and n_{per} is the predicted value by the algorithm. For the first two rows, where there is no discretization in θ direction the error in predicting the imaginary part of the refractive index is less than 0.11%, and for the other cases where $N_\theta > 1$, the algorithm does not converge.

Table 2 radius of the convergence for a non-homogenous sphere. Itr is an abbreviation for iterations

N_r	N_θ	N_ϕ	$\mathcal{K}$	$max(n)$	itr	$\dfrac{|n - n_{per}|}{|n|}$	$\dfrac{Re\{n - n_{per}\}}{Re\{n\}}$	$\dfrac{imag\{n - n_{per}\}}{imag\{n\}}$
3	1	1	1571	$n_r + 64n_i$	1	0.0735	0.0116	0.1124
3	1	2	7003	$n_r + 64n_i$	1	0.0771	0.0142	0.1177
3	2	1	54947	$n_r + 8n_i$	1	0.0538	0.0489	0.5006
3	2	2	55009	$n_r + 8n_i$	1	0.0546	0.0489	0.955

5.5.2 Experimental Evaluation of the algorithm

Melanocyte reside in the lower layers of the skin's epidermis. These cells produce melanosomes, which contain light absorbing melanin pigment. Melanoma is a tumor of melanocyte, usually caused by long-term exposure to UV radiation. Changes in the chemical content of the cell affect the refractive index of the cell, so refractive index can be used as a diagnostic indicator and the progress of the cancerous cell can be detected by monitoring the refractive index of the cell. Figure 35 shows the wide field images of the measured melanoma cell. The spherical black objects shown in the figure are called melanosomes. In this chapter we are trying to measure the refractive index of the melanosomes by fitting the simulated holographic images with the measured ones.

97
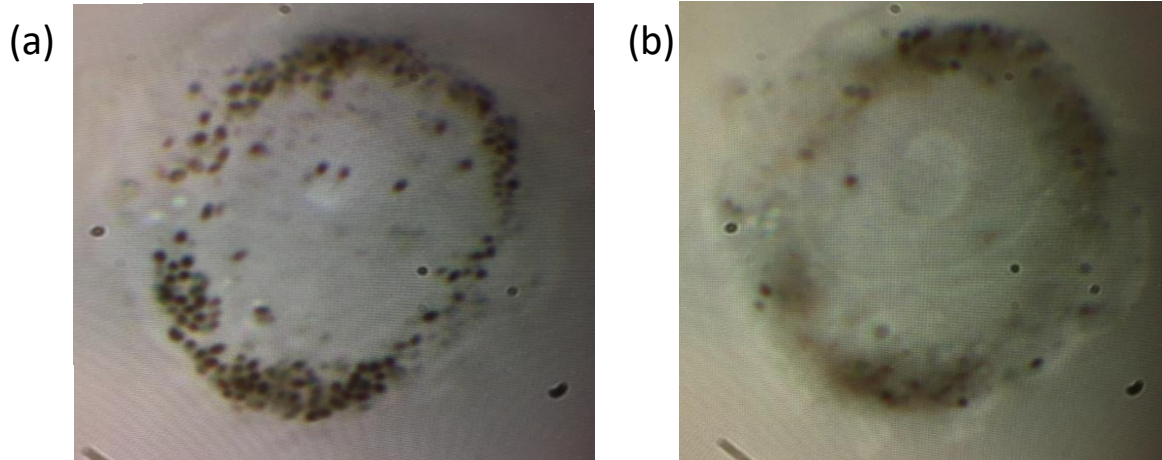
Figure 35 Widefield images of melanoma cell. The black microsphere shape objects are melanosomes(a) Focused at the edge of the cell. (b) Out of focus wide field image

To evaluate the algorithm, broadband phase images of a Melanoma cell is measured in Spectral range of 450-700 nm with a holographic method (Lauer, 2002) (Charrière, et al., 2006) (Choi, et al., 2007). The spectral resolution of the measurement was 5 nm, and the spatial resolution was 0.067 µm.

Digital holography (DH) is one the most effective methods for refractive index measurement. However due to the coherent nature of the required light sources holographic images are hindered by speckle artifact. (Bianco, et al., 2018) As the result Melanosomes are hidden in the speckle pattern as it is shown in Figure 36 (a) and (b). To reduce the noise present in the measure amplitude and phase images, the pixelated spectra are first filtered by Savitzky-Golay digital filter. Then the average size parameter, and the average scattering contribution of the melanosome is calculated by Mie scattering theory. Next, an isolated melanosome inside the cell is selected by means of cross correlation of the Mie scattering with the pixelated spectra. As the next step propagation

www.manaraa.com
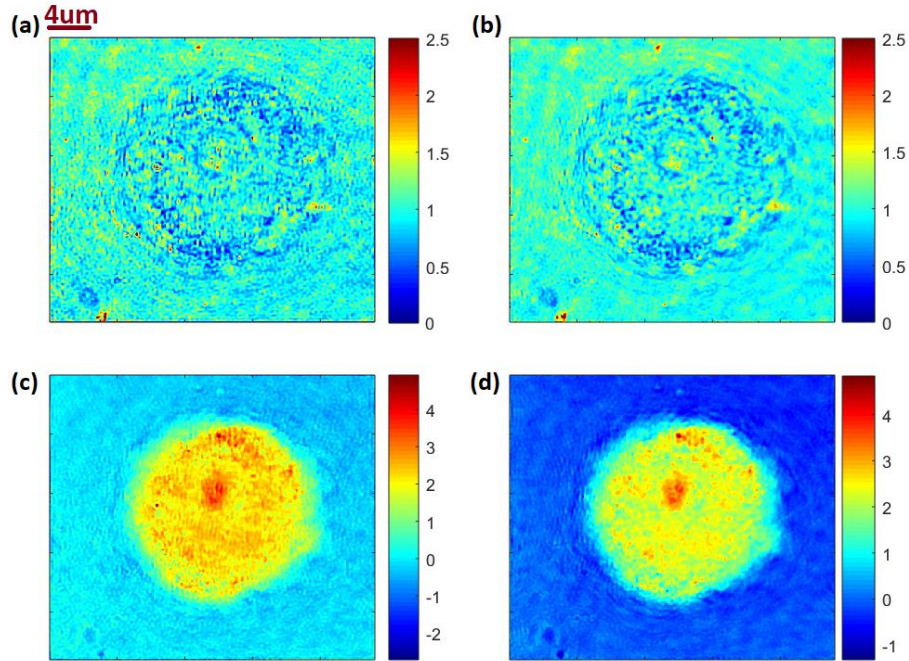
Figure 36 Light Field at the image plane at $\lambda = 575\ nm$ (a) Amplitude without filtering. (b) Amplitude after SG filtering. (c) Phase without filtering (d) Phase after SG filtering

distance of the measured image is approximated. Finally, the complex refractive index of the melanosome is reconstructed as a function of wavelength.

5.5.3 Spectral Filtering

Savitzky-Golay (SG) (Savitzky & Golay, Smoothing and Differentiation of Data by Simplified Least Squares Procedures, 1964) is a digital filter used in spectrometric applications. It approximates the data within a moving window by a polynomial mostly quadratic or cubic. The importance of the SG filtering lies in its ability to preserve higher order moments of the signal. In other words, SG preserves the widths and heights of the spectral peaks, while minimizing the random noise. A SG smoothing filter of polynomial order 3 and frame length of 11 is applied to the pixelated spectra of phase and amplitude separately. Filtering the spectral information, result
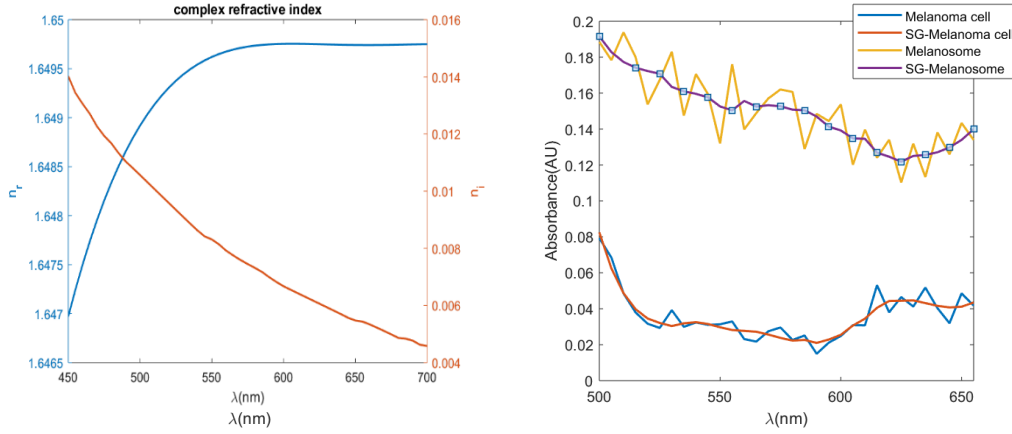
Figure 37 (a)Theoretical complex refractive index of the melanosome in retinal pigmented epithelium. (SONG, ZHANG, NESS, & YI, 2017) *(b) Measured absorbance spectra of the melanoma cell and melanosome before and after filtering.*

in reduction of the speckle pattern in the amplitude and phase images. The result of the SG filtering

on the spatial and spectral information is shown in Figure 36 and Figure 37, respectively.

5.5.4 Melanosome Detection

The average diameter and refractive index of the melanosomes are reported to be 1.2 μm and

1.6 respectively (Seet, Nieminen, & Zvyagin, 2009). Knowing the size parameter of a sphere that

is defined as

$$\rho = 4\pi r(\frac{n_s}{n_m} - 1)v \qquad (5.24)$$

Where r is the radius, n_s is the sample refractive index, n_m is the refractive index of the

medium, $v = \frac{1}{\lambda}$, and λ is the wavelength, the scattering behavior of the particle is explained by

$$Q_{ext} = 2 - \frac{4}{\rho}sin\rho + \frac{4}{\rho^2}(1 - cos\rho). \qquad (5.25)$$

Considering the melanosome as a sphere with diameter of 1.2 μm and refractive index of 1.6,

suspended in a medium with refractive index of 1.37, its Q_{ext} can be predicted by equation

100
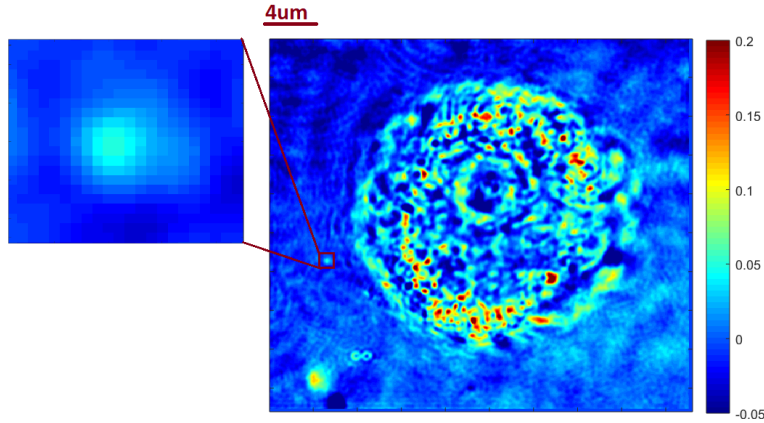
Figure 38 Cross-Correlation of the Q_{ext} of a spherical particle with diameter of 1.2µm and refractive index of 1.2 with the pixelated spectra. The enlarged area shows an isolated melanosome.

(5.25). In order to find an isolated melanosome inside the melanoma cell, the cross-correlation of the predicted Q_{ext} with the pixelated spectra is calculated. The result is shown in Figure 38. An isolated melanosome is chosen and highlighted at the region enlarged in Figure 38. Figure 39 shows the corresponding amplitude and phase images of the isolated melanosome at 500, 575, and 600 nm wavelength. The measured images are dominated by speckle pattern even after SG filtering. The algorithm has applied to the detected melanosome, although the results are promising due to the complexity of the sample, and not having enough information. The correct values of the refractive index is not reconstructed yet. The workflow of these study is going to be added as an appendix at the end of thesis.
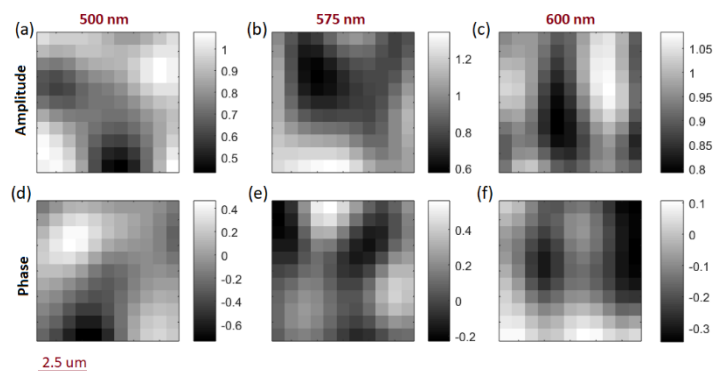
Figure 39 Light Field measured at the position of the isolated melanosome shown in Figure 38. (a) Amplitude at 500nm, (b) Amplitude at 575nm, (c) Amplitude at 600nm, (d) Phase at 500nm, (e) Phase at 575 nm, (f) Phase at 600 nm.

101

5.5.5 Extending the algorithm for Intensity Measurements

In conventional FTIR imaging, intensity and not the electric field is measured at the detector. Here we have shown that, in this case linear Eq. (5.13) changes to a non-linear optimization problem. If the refractive index is a real value starting from we have

$$\vec{E}_{FPA}(\vec{r}) = \vec{E}_{inc}(\vec{r}) + k^2 \int (1 - n(\vec{r}')^2) Grn(\vec{r} - \vec{r}') \vec{E}_{int}(\vec{r}') d^3\vec{r}', \quad (5.26)$$

where $\vec{E}_{FPA}$ is the field observed at the position $\vec{r}$, $\vec{r} = (x, y, z)$ is the coordinate of the image plane, and the sample coordinate is $\vec{r}' = (x', y', z')$. $n(\vec{r}) = n_r(\vec{r}) + jn_i(\vec{r})$ is the complex refractive index at the position $\vec{r}$. $E_{int}(\vec{r}')$ is the internal field of the sample, $k = \frac{2\pi}{\lambda}$ and $Grn(\vec{r} - \vec{r}')$ is the tensor free space Green's function of the Maxwell's equation. Considering simulated intensity as $I_{FPA} \approx |\vec{E}^{FPA}|^2$. We would like to minimize

$$F = \sum_{j=1}^{N_{pixel}} [I^{meas}(\vec{r}_j) - I^{FPA}(\vec{r}_j)]^2 \quad (5.27)$$

Where $j = 1, 2, 3, \dots N_{pixel}$ is the number of pixels. $I^{FPA}(\vec{r}_j)$ and $I^{meas}(\vec{r}_j)$ show simulated intensity at the detector and the measured intensity, respectively. In practice, there is always an experimental error, which differentiates between $I^{meas}(\vec{r}_j)$ and $I^{meas}(\vec{r}_j)$. The best $n(\vec{r})$ is chosen, such that F is minimized. We have

$$\vec{E}_j^{FPA} = \vec{E}_j^{inc} + k^2 \sum_{l=1}^{N_{voxel}} G(\vec{r}_j, \vec{r}_l) X_l \vec{E}_l^{int} \Delta V, \quad (5.28)$$

assuming $X_l = n^2(\vec{r}_l) - 1$,

$$I_j^{FPA} = |\vec{E}_j^{FPA}|^2 = \left[\vec{E}_j^{inc} + k^2 \sum_{l=1}^{N_{voxel}} G_{jl} X_l \vec{E}_l^{int} \Delta V\right]^* \cdot \left[\vec{E}_j^{inc} + k^2 \sum_{m=1}^{N_{voxel}} G_{jm} X_m \vec{E}_m^{int} \Delta V\right]$$

$$= \left|\vec{E}_j^{inc}\right|^2 + k^2 \Delta V \sum_{m=1}^{N_{voxel}} \vec{E}_j^{inc} G_{jm} X_m \vec{E}_m^{int} + k^2 \Delta V \sum_{l=1}^{N_{voxel}} \vec{E}_j^{inc^*} G_{jl}^* X_l^* \vec{E}_l^{int^*} +$$

$$k^4 \Delta V^2 \sum_{l=1}^{N_{voxel}} \sum_{m=1}^{N_{voxel}} G_{jl}^* G_{jm} X_m X_l^* \vec{E}_l^{int^*} \vec{E}_m^{int} \qquad (5.29)$$

defining:

$$P_{jl} = k^2 \Delta V \left\{ \vec{E}_j^{inc^*} G_{jl} \vec{E}_l^{int} + \vec{E}_l^{int} G_{jl}^* \vec{E}_j^{inc} \right\} \qquad (5.30)$$

and

$$Q_{jlm} = \left(\vec{E}_l^{int^*} k^4 \Delta V G_{jl}^* G_{jm} \vec{E}_m^{int} \right) k^4 \Delta V \, (5.31)$$

We have

$$I_j^{FPA} = \left|\vec{E}_j^{inc}\right|^2 + \sum_{l=1}^{N_{voxel}} P_{jl} X_l + \sum_{l=1}^{N_{voxel}} \sum_{m=1}^{N_{voxel}} Q_{jlm} X_l X_m \qquad (5.32)$$

The variables X_l and X_m are unknowns. Therefore,

$$F = F(\vec{X}) = F(X_1, X_2, \ldots, X_{N_{voxel}}) \qquad (5.33)$$

To minimize Eq. (B.8), we need to find

$$\frac{\partial F}{\partial X_l} = 0, \quad (5.34)$$

For all $l = 1, 2, \ldots, N_{voxel}$.

Having

$$\frac{\partial F}{\partial X_l} = \frac{\partial}{\partial X_l} \sum_{j=1}^{N_{pixel}} \left[I_j^{meas} - I_j^{FPA} \right]^2 = 2 \sum_{j=1}^{N_{pixel}} \left[I_j^{meas} - I_j^{FPA} \right] \frac{\partial I_j^{FPA}}{\partial X_l} = 0 \quad (5.35)$$

And,

$$\frac{\partial I_j^{FPA}}{\partial X_l} = P_{jl} + \sum_{\acute{l}=1}^{N_{voxel}} \sum_{\acute{m}=1}^{N_{voxel}} Q_{jl\acute{m}}(\delta_{l\acute{l}} X_{\acute{m}} + \delta_{\acute{m}l} X_{\acute{l}}) = P_{jl} + \sum_{\acute{m}=1}^{N_{voxel}} Q_{jl\acute{m}} X_{\acute{m}} + \sum_{\acute{l}=1}^{N_{voxel}} Q_{j\acute{l}l} X_{\acute{l}}$$

$$= P_{jl} + \sum_{m=1}^{N_{voxel}} [Q_{jlm} + Q_{jml}] X_m \, (5.36)$$

103

All required quantities are now expressed in form of the unknown X_l. Thus, F can be minimized with respect to the N_{voxel} unknowns X_l.

This optimization problem could also be formulated for a complex refractive index as well.

6 Conclusions

Wide field FTIR imaging is a powerful technique for chemical imaging of micro-meter size samples. Wide field FTIR imaging in diffraction limit is restricted to samples that the derivative of their refractive index is a continues function of position. For example, there is no sudden change in the value of the refractive index of the algal cell presented in Chapter 2. This prototype experiment shows the potential of FTIR imaging in revealing information about chemistry of biological samples. However, most of the biological samples are highly scattering.

In order to better understand the scattering phenomena in the pixelated FTIR images, hyperspectral image of a 25 µm polymer bead was measured and simulated. The result shows that apart from the numerical object of the focusing optics, the scattering contributions are highly dependent on the focal depth of the objective and the axial position of the image. Comparing the measured images of thermal and synchrotron sources indicated that pixelated scattering contributions are also dependent on the spatial coherency of the light source. The insight gained from these observations leads us toward implementing an inverse scattering method for recovery of the pure absorbance spectra.

Our iterative inverse scattering method is an optimization algorithm for removing the scattering from the spectra. The algorithm fits the measured field images to a simulated field images in an iterative process and recovers the refractive index of the sample. The method can recover the pure absorptivity of the samples (with imaginary part of the refractive index as high as 3) in presence of Poisson noise. The algorithm is being tested on real experimental data and will be extended for refractive index recovery of inhomogeneous samples.

7 References

Clark, F., & Moffatt, D. (1978). The Elimination of Interference Fringes from Infrared Spectra. *Applied Spectroscopy, 32*(6), 547-549.

Didonna, A., Vaccari, L., Bek, A., & Legname, G. (2011). Infrared Microspectroscopy: A Multiple-Screening Platform for Investigating Single-Cell Biochemical Perturbations upon Prion Infection. *ASC Chemical Neuroscience*, 160-174.

Dijk, T. v., Mayerich, D., Carney, P. S., & Bhargava, R. (2013). Recovery of Absorption Spectra from Fourier Transform Infrared (FT-IR) Microspectroscopic Measurements of Intact Spheres. *APPLIED SPECTROSCOPY*, 546-552.

Hobro, A. J., Pavillon, N., Fujita, K., Ozkan, M., Coban, C., & Smith, N. I. (2015). Label-free Raman imaging of the macrophage response to the malaria pigment hemozoin. *Analyst, 140*(7), 2350-2359.

Loutherback, K., Birarda, G., Chen, L., & Holman, H.-Y. N. (2016). Microfluidic Approaches to Synchrotron Radiation-Based Fourier Transform Infrared (SR-FTIR) Spectral Microscopy of Living Biosystems . *Protein & Peptide Letters*, 273-282.

Mourant, J. R., Freyer, J. P., Hielscher, A. H., Eick, A. A., Shen, D., & Johnson, T. M. (1998). Mechanisms of light scattering from biological cells relevant to noninvasive optical-tissue diagnostics. *APPLIED OPTICS*, 3586-3593.

Nasse, M. J., Walsh, M. J., Mattson, E. C., Reininger, R., Kajdacsy-Balla, A., Macias, V., . . . Hirschmugl, C. J. (2011). High-resolution Fouriertransform infrared chemical imaging with multiple synchrotron beams. *Nature Methods*, 413-418.

Rahmelow, K., & Hubner, W. (1997). Infrared Spectroscopy in Aqueous Solution: Difficulties and Accuracy of Water Subtraction. *Applied Spectroscopy, 51*(2), 160-170.

YAGHJIAN, A. D. (1980). Electric Dyadic Green's Functions in the Source Region . *PROCEEDINGS OF THE IEEE, 68*(2), 248-263.

Abo-Bakr, M., Feikes, J., Holldack, K., Kusk, P., Peatman, W. B., Schade, U., & Wu¨stefeld, G. (2003). Brilliant, Coherent Far-Infrared (THz) Synchrotron Radiation. *PHYSICAL REVIEW LETTERS, 90*, 094801-1 to 4.

Almog, I., Bradley, M., & Bulovi´c, V. (n.d.). *The Lorentz Oscillator and its Applications.* Retrieved February 21, 2019, from MITOPENCOURSEWARE: https://ocw.mit.edu/courses/electrical-engineering-and-computer-science/6-007-electromagnetic-energy-from-motors-to-lasers-spring-2011/readings/MIT6_007S11_lorentz.pdf

Baker, M. J., Trevisan, J., Bassan, P., Bhargava, R., Butler, H. J., Dorling, K. M., . . . Martin, F. L. (2014). Using Fourier Transform IR spectroscopy to analyze biological materials. *Nature Protocol, 9*(8), 1771-1791.

Baker, M. J., Trevisan, J., Bassan, P., Bhargava, R., Butler, H. J., Dorling, K. M., . . . Martin, F. L. (2014). Using Fourier transform IR spectroscopy to analyze biological materials. *Nature Protocols*, 1771-1791.

Bansal, R. (1999). The Far-Field: How Far is Far Enough? *Design Ideas - Applied Microwave and Wireless*, 58-60.

Barber, D., Cole, A., & Thompson, H. (1949). Infrared Spectroscopy With The Reflecting Microscope In Physics, Chemistry and Biology. *Nature*, 198-201.

Bassan, P. (2011). *Light scattering during infrared spectroscopic measurements of biomedical samples.* Ph. D. Thesis: University of Manchester.

Bassan, P., Kohler, A., Martens, H., Lee, J., Byrne, H. J., Dumas, P., . . . Gardner, P. (2009). Resonant Mie Scattering (RMieS) correction of infrared spectra from highly scattering biological samples. *Analyst*, 268-277.

Berisha, S., Dijk, T. v., Bhargava, R., Carney, P. S., & Mayerich, D. (2017). BIM-Sim: Interactive Simulation of Broadband Imaging Using Mie Theory. *frontiers in Physics*.

Bhargava, R. (2012). Infrared Spectroscopic Imaging: The Next Generation. *Appl Spectrosc, 66*(10), 1091-1120.

Bianco, V., Memmolo, P., Leo, M., Montresor, S., Distante, C., Paturzo, M., . . . Ferraro, P. (2018). Strategies for reducing speckle noise in digital holography. *Light: Science & Applications, 18*.

Bl¨umel, R., Ba˘gcıo˘glu, M., Lukacs, R., & Kohler, A. (2016, May 23). *Infrared refractive index dispersion of PMMA spheres from synchrotron extinction spectra.* Retrieved from Archive: https://arxiv.org/abs/1605.07011

Blout, E. R., & Bird, G. R. (1950). Infrared Microspectroscopy. *The Optical Society of America*, 304-313.

Blumel, R., Bagcioglu, M., Lukaccs, R., & Kohler, A. (2016). *Infrared refractive index dispersion of polymethyl methacrylate spheres from Mie ripples in Fourier-transform infrared microscopy extinction spectra.* 2016: Journal of the Optical Society of America.

Bohren, C. F., & Huffman, D. R. (1998). Absorption and Scattering by a sphere. In *Absorption and Scattering of Light by Small Particles* (pp. 82-129). WILEY-VCH Verlag GmbH & Co. KGaA.

Brereton, R. G. (2009). *Chemometrics for Pattern Recognition.* John Wiley & Sons, Ltd.

Burch, C. R. (1947). Reflecting microscopes. *Proceedings of the Physical Society*, 41-47.

Charrière, F., Marian, A., Montfort, F., Kuehn, J., Colomb, T., Cuche, E., . . . Depeursinge, C. (2006). Cell refractive index tomography by digital holographic microscopy. *Optics Letters, 31*(2), 178-180.

Chittur, K. K. (1998). FTIR/ATR for protein adsorption to biomaterial surfaces. *Biomaterials, 19*(4-5), 357-369.

Choi, W., Fang-Yen, C., Badizadegan, K., Oh, S., Lue, N., Dasari, R. R., & Feld, M. S. (2007). Tomographic phase. *Nature Methods*, 717-719.

107

Cittert, P. V. (1934). Die Wahrscheinliche Schwingungsverteilung in Einer von Einer Lichtquelle Direkt Oder Mittels Einer Linse Beleuchteten Ebene. *Physica, 1*(1-6), 201-210.

Coates, V. J., Offner, A., & Siegler, E. (1953). Design and Performance of an Infrared Microscope Attachment. *Optical Society of America*, 984-989.

Coisson, R. (1995). Spatial coherence of synchrotron radiation. *APPLIED OPTICS*, 904-908.

Criag F. Bohren, Donald R. Huffman. (2004). *Absorption and Scattering of Light by Small Particles.* Germany: John Wilet & Sons, Inc.

Deng, Y., & Chu, D. (2017). Coherence properties of different light sources and their effect on the image sharpness and speckle of holographic displays. *scientific reports*.

Dorrer, C. (2004). Temporal van Cittert–Zernike theorem and its application to the measurement of chromatic dispersion. *The Optical Society of America, 21*(8), 1417-1423.

Dunn, A., & Richards-Kortum, R. (1996). Three-dimensional computation of light scattering from cells. *IEEE Journal of Selected Topics in Quantum Electronics*, 898-905.

Economou, E. N. (1979). *Green's Functions in Quantum Physics.* Germany: Springer.

Farrington, P. J., Hill, D., O'Donnell, H., & Pomery, P. J. (1990). Suppression of Interference Fringes in the Infrared Spectra of Thin Polymer Films. *The Optical Society, 44*(5), 901-903.

Fernandez, D. C., Bhargava, R., Hewitt, S. M., & Levin, I. W. (2005). Infrared spectroscopic imaging for histopathologic recognition. *nature biotechnology*, 496-474.

Fischer, D. G., Dijk, T. v., Visser, T. D., & Wolf, E. (n.d.).

Fourier Transform Spectroscopic Imaging Using an Infrared Focal-Plane Array Detector. (1995). *Analytical Chemistry*, 3377-3381.

FREITAS, R. O., DENEKE,, C., MAIA, F. C., MEDEIROS, H. G., MORENO, T., DUMAS, P., . . . WESTFAHL, D. (2018). Low-aberration beamline optics for synchrotron infrared nanospectroscopy. *OPTICS EXPRESS*, 11238-11249.

Fu, Q., & Sun, W. (2001). Mie theory for light scattering by a spherical particle in an absorbing medium. *Applied Optics*, 1354-1361.

Geladi, P., MacDougall, D., & Martens, H. (1985). Linearization and Scatter-Correction for Near-Infrared Reflectance Spectra of Meat. *Applied Spectroscopy, 39*(3), 491-500.

Goedecke, G. H., & O'Brien, S. G. (1988). Scattering by irregular inhomogeneous particles via the digitized Green's function algorithm. *Applied Optics*, 2431-2438.

GONZAGA-GALEANA, J. A., & ZURITA-SÁNCHEZ, J. R. (2018). Mie scattering of partially coherent light: controlling absorption with spatial coherence. *Optics Express*, 2928-2943.

Goodman, J. W. (1985). *Statistical Optics.* New York: John Wiley & Sons.

Goodman, J. W. (2005). *Fourier Optics.* Greenwood Village, CO: Ben Roberts.

Greffet, J.-J., Cruz-Gutierrez, M. D., Ignatovich, P. V., & Radunsky, A. (2003). Influence of spatial coherence on scattering by a particle. *Optical Society of America*, 2315-2320.

Griffiths, P. R., & de Haseth, J. A. (2007). *Fourier Transform Infrared Spectrometry.* Athens, Georgia: WILEY.

Harrick, N. J. (1977). Transmission Spectra without Interference Fringes. *Applied Spectroscopy, 31*(6), 548-549.

Heraud, P., Ng, E. S., Caine, S., Qing, Y. C., Hirst, C., Mayberry, R., . . . Elefanty, A. G. (2010). Fourier transform infrared microspectroscopy identifies early lineage commitment in differentiating human embryonic stem cells. *Stem Cell Research*, 140-147.

Hermes, M., Morrish, R. B., Huot, L., Meng, L., Junaid, S., Tomko, J., . . . Stone, N. (2018). Mid-IR hyperspectral imaging for label-free histopathology and cytology. *Journal of Optics, 20*, 1-21.

Hetch, E. (1974). *Optics.* Addison Wesley.

Hirschfeld, T. (1978). New trends in the application of Fourier transform infrared spectroscopy to analytical chemistry. *The Optical Society, 17*(9), 1400-1412.

Hirschfeld, T., & Mantz, A. (1976). Elimination of Thin Film Infrared Channel Spectra in Fourier Transform Infrared Spectroscopy. *Applied Spectroscopy, 30*(5), 552-553.

Hirschmugl , C. J., & Gough, K. M. (2012). Fourier Transform Infrared Spectrochemical Imaging: Review of Design and Applications with a Focal Plane Array and Multiple Beam Synchrotron Radiation Source. *Applied Spectroscopy*, 475-491.

Holman, H.-Y. N., Bechtel, H. A., Hao, Z., & Martin, M. C. (2010). Synchrotron IR Spectromicroscopy: Chemistry of Living Cells. *analytical chemistry*, 8757-5765.

Holman, H.-Y. N., Bechtel, H. A., Hao, Z., & Martin, M. C. (2010). Synchrotron IR Spectromicroscopy: Chemistry of Living Cells. *analytical chemistry*, 8757-8765.

Huang, Z. (2013). BRIGHTNESS AND COHERENCE OF SYNCHROTRON RADIATION AND FELs. *The 4th International Particle Accelerator Conference.* Shanghai, China.

Hulst, H. (1981). *Light Scattering by Small Particles.* New York: John Wiley & Sons.

Hyperspectral remote sensing. (2019, 6 26). Retrieved from university of texas: http://www.csr.utexas.edu/projects/rs/hrs/hyper.html

Ibrahim, A., Predoi-Cross, A., & Povey, C. (2013). Handling techniques for channel spectra in synchrotron-based Fourier transform spectra. *Canadian Journal of Physics, 91*(11), 920-923.

Kak, A. C., & Slaney, M. (1988). *Principles of Computerized Tomographic Imaging.* Newyork: IEEE Press.

KnowItAll. (2017). USA: Bio-Rad.

KOHLER, A., SULE´-SUSO, J., SOCKALINGUM, G., TOBIN, M., BAHRAMI, F., YANG, Y., . . . MARTENS, H. (2008). Estimating and Correcting Mie Scattering in Synchrotron-Based Microscopic Fourier Transform Infrared Spectra by Extended Multiplicative Signal Correction. *APPLIED SPECTROSCOPY*, 259-266.

Konevskikh , T., Lukacs, R., & Kohler, A. (2017). An improved algorithm for fast resonant Mie scatter correction of infrared spectra of cells and tissues. *Journal of Biophotonics*.

109

Konevskikh, T., Lukacs, R., Bl¨umel, R., Ponossov, A., & Kohler, A. (2015). Mie scatter corrections in single cell infrared microspectroscopy. *Faraday Discussions*, 235-257.

Konevskikh, T., Ponossov, A., Blümel, R., Lukacs, R., & Kohler, A. (2015). Fringes in FTIR spectroscopy revisited: understanding and modelling fringes in infrared spectroscopy of thin films. *Analyst, 140*, 3969-3980.

Krauze, W., Kus´, A., S´ladowski, D., Skrzypek, E., & Kujawin´ska, M. (2018). Reconstruction method for extended depth-of-field optical diffraction tomography. *Methods, Science Direct*, 40-49.

Kuimova, M., Chan , K., & Kazarian, S. (2009). Chemical imaging of live cancer cells in the natural aqueous environment. *Applied Spectroscopy, 63*(2), 164-171.

Lauer, A. (2002). New approach to optical diffraction tomography yielding a vector equation of diffraction tomography and a novel tomographic microscope. *Journal of Microscopy, 205*(2), 165-176.

Lavrinenko, A. V., Laegsgaard, J., Gregersen, N., Schmidt, F., & Sondergaard, T. (2017). *Numerical Methods in Photonics.* Boca Raton, FL: Taylor & Francis Group.

Lavrinenko, A. V., Leagsgaard, J., Gregersen, N., Schmidt, F., & Sondergaard, T. (2014). *Numerical Methods in Photonics.* CRC PRESS .

Lewis, E. N., Treado, P. J., Reeder, R. C., Story, G. M., Dowrey, A. E., Marcott, C., & Levin, I. W. (1995). Fourier Transform Spectroscopic Imaging Using an Infrared Focal-Plane Array Detector. *Analytical Chemistry*, 3377-3381.

Liu, C., Capjack, C. E., & Rozmus, W. (2005). 3-D simulation of light scattering from biological cells and cell differentiation. *Journal of Biomedical Optics*, 014007-1-12.

Martin, M. C., Dabat-Blondeau, C., Unger, M., Sedlmair, J., Parkinson, D. Y., Bechtel, H. A., . . . Hirschmugl, C. J. (2013). 3D spectral imaging with synchrotron Fourier transform infrared spectro-microtomography. *Nature Methods*, 861-865.

Matrigel. (n.d.). (WIKIPEDIA) Retrieved 6 7, 2019, from https://en.wikipedia.org/wiki/Matrigel

Mattson, E. C., Nasse, M. J., Rak, M., Gough, K. M., & Hirschmugl, C. J. (2012). Restoration and Spectral Reconvery of Mid-Infrared Chemical Images. *analytical chemistry*, 6173-6180.

Mattson, E. C., Unger, M., Clede, S., Lambert, F., Policar, C., Imtiaz, A., . . . Hirschmugl, C. J. (2013). Toward optimal spatial and spectral quality in widefield infrared spectromicroscopy of IR labelled single cells. *Analyst*, 5610-5618.

Meglinski, I. (2015). *Biophotonics for Medical Applications.* Elsevier Ltd.

Melin, A.-M., Perromat, A., & Déléris, G. (2001). Sensitivity of Deinococcus radiodurans to γ-Irradiation: A Novel Approach by Fourier Transform Infrared Spectroscopy. *ELSEVIER, Archives of Biochemistry and Biophysics, 394*(15), 256-274.

Miller, L., Q, W., TP, T., RJ, S., Lanzirotti, A., & Miklossy, J. (2006). Synchrotron-based infrared and X-ray imaging shows focalized accumulation of Cu and Zn co-localized with beta-amyloid deposits in Alzheimer's disease. *ELSEVIER*, 30-37.

110

Miyamoto, K., Yamada, P., Yamaguchi, R., Muto, T., Hirano, A., Kimura, Y., . . . Isoda, H. (2007). In situ observation of a cell adhesion and metabolism using surface infrared spectroscopy. *Cytotechnology, 55*(2-3), 143-149.

Muller, P., Schurmann, M., & Guck, J. (2016, October 10). The Theory of Diffraction Tomography. Dresden, Germany.

Nasse, M. J., Ratti, S., Giordano, M., & Hirschmugl, C. J. (2009). Demountable Liquid/Flow Cell for in vivo Infrared Microspectroscopy of Biological Specimens. *Applied Spectroscopy*.

PARK, C., SHIN, S., & PARK, Y. (2018). Generalized quantification of three-dimensional resolution in optical diffraction tomography using the projection of maximal spatial bandwidths. *Journal of the Optical Society of America*, 1891-1898.

Quaroni, L., Zlateva, T., Sarafimov, B., Kreuzer, H., Wehbe, K., Hegg, E., & Cinque, G. (2014). Synchrotron based infrared imaging and spectroscopy via focal plane array on live fibroblasts in D2O enriched medium. *Biophysical Chemistry, 189*, 40-48.

Savitzky, A., & Golay, M. (1964). Smoothing and Differentiation of Data by Simplified Least Squares Procedures. *Analytical Chemistry, 36*(8), 1627-1639.

Savitzky, A., & Golay, M. J. (1964). Smoothing and Differentiation of Data by Simplified Least Squares Procedures. *Analytical Chemistry*, 1627-1639.

Schmidt, J. D. (2010). *Numerical Simulation of Optical Wave Propagation with Examples in MATLAB.* SPIE .

Seet, K. Y., Nieminen, T. A., & Zvyagin, A. V. (2009). Refractometry of melanocyte cell nuclei using optical scatter images recorded by digital Fourier microscopy. *Journal of Biomedical Optics*, 044031(1-7).

Solheim, J. H., Evgeniy Gunko, E., Peterson, D., Großerüschkamp, F., Gerwert, K., & Kohler, A. (2019). An open-source code for Mie extinction extended multiplicative signal correction for infrared microscopy spectra of cells and tissues. *Journal of Biophotonics*.

Solheim, J., Gunko, E., Petersen, D., Frederik, e. G., Gerwert, K., & Kohler, A. (2019). An open source code for Mie Extinction EMSC for infrared microscopy spectra of cells and tissues. *Wiley Online Library*.

SONG, W., ZHANG, L., NESS, S., & YI, J. (2017). Wavelength-dependent optical properties of melanosomes in retinal pigmented epithelium and their changes with melanin bleaching: a numerical study. *Biomedical Optics Express*, 3966-3979.

Su, X., Capjack, C., Rozmus, W., & Backhouse, C. (2007). 2D light scattering patterns of mitochondria in single cells. *Opt Express*, 10562-10575.

Tao Su, X., Capjack, C., Rozmus, W., & Backhouse, C. (2007). 2D light scattering patterns of mitochondria in single cells . *OPTICS EXPRESS*, 10562-10575.

Tisinger, L. (2018, 11 4). *agilent.* Retrieved from library: https://www.agilent.com/cs/library/eseminars/public/Chemical_Imaging_for_Industrial_Laboratories.pdf

Tobin, M. J., Puskar, L., Barber, R. L., Harvey, E. C., Heraud, P., Wood, B. R., . . . Munro, K. L. (2010). FTIR spectroscopy of single live cells in aqueous media by synchrotron IR microscopy using microfabricated sample holders. *Vibrational Spectroscopy*, 34-38.

Vaccari, L., Birarda, G., Businaro, L., Pacor, S., & Grenci, G. (2012). Infrared Microspectroscopy of Live Cells in Microfluidic Devices (MD-IRMS): Toward a Powerful Label-Free Cell-Based Assay. *analytical chemistry*, 4768-4775.

Walter, N., & Patch, S. (2018). Mie Electric Field Simulation for Spheres. Milwaukee: Mathworks.

Wieliczka, D. M., Weng, S., & Querry, M. R. (1989). Wedge shaped cell for highly absorbent liquids: infrared optical constants of water. *The Optical Society, 28*(9), 1714-1719.

Wold, S., Martens, H., & Wold, H. (1983). The multivariate calibration problem in chemistry solved by the PLS method. *Matrix Pencils*, 286-293.

Yeh, K., Kenkel, S., Liu, J.-N., & Bhargava, R. (2015). Fast Infrared Chemical Imaging with a Quantum Cascade Laser. *analytical chemistry*, 485-493.

Zernike, F. (1938). The concept of degree of coherence and its application to optical problems. *Physica, 5*(8), 785-795.

Curriculum Vitae

Ghazal Azarfar

Physicist and engineer pursuing her PhD at University of Wisconsin Milwaukee with 3 years of experience with infrared hyper spectral imaging, big data analysis, and numerical modeling of optical systems.

Education and Training

Ph.D.: Electrical Engineering, 2014 to present

Field of study: Optics, Minor: Mathematics

University of Wisconsin Milwaukee – Milwaukee, WI, United States

GPA: 3.92/4

Master of Science: Electrical Engineering, 2012-2014

Field of study: Digital Electronics

Shahid Beheshti University – Tehran, Iran

GPA: 4/4

Bachelor of Science: Electrical Engineering, 2008-2012

Field of study: Electronics

Shahid Beheshti University – Tehran, Iran

GPA: 4/4

Skills

- MATLAB
- ANSYS Mechanical APDL
- Labview

- FPGA design/ ISE Design Suite
- C++ programming
- CST

Research Interests

Inverse Scattering

Cryptography

Holography

www.manaraa.com

Multivariant Data Analysis

3D chemical imaging

Biomedical Imaging

Optical Design

far and mid-infrared absorption studies

Numerical simulation of optical wave propagation

Research Experience

Research Assistant, under supervision of Prof. Carol Hirschmugl:

May 2016 to May 2018, University of Wisconsin Milwaukee

1)   "Correction of Multiple Light scattering features in Diffraction Limited broad-band infrared Images", Since Aug 2018

2)   "Comparison of light sources: Laser, Synchrotron and Thermal broadband sources with application in infrared Chemical Imaging", Since Dec 2018

3)   "Role of Light Scattering in Spatially Resolved Synchrotron Chemical Imaging", Since Feb 2017

4)   "Three-dimensional IR Spectro-Microtomography of Diamonds", Jan 2017

5)   "Simulation and Analyzing Forward Projection of a Microsphere under Irradiation of IR Source", Since Nov 2016.

6)   "Developing a Method for Fringe Correction in Chemical Images", Dec 2017.

7)   "Correction of Optical Transfer Function of a Specific IR Microscope", Jun 2016.

External Intern in Neurophysiology department. under supervision of Prof. Tansu Celikel

Jan 2014 to May 2014, Radboud University Nijmegan – Netherland

Analyzing result of simulation of Neural Networks in Barrel Cortex of rat.

Publication

1.   Ghazal Azarfar, Ebrahim Aboualizadeh, Nickolas M. Walter, Simona Ratti, Camilla Olivieri, Alessandra Norici, Achim Kohler, Mario Giordano, Carol Hirschmugl,

"*Estimating and Correcting Interference Fringes in Infrared Spectra in Infrared Hyperspectral Imaging*", (**Analyst, published Sep 2018**).

2.   Ghazal Azarfar, Ebrahim Aboualizadeh, Nickolas M. Walter, Simona Ratti, Camilal Oliviera, Alessandra Norici, Michael Nasse, Mario Giordano, Carol Hirschmugl, "*Time-Resolved Mid-IR Synchrotron Hyperspectral Imaging of Thalassiosira weissflogi as a function of CO_2 Availibility*", (Submitted to **Scientific Reports, Aug 2019**).

3. Ghazal Azarfar, Nickolas M. Walter, Achim Kohler, Reinhold Blumel, Carol Hirschmugl, "*Recovery of frequency-dependent refractive index via optimizing inverse scattering Green's function method*", (Submitted to **Journal of the Optical Society of America A, Aug 2019**).

4. Ghazal Azarfar, Hamid Hassani, Achim Kohler, Reinhold Blumel, Yongjin Sung, Carol Hirschmugl, "*3D Near Infrared Hyperspectral Imaging of Melanosomes by Solving a System of Linear Equations*", (In Preparation for Submission to **Frontier in Physics**).

Conference Presentation

Poster Presentation at CEAS Poster Competition:
 Apr 2019, University of Wisconsin Milwaukee, Milwaukee, WI:
Ghazal Azarfar, Hamid Hassani, Yongjin Sung, Achim Kohler, Reinhold Blumel, Carol Hirschmugl, "*A New Algorithm: 3D Chemical Infrared Imaging*".

Oral Presentation at SCIX Conference:
 Oct 2018, Marriott Marquis, Atlanta, GA
Ghazal Azarfar, Nickolas Walter, Alex J Schofield, Sugato Ray, Zahra Alavi, Achim Kohler, Reinhold Blumel, Sarah Patch, Carol Hirschmugl, "*Measurement of 2D Coherence Factor of Infrared light sources and Its Application in Diffraction Limited Fourier Transform Chemical Imaging*".

115

Poster Presentation at CEAS Poster Competition:

 Apr 2018, University of Wisconsin Milwaukee, Milwaukee, WI:

<u>Ghazal Azarfar</u>, Nickolas Walter, Alex J Schofield, Sugato Ray, Zahra Alavi, Achim Kohler, Reinhold Blumel, Sarah Patch, Carol Hirschmugl, "*Role of Light Scattering in Spatially Resolved Synchrotron Chemical Imaging*".

Poster Presentation at SCIX Conference,

Oct 2017, Grand Sierra Resort, Reno, NV:

<u>Ghazal Azarfar</u>, Ebrahim Aboualizadeh, Nickolas Walter, Achim Kohler, Carol Hirschmugl, "*Eliminating Fringes from Synchrotron FTIR Images Reveals Modification of Thalassiosira weissflogi Metabolism During Short-term CO_2 Acclimation*".

Poster Presentation at AVS Prairie Chapter Symposium:

Sep 2017, Discovery World Science and Technology Museum**,** Milwaukee, WI:

<u>Ghazal Azarfar</u>, Nickolas Walter, Alex J Schofield, Sugato Ray, Zahra Alavi, Achim Kohler, Reinhold Blumel, Sarah Patch, Carol Hirschmugl, "*Role of Light Scattering in Spatially Resolved Synchrotron Chemical Imaging*".

Poster Presentation at CEAS Poster Competition:

 Apr 2017, University of Wisconsin Milwaukee, Milwaukee, WI:

<u>Ghazal Azarfar</u>, Ebrahim Aboualizadeh, Nickolas Walter, Achim Kohler, Carol Hirschmugl, "*Eliminating Fringes from Hyperspectral Data to Localize Chemically Distinct Macromolecules*".

Teaching Experience

Lecturer – Technology Around the World

Aug 2018 to Dec 2018, University of Wisconsin Milwaukee

Teaching Assistant - Introduction to Electrical Engineering

 Aug 2015 to May 2016, University of Wisconsin Milwaukee

Teaching Assistant - Microprocessors

September 2013 to December 2013, Shahid Beheshti University, Tehran, Iran

Teaching Assistant - Engineering Mathematics

 Jan 2011 to Dec 2011, Shahid Beheshti University, Tehran, Iran

Honor and Awards

Honorable Mention Award in CEAS Poster Competition, University of Wisconsin Milwaukee, Spring 2019

The Chancellor's Graduate Student Award, University of Wisconsin Milwaukee, Spring 2019.

The Chancellor's Graduate Student Award, University of Wisconsin Milwaukee, Fall 2018.

4 Years Dean's fellowship award, University of Wisconsin Milwaukee, 2014.

Distinguished undergraduate student scholarship; each year this award is given to less than 1% of undergraduate students among all electrical engineering undergraduates in Iran to enter master program, 2012.

Professional Experience

Intern in Mana R&D center

Jan 2012 to Dec 2013, *Mana Pardaz Control system design Co*. - Tehran, Iran.

Work as a team member to design a 3D Monitoring System: implementing Ethernet in a FPGA.

Graduate Student Ambassador

May 2016 to April 2018, *UWM Research Foundation*, under supervision of Dr. Jessica Silvaggi – Milwaukee, United States.

Volunteer Experience

Reestablishment of SAS at UWM

Since Oct 2017, *Society of Applied Spectroscopy*, under supervision of Dr. Rober Lascola and Dr. Carol Hirchmugl – Milwaukee, United States.

Women in Physics

Member since Jun 2018

Affiliations

University of Wisconsin Milwaukee (United States)

Society for Applied Spectroscopy (United States)

University of Wisconsin Milwaukee Research Foundation (United States)